

1 LEVERAGING MULTI-MESSENGER ASTROPHYSICS FOR DARK MATTER SEARCHES

By

Daniel Nicholas Salazar-Gallegos

A DISSERTATION

Submitted to
Michigan State University
in partial fulfillment of the requirements
for the degree of

Physics—Doctor of Philosophy
Computational Mathematics in Science and Engineering—Dual Major

Today

ABSTRACT

3 I did Dark Matter with HAWC and IceCube. I also used Graph Neural Networks

⁴ Copyright by

⁵ DANIEL NICHOLAS SALAZAR-GALLEGOS

⁶ Today

ACKNOWLEDGMENTS

8 I love my friends. Thanks to everyone that helped me figure this out. Amazing thanks to the people
9 at LANL who supported me. Eames, etc Dinner Parties Jenny and her child Kaydince Kirsten, Pat,
10 Andrea Family. You're so far but so critical to my formation. Unconditional love. Roommate

TABLE OF CONTENTS

12	LIST OF TABLES	vii
13	LIST OF FIGURES	viii
14	LIST OF ABBREVIATIONS	xv
15	CHAPTER 1 INTRODUCTION	1
16	CHAPTER 2 DARK MATTER IN THE COSMOS	2
17	2.1 Introduction	2
18	2.2 Dark Matter Basics	3
19	2.3 Evidence for Dark Matter	4
20	2.4 Searching for Dark Matter: Particle DM	11
21	2.5 Sources for Indirect Dark Matter Searches	16
22	2.6 Multi-Messenger Dark Matter	18
23	CHAPTER 3 MULTIMESSENGER ASTROPHYSICS: DETECTING HIGH EN-	
24	ERGY NEUTRAL MESSENGERS	21
25	3.1 Introduction	21
26	3.2 Charged Particles in a Medium	21
27	3.3 Photons (γ)	22
28	3.4 Neutrinos (ν)	22
29	3.5 Opportunities to Combine for Dark Matter	22
30	CHAPTER 4 HIGH ALTITUDE WATER CHERENKOV (HAWC) OBSERVATORY .	24
31	4.1 The Detector	24
32	4.2 Events Reconstruction and Data Acquisition	24
33	4.3 Remote Monitoring	24
34	CHAPTER 5 ICECUBE NEUTRINO OBSERVATORY	25
35	5.1 The Detector	25
36	5.2 Events Reconstruction and Data Acquisition	25
37	5.3 Northern Test Site	25
38	CHAPTER 6 GLORY DUCK: MULTI-WAVELENGTH SEARCH FOR DARK MATT-	
39	TER ANNIHILATION TOWARDS DWARF SPHEROIDAL GALAX-	
40	IES	26
41	6.1 Introduction	26
42	6.2 Dataset and Background	28
43	6.3 Analysis	29
44	6.4 Likelihood Methods	34
45	6.5 HAWC Results	40
46	6.6 Glory Duck Combined Results	43
47	6.7 HAWC Systematics	48

48	6.8 <i>J</i> -factor distributions	49
49	6.9 Discussion and Conclusions	55
50	CHAPTER 7 MULTITHREADING HAWC ANALYSES FOR DARK MATTER	
51	SEARCHES	59
52	7.1 Introduction	59
53	7.2 Dataset and Background	59
54	7.3 Analysis	60
55	7.4 Likelihood Methods	65
56	7.5 Computational Methods: Multithreading	65
57	7.6 Analysis Results	71
58	7.7 Systematics	71
59	7.8 Conclusion and Discussion	72
60	CHAPTER 8 HEAVY DARK MATTER ANNIHILATION SEARCH WITH ICE-	
61	CUBE'S NORTH SKY TRACK DATA	79
62	CHAPTER 9 NU DUCK	80
63	APPENDIX A MULTI-EXPERIMENT SUPPLEMENTARY FIGURES	81
64	APPENDIX B MULTITHREADING SUPPLEMENTARY FIGURES	82
65	B.1 <code>mpu_analysis.py</code>	83
66	BIBLIOGRAPHY	92

LIST OF TABLES

68	Table 6.1	Summary of the relevant properties of the dSphs used in the present work. Column 1 lists the dSphs. Columns 2 and 3 present their heliocentric distance and galactic coordinates, respectively. Columns 4 and 5 report the J -factors of each source given from the \mathcal{GS} and \mathcal{B} independent studies and their estimated $\pm 1\sigma$ uncertainties. The values $\log_{10} J$ (\mathcal{GS} set) [45] correspond to the mean J -factor values for a source extension truncated at the outermost observed star. The values $\log_{10} J$ (\mathcal{B} set) [47] are provided for a source extension at the tidal radius of each dSph. Bolded sources are within HAWC's field of view and provided to the Glory Duck analysis.	34
77	Table 6.2	Summary of dSph observations by each experiment used in this work. A '-' indicates the experiment did not observe the dSph for this study. For Fermi-LAT, the exposure at 1 GeV is given. For HAWC, $ \Delta\theta $ is the absolute difference between the source declination and HAWC latitude. HAWC is more sensitive to sources with smaller $ \Delta\theta $. For IACTs, we show the zenith angle range, the total exposure, the energy range, the angular radius θ of the signal or ON region, the ratio of exposures between the background-control (OFF) and signal (ON) regions (τ), and the significance of gamma-ray excess in standard deviations, σ .	35
86	Table 7.1	Summary of the relevant properties of the dSphs used in the present work. Column 1 lists the dSphs. Columns 2 and 3 present their heliocentric distance and galactic coordinates, respectively. Column 4 reports the J -factors of each source given from the \mathcal{LS} studies and estimated $\pm 1\sigma$ uncertainties. The values $\log_{10} J$ (\mathcal{LS} set) [65] correspond to the mean J -factor values for a source extension truncated at 0.5° .	63
92	Table 7.2	Timing summaries for analyses for serial and multithreaded processes. M tasks is the number of functional-parallel tasks ran for the computation. $T_{p,c}$ is a single run time in hours:minutes:seconds for runs utilizing p nodes and c threads. Runs are run interactively on the same computer to maximize consistency. Empty entries are indicated with '-'. (\cdot) entries are estimated entries extrapolated from data earlier in the column.	69
98	Table 7.3	Speed up summaries for analyses for serial and multithreaded processes. M tasks is the number of functional-parallel tasks ran for the computation. $S_{p,c}$ is a single speedup comparison for runs utilizing p nodes and c threads. $[\cdot]$ are the estimated speedups calculated from Tab. 7.2, Eq. (7.10), and Eq. (7.5). Empty entries are indicated with '-'.	71
103	Proof I know how to include		

LIST OF FIGURES

105	Figure 2.1	Rotation curve fit to NGC 6503 from [7]. Dashed line is the contribution 106 from visible matter. Dotted curves are from gas. Dash-dot curves are from 107 dark matter (DM). Solid line is the composite contribution from all matter 108 and DM sources. Data are indicated with bold dots with error bars. Data 109 agree strongly with a matter + DM composite prediction.	5
110	Figure 2.2	Light from distant galaxy is bent in unique ways depending on the distribution 111 of mass between the galaxy and Earth. Yellow dashed lines indicate where 112 the light would have gone if the matter were not present [8].	7
113	Figure 2.3	(left) Optical image of galactic cluster 1E0657-558. (right) X-ray image of the 114 cluster with redder meaning hotter and higher baryon density. (both) Green 115 contours are reconstruction of gravity contours from weak lensing. White 116 rings are the best fit mass maxima at 68.3%, 95.5%, and 99.7% confidence. 117 The matter maxima of the clusters are clearly separated from x-ray maxima. [9]	8
118	Figure 2.4	Plank CMB sky. Sky map features small variations in temperature in primor- 119 dial light. These anisotropies are used to make inferences about the universe's 120 energy budget and developmental history. [10]	9
121	Figure 2.5	Observed Cosmic Microwave Background power spectrum as a function of 122 multipole moment from Plank [10]. Blue line is best fit model from Λ CDM. 123 Red points and lines are data and error, respectively.	10
124	Figure 2.6	Predicted power spectra of CMB for different $\Omega_m h^2$ values for fixed baryon 125 density from [11]. (left) Low $\Omega_m h^2$ increases the prominence of first and 126 second peaks. (middle) $\Omega_m h^2$ is most similar to the observed power spectrum. 127 The second and third peaks are similar in height. (right) $\Omega_m h^2$ is large which 128 suppresses the first peak and raises the prominence of the third peak.	10
129	Figure 2.7	The Standard Model (SM) of particle physics. Figure taken from http://www.quantumdiaries.org/2014/03/14/the-standard-model-a-beautiful-but-flawed-theory/	12
132	Figure 2.8	Simplified Feynman diagram demonstrating with different ways DM can 133 interact with SM particles. The 'X's refer to the DM particles whereas the 134 SM refer to fundamental particles in the SM. The large circle in the center 135 indicates the vertex of interaction and is purposely left vague. The colored 136 arrows refer to different directions of time as well as their respective labels. 137 The arrows indicate the initial and final state of the DM -SM interaction in time.	13

138	Figure 2.9 A single jet event in ATLAS detector from 2017 [16]. Jet momentum was 139 observed to be 1.9 TeV. Missing transverse momentum was observed to be 140 1.9 TeV compared to the initial transverse momentum of the event was 0. 141 Implied MET is traced by a red dashed line in event display.	14
142	Figure 2.10 More detailed pseudo-Feynman diagram of particle cascade from dark matter 143 annihilation into 2 quarks. The quarks hadronize and down to stable particles 144 like γ or the anti-proton (p^-). Diagram pulled from ICRC 2021 presentation 145 on DM annihilation search [17].	15
146	Figure 2.11 Dark Matter (DM) decay spectrum for $b\bar{b}$ initial state and γ final state. Redder 147 spectra are for larger DM masses. Bluer spectra are light DM masses. x is a 148 unitless factor defined as the ratio of the mass of DM, m_χ , and the final state 149 particle energy E_γ . Figure from [19].	17
150	Figure 2.12 Different dark matter density profiles compared. Some models produce ex- 151 ceptionally large densities at small r [20].	18
152	Figure 2.13 The Milky Way Galaxy in photons (γ) and neutrinos (ν) [22]. The Galactic 153 center is at $l=0^\circ$ and is the brightest region in all panels. (top) An Optical 154 color image of the Milky Way galaxy seen from Earth. Clouds of gas and dust 155 obscure some light from stars. (2nd down) Integrated flux of γ -rays observed 156 by the Fermi-LAT telescope [23]. (middle) Expected neutrino emission 157 that corresponds with Fermi-LAT observations. (2nd up) Expected neutrino 158 emission profile after considering detector systematics of IceCube. (bottom) 159 Observed neutrino emission from region of the galactic plane. Substantial 160 neutrino emission was detected.	19
161	Figure 2.14 Dark Matter annihilation spectra for different final state particle and standard 162 model annihilation channels [24]. Photons (red), e^\pm (green), \bar{p} (blue), ν (black).	20
163	Figure 3.1 TODO: Show a nuclear reactor with cherenkov radiation[NEEDS A SOURCE][FACT 164 CHECK THIS]	22
165	Figure 3.2 TODO: absorption spectrum of liquid and solid water[NEEDS A SOURCE][FACT 166 CHECK THIS]	23

167	Figure 6.1 Sensitivities of five gamma-ray experiments compared to percentages of the 168 Crab nebula's emission and dark matter annihilation. Solid lines present 169 estimated sensitivities to power law spectra [FACT CHECK THIS]for each 170 experiment. Green lines are Fermi-LAT sensitivities where lighter green is 171 the sensitivity to the galactic center and dark green is its sensitivity to higher 172 declinations. Orange, red, and purple solid lines represent the MAGIC, HESS, 173 and VERITAS 50 hour sensitivities respectively. The maroon and brown lines 174 are the HAWC 1 year and 5 year sensitivities. Across four decades of gamma- 175 ray energy, these experiments have similar sensitivities on the order 10^{-12} 176 erg cm $^{-2}$ s $^{-1}$. The dotted lines are estimated dark matter fluxes assuming 177 $m_\chi = 5$ TeV DM annihilating to bottom quarks (red), tau leptons (blue), 178 and W bosons (green). Faded gray lines outline percentage flux of the Crab 179 nebula. Figure is an augmented version of [25]	27
180	Figure 6.2 Effect of Electroweak (EW) corrections on expected DM annihilation spec- 181 trum for $\chi\chi \rightarrow W^-W^+$. Solid lines are spectral models that consider EW 182 corrections. Dash-dot lines are spectral models without EW corrections. Red 183 lines are models for $M_\chi = 1$ TeV. Blue lines represent models for $M_\chi = 100$ 184 TeV. All models are sourced from the PPPC4DMID [44].	31
185	Figure 6.3 $\frac{dJ}{d\Omega}$ maps for Segue1 (top) and Coma Berenices (bottom). Origin is centered 186 on the specific dwarf spheroidal galaxies (dSph). X and Y axes are the 187 angular separation from the center of the dwarf. Plots of the remaining 11 188 dSph HAWC studied are linked in Fig. A.1.	33
189	Figure 6.4 Illustration of the combination technique showing a comparison between 190 $-2 \ln \lambda$ provided by four instruments (colored lines) from the observation 191 of the same dSph without any J nuisance and their sum, <i>i.e.</i> the resulting 192 combined likelihood (thin black line). According to the test statistics of 193 Equation (6.6), the intersection of the likelihood profiles with the line $-2 \ln \lambda$ 194 = 2.71 indicates the 95% C.L. upper limit on $\langle \sigma v \rangle$. The combined likelihood 195 (thin black line) shows a smaller value of upper limit on $\langle \sigma v \rangle$ than those 196 derived by individual instruments. We also show how the uncertainties on 197 the J factor effects the combined likelihood and degrade the upper limit on 198 $\langle \sigma v \rangle$ (thick black line). All likelihood profiles are normalized so that the global 199 minimum $\widehat{\langle \sigma v \rangle}$ is 0. We note that each profile depends on the observational 200 conditions in which a target object was observed. The sensitivity of a given 201 instrument can be degraded and the upper limits less constraining if the 202 observations are performed in non-optimal conditions such as a high zenith 203 angle or a short exposure time.	38
204	Figure 6.5 HAWC upper limits at 95% confidence level on $\langle \sigma v \rangle$ versus DM mass for 205 seven annihilation channels, using the set of J -factors from Ref. [53] The 206 solid line represents the observed combined limit. Dashed lines represent 207 limits from individual dSphs.	41

208	Figure 6.6 HAWC TS values for best fit $\langle\sigma v\rangle$ versus m_χ for seven SM annihilation channels with J factors from \mathcal{GS} . The solid black line shows the combined best fit TS values. The colored, dashed lines are the TS values for each of the 13 sources HAWC studied.	42
212	Figure 6.7 HAWC Brazil bands at 95% confidence level on $\langle\sigma v\rangle$ versus DM mass for seven annihilation channels with J -factors from \mathcal{GS} [53]. The solid line represents the combined limit from 13 dSphs. The dashed line is the expected limit. The green band is the 68% containment. The yellow band is the 95% containment.	43
217	Figure 6.8 Upper limits at 95% confidence level on $\langle\sigma v\rangle$ in function of the DM mass for eight annihilation channels, using the set of J factors from Ref. [53] (\mathcal{GS} set in Table 6.1). The black solid line represents the observed combined limit, the black dashed line is the median of the null hypothesis corresponding to the expected limit, while the green and yellow bands show the 68% and 95% containment bands. Combined upper limits for each individual detector are also indicated as solid, colored lines. The value of the thermal relic cross-section in function of the DM mass is given as the red dotted-dashed line [54].	44
226	Figure 6.9 Same as Fig. 6.8, using the set of J factors from Ref. [47, 55] (\mathcal{B} set in Table 6.1).	45
227	Figure 6.10 Comparisons of the combined limits at 95% confidence level for each of the eight annihilation channels when using the J factors from Ref. [53] (\mathcal{GS} set in Table 6.1), plain lines, and the J factor from Ref. [47, 55] (\mathcal{B} set in Table 6.1), dashed lines. The cross-section given by the thermal relic is also indicated [54].	47
231	Figure 6.11 Comparisons of the combined limits at 95% confidence level for a point source analysis and extended source using [53] \mathcal{GS} J-factor distributions and PPPC [44] annihilation spectra. Shown are the limits for Segue1 which will have the most significant impact on the combined limit. 6 of the 7 DM annihilation channels are shown. Solid lines are extended source studies. Dashed lines are point source studies. Overall, the extended source analysis improves the limit by a factor of 2.	49
238	Figure 6.12 Same as Fig. 6.11 on Coma Berenices. This dSph also contributes significantly to the limit. The limits are identical in this case.	50
240	Figure 6.13 Comparison of combined limits when correcting for HAWC's pointing systematic. All DM annihilation channels are shown. The solid black line is the ratio between published limit to the declination corrected limit. The blue solid line or "Combined_og" represented the limits computed for Glory Duck. The solid orange line or "Combined_ad" represented the limits computed after correcting for the pointing systematic.	51

246	Figure 6.14 Differential map of dJ/Ω from model built in Section 6.8.1 and profiles provided directly from authors. (Top) Differential from Segue1. (bottom) Differential from Coma Berenices. Note that their scales are not the same. Segue1 shows the deepest discrepancies which is congruent with its large uncertainties. Both models show anuli where unique models become apparent.	52
251	Figure 6.15 HAWC limits for Coma Berenices (top) and Segue1 (bottom) for two different map sets. Blue lines are limits calculated on maps with poor model representation. Orange lines are limits calculated on spatial profiles provided by the authors of [45]. Black line is the ratio of the poor spatial model limits to the corrected spatial models. The left y-axis measures $\langle\sigma v\rangle$ for the blue and orange lines. The right y-axis measures the ratio and is unitless.	53
257	Figure 6.16 Comparisons between the J -factors versus the angular radius for the computation of J factors from Ref. [53] (\mathcal{GS} set in Table 6.1) in blue and for the computation from Ref. [47, 55] (\mathcal{B} set in Tab. 6.1) in orange. The solid lines represent the central value of the J -factors while the shaded regions correspond to the 1σ standard deviation.	56
262	Figure 6.17 Comparisons between the J -factors versus the angular radius for the computation of J factors from Ref. [53] (\mathcal{GS} set in Tab. 6.1) in blue and for the computation from Ref. [47, 55] (\mathcal{B} set in Tab. 6.1) in orange. The solid lines represent the central value of the J -factors while the shaded regions correspond to the 1σ standard deviation.	57
267	Figure 7.1 Difference between spectral hypotheses from PPPC [44] and HDM [64]. Shown is the expected DM annihilation spectrum for $\chi\chi \rightarrow W^-W^+$. Solid lines are spectral models with EW corrections from the PPPC. Dash-dot lines are spectral models from HDM. Red lines are models for $M_\chi = 1$ TeV. Blue lines represent models for $M_\chi = 100$ TeV.	62
272	Figure 7.2 Photon spectra for $\chi\chi \rightarrow \gamma\gamma$ (left) and $\chi\chi \rightarrow ZZ$ (right) after gaussian convolution of line features. Both spectra have δ -features at photon energies equal to the DM mass. Bluer lines are annihilation spectra with lower DM mass. Redder lines are spectra from larger DM mass. All Spectral models are sourced from the Heavy Dark Matter models [64]. Axes are drawn roughly according to the energy sensitivity of HAWC.	63
278	Figure 7.3 $\frac{dJ}{d\Omega}$ maps for Coma Berenices, Draco, Segue1, and Sextans. Columns are divided for the $\pm 1\sigma$ uncertainties in $dJ/d\Omega$ around the mean value from \mathcal{LS} [65]. Origin is centered on the specific dwarf spheroidal galaxies (dSph). θ and ϕ axes are the angular separation from the center of the dwarf	64

282	Figure 7.4	Infographic on how jobs and DM computation was organized in Section 6.3. Jobs were built for each permutation of CHANS and SOURCES shown by the left block in the figure. Each job, which took on the order 2 hrs to compute, had the following work flow: 1. Import HAWC analysis software, 2 min to run. 2. Load HAWC count maps, 5 min to run. 3. Load HAWC energy and spatial resolutions, 4 min. 5. Load DM spatial source templates and spectral models, less than 1 s. 6. Perform likelihood fit on data and model, about 8 min per DM mass. 7. Write results to file, less than 1s.	66
290	Figure 7.5	Graphic of Gustafson parallel coding pattern. f_s is the fraction of a program, in time, spent on serial computation. f_p is the fraction of computing time that is parallelizable. T_p is the total time for a parallel program to run. T_1 is the total time for a parallel program to run if only 1 processor is allocated. P_N is the N -th processor where it's row is the computation the processor performs. The Gustafson pattern is most similar to what is implemented for this analysis. Figure is pulled from [67].	67
297	Figure 7.6	Task chart for one multi-threaded job developed for this project. Green blocks indicate a shared resource across the threads AND computation performed serially. Red blocks indicate functional parallel processing within each thread. 3 threads are represented here, yet many more can be employed during the full analysis. Jobs are defined by the SOURCE as these require unique maps to be loaded into the likelihood estimator. The m_χ , CHAN, and $\langle\sigma v\rangle$ variables are entered into the thread pool and allocated as evenly as possible across the threads.	69
305	Figure 7.7	TODO: fill this out	72
306	Figure 7.8	TODO: fill this out	73
307	Figure 7.9	TODO: TS of analysis of results. See if we can include Draco[NEEDS A SOURCE][FACT CHECK THIS]	74
309	Figure 7.10	TODO: TS of analysis of results. There will definitely be 2[NEEDS A SOURCE][FACT CHECK THIS]	75
311	Figure 7.11	TODO: Comparison of channels with GD combined results.[NEEDS A SOURCE][FACT CHECK THIS]	76
313	Figure 7.12	TODO: show p1 and m1 limits around[NEEDS A SOURCE][FACT CHECK THIS]	77
315	Figure 7.13	TODO: there will be 2[NEEDS A SOURCE][FACT CHECK THIS]	78

316	Figure A.1 Sister figure to Figure 6.3. Sources in the first row from left to right: Bootes 317 I, Canes Venatici I, II. In second row: Draco, Hercules, Leo I. In the first row: 318 Leo II, Leo IV, Sextans. In the final row: Ursa Major I, Ursa Major II.	81
319	Figure B.1 Sister figure to Figure 7.2 for remaining SM primary annihilation channels 320 studied for this thesis. These did not require any post generation smoothing 321 and so are directly pulled from [64] with a binning scheme most helpful for a 322 HAWC analysis.	82

LIST OF ABBREVIATIONS

- 324 **MSU** Michigan State University
325 **LANL** Los Alamos National Laboratory
326 **DM** Dark Matter
327 **SM** Standard Model
328 **HAWC** High Altitude Water Cherenkov Observatory
329 **dSph** Dwarf Spheroidal Galaxy

330

CHAPTER 1

INTRODUCTION

331 Is the text not rendering right? Ah ok it knows im basically drafting the doc still

CHAPTER 2

332

DARK MATTER IN THE COSMOS

333 **2.1 Introduction**

334 The dark matter problem can be summarized in part by the following thought experiment.

335 Let us say you are the teacher for an elementary school classroom. You take them on a field
336 trip to your local science museum and among the exhibits is one for mass and weight. The exhibit
337 has a gigantic scale, and you come up with a fun problem for your class.

338 You ask your class, "What is the total weight of the classroom? Give your best estimation to
339 me in 30 minutes, and then we'll check your guess on the scale. If your guess is within 10% of the
340 right answer, we will stop for ice cream on the way back."

341 The students are ecstatic to hear this, and they get to work. The solution is some variation of
342 the following strategy. The students should give each other their weight or best guess if they do
343 not know. Then, all they must do is add each student's weight and get a grand total for the class.

344 The measurement on the giant scale should show the true weight of the class. When comparing
345 the measured weight to your estimation, multiply the measurement by 1.0 ± 0.1 to get the $\pm 10\%$
346 tolerances for your estimation.

347 Two of your students, Sandra and Mario, return to you with a solution.

348 They say, "We weren't sure of everyone's weight. We used 65 lbs. for the people we didn't
349 know and added everyone who does know. There are 30 of us, and we got 2,000 lbs.! That's a ton!"

350 You estimated 1,900 lbs. assuming the average weight of a student in your class was 60 lbs.
351 So, you are pleased with Sandra's and Mario's answer. You instruct your students to all gather on
352 the giant scale and read off the weight together. To all your surprise, the scale reads *10,000 lbs.*!
353 10,000 is significantly more than a 10% error from 2,000. In fact, it is approximately 5 times more
354 massive than either your or your students' estimates. You think to yourself and conclude there
355 must be something wrong with the scale. You ask an employee to check the scale and verify it is
356 well calibrated. They confirm that the scale is in working order. You weigh a couple of students
357 individually to assess that the scale is well calibrated. Sandra weighs 59 lbs., and Mario weighs

358 62 lbs., typical weights for their age. You then weigh each student individually and see that their
359 weights individually do not deviate greatly from 60 lbs. So, where does all the extra weight come
360 from?

361 This thought experiment serves as an analogy to the Dark Matter problem. The important
362 substitution to make however is to replace the students with stars and the classroom with a galaxy,
363 say the Milky Way. Individually the mass of stars is well measured and defined with the Sun as our
364 nearest test case. However, when we set out to measure the mass of a collection of stars as large as
365 galaxies, our well-motivated estimation is wildly incorrect. There simply is no way to account for
366 this discrepancy except without some unseen, or dark, contribution to mass and matter in galaxies.
367 I set out in my thesis to narrow the possibilities of what this Dark Matter could be.

368 This chapter is organized like the following... **TODO: Text should look like ... Chapter x has**
369 **blah blah blah.**

370 2.2 Dark Matter Basics

371 Presently, a more compelling theory of cosmology that includes Dark Matter (DM) in order
372 to explain a variety of observations is Λ Cold Dark Matter, or Λ CDM. I present the evidence
373 supporting Λ CDM in Section 2.3 yet discuss the conclusions of the Λ CDM model here. According
374 to Λ CDM fit to observations on the Cosmic Microwave Background (CMB), DM is 26.8% of the
375 universe's current energy budget. Baryonic matter, stuff like atoms, gas, and stars, contributes to
376 4.9% of the universe's current energy budget [1, 2, 3].

377 DM is dark; it does not interact readily with light at any wavelength. DM also does not interact
378 noticeably with the other standard model forces (Strong and Weak) at a rate that is readily observed
379 [3]. DM is cold, which is to say that the average velocity of DM is below relativistic speeds [1].
380 'Hot' DM would not likely manifest the dense structures we observe like galaxies, and instead
381 would produce much more diffuse galaxies than what is observed [3, 1]. DM is old; it played a
382 critical role in the formation of the universe and the structures within it [1, 2].

383 Observations of DM have so far been only gravitational. The parameter space available to what
384 DM could be therefore is extremely broad. The broad DM parameter space is iteratively tested in

385 DM searches by supposing a hypothesis that has not yet been ruled out and performing observations
386 to test them. When the observations yield a null result, the parameter space is constrained further.
387 I present some approaches for DM searches in Section 2.4.

388 **2.3 Evidence for Dark Matter**

389 Dark Matter (DM) has been a looming problem in physics for almost 100 years. Anomalies
390 have been observed by astrophysicists in galactic dynamics as early as 1933 when Fritz Zwicky
391 noticed unusually large velocity dispersion in the Coma cluster. Zwicky's measurement was the
392 first recorded to use the Virial theorem to measure the mass fraction of visible and invisible matter
393 in celestial bodies [4]. From Zwicky in [5], "*If this would be confirmed, we would get the surprising*
394 *result that dark matter is present in much greater amount than luminous matter.*" Zwicky's and
395 others' observation did not instigate a crisis in astrophysics because the measurements did not
396 entirely conflict with their understanding of galaxies [4]. In 1978, Rubin, Ford, and Norbert
397 measured rotation curves for ten spiral galaxies [6]. Rubin et al.'s 1978 publication presented a
398 major challenge to the conventional understanding of galaxies that could no longer be dismissed by
399 measurement uncertainties. Evidence has been mounting ever since for this exotic form of matter.
400 The following subsections provide three compelling pieces of evidence in support of the existence
401 of DM.

402 **2.3.1 First Clues: Stellar Velocities**

403 Zwicky, and later Rubin, measured the stellar velocities of various galaxies to estimate their
404 virial mass. The Virial Theorem upon which these observations are interpreted is written as

$$2T + V = 0. \quad (2.1)$$

405 Where T is the kinetic energy and V is the potential energy in a self-gravitating system. The
406 classical Newton's law of gravity from stars and gas was used for gravitational potential modeled in
407 the observed galaxies:

$$V = -\frac{1}{2} \sum_i \sum_{j \neq i} \frac{m_i m_j}{r_{ij}}. \quad (2.2)$$

408 Zwicky et al. measured just the velocities of stars apparent in optical wavelengths [5]. Rubin et al.
 409 added by measuring the velocity of the hydrogen gas via the 21 cm emission line of Hydrogen [6].
 410 The velocities of the stars and gas are used to infer the total mass of galaxies and galaxy clusters
 411 via Equation (2.1). An inferred mass is obtained from the luminosity of the selected sources. The
 412 two inferences are compared to each other as a luminosity to mass ratio which typically yielded [1]

$$\frac{M}{L} \sim 400 \frac{M_{\odot}}{L_{\odot}} \quad (2.3)$$

413 M_{\odot} and L_{\odot} referring to stellar mass and stellar luminosity, respectively. These ratios clearly indicate
 414 a discrepancy in apparent light and mass from stars and gas and their velocities.

415 Rubin et al. [6] demonstrated that the discrepancy was unlikely to be an underestimation of
 416 the mass of the stars and gas. The inferred "dark" mass was up to 5 times more than the luminous
 417 mass. This dark mass also needed to extend well beyond the extent of the luminous matter.

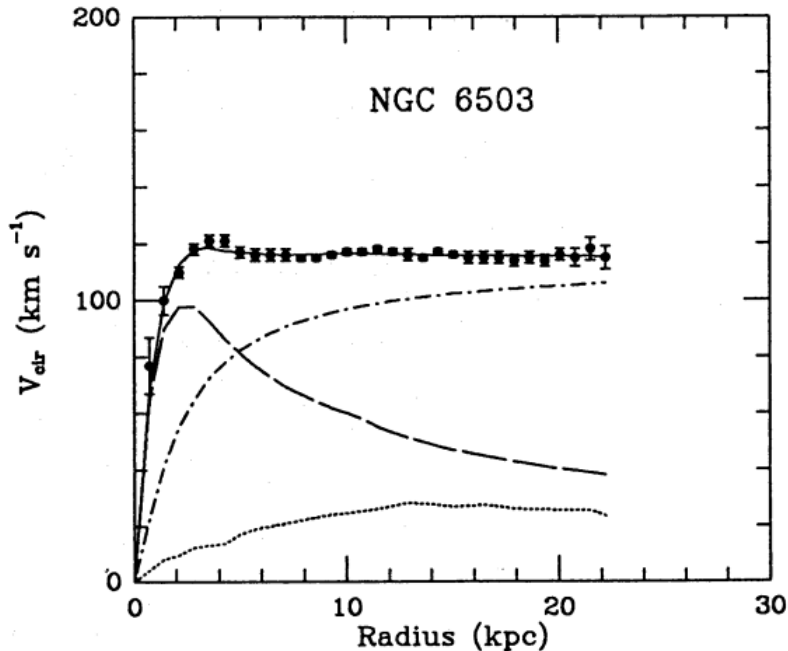


Figure 2.1 Rotation curve fit to NGC 6503 from [7]. Dashed line is the contribution from visible matter. Dotted curves are from gas. Dash-dot curves are from dark matter (DM). Solid line is the composite contribution from all matter and DM sources. Data are indicated with bold dots with error bars. Data agree strongly with a matter + DM composite prediction.

418 Figure 2.1 features one of many rotation curves plotted from the stellar velocities within galaxies.

419 The measured rotation curves mostly feature a flattening of velocities at higher radius which is not
420 expected if the gravity was only coming from gas and luminous matter. The extension of the
421 flat velocity region also indicates that the DM is distributed far from the center of the galaxy.
422 Modern velocity measurements include significantly larger objects, galactic clusters, and smaller
423 objects, dwarf galaxies. Yet, measurements along this regime are leveraging the Virial theorem
424 with Newtonian potential energies. We know Newtonian gravity is not a comprehensive description
425 of gravity. New observational techniques have been developed since 1978, and those are discussed
426 in the following sections.

427 **2.3.2 Evidence for Dark Matter: Gravitational Lensing**

428 Modern evidence for dark matter comes from new avenues beyond stellar velocities. Grav-
429 itational lensing from DM is a new channel from general relativity. General relativity predicts
430 aberrations in light caused by massive objects. In recent decades we have been able to measure the
431 lensing effects from compact objects and DM halos. Figure 2.2 shows how different massive ob-
432 jects change the final image of a faraway galaxy resulting from gravitational lensing. Gravitational
433 lensing developed our understanding of dark matter in two important ways.

434 Gravitational lensing provides additional compelling evidence for DM. The observation of two
435 merging galactic clusters in 2006, shown in Figure 2.3, provided a compelling argument for DM
436 outside the Standard Model. These clusters merged recently in astrophysical time scales. Galaxies
437 and star cluster have mostly passed by each other as the likelihood of their collision is low. Therefore,
438 these massive objects will mostly track the highest mass, dark and/or baryonic, density. Yet, the
439 intergalactic gas is responsible for the majority of the baryonic mass in the systems [4]. These gas
440 bodies will not phase through and will heat up as they collide together. The hot gas is located via
441 x-ray emission from the cluster. Two observations of the clusters were performed independently of
442 each other.

443 The first was the lensing of light around the galaxies due to their gravitational influences.
444 When celestial bodies are large enough, the gravity they exert bends space and time itself. The
445 warped space-time lenses light and will deflect in an analogous way to how glass lenses will bend

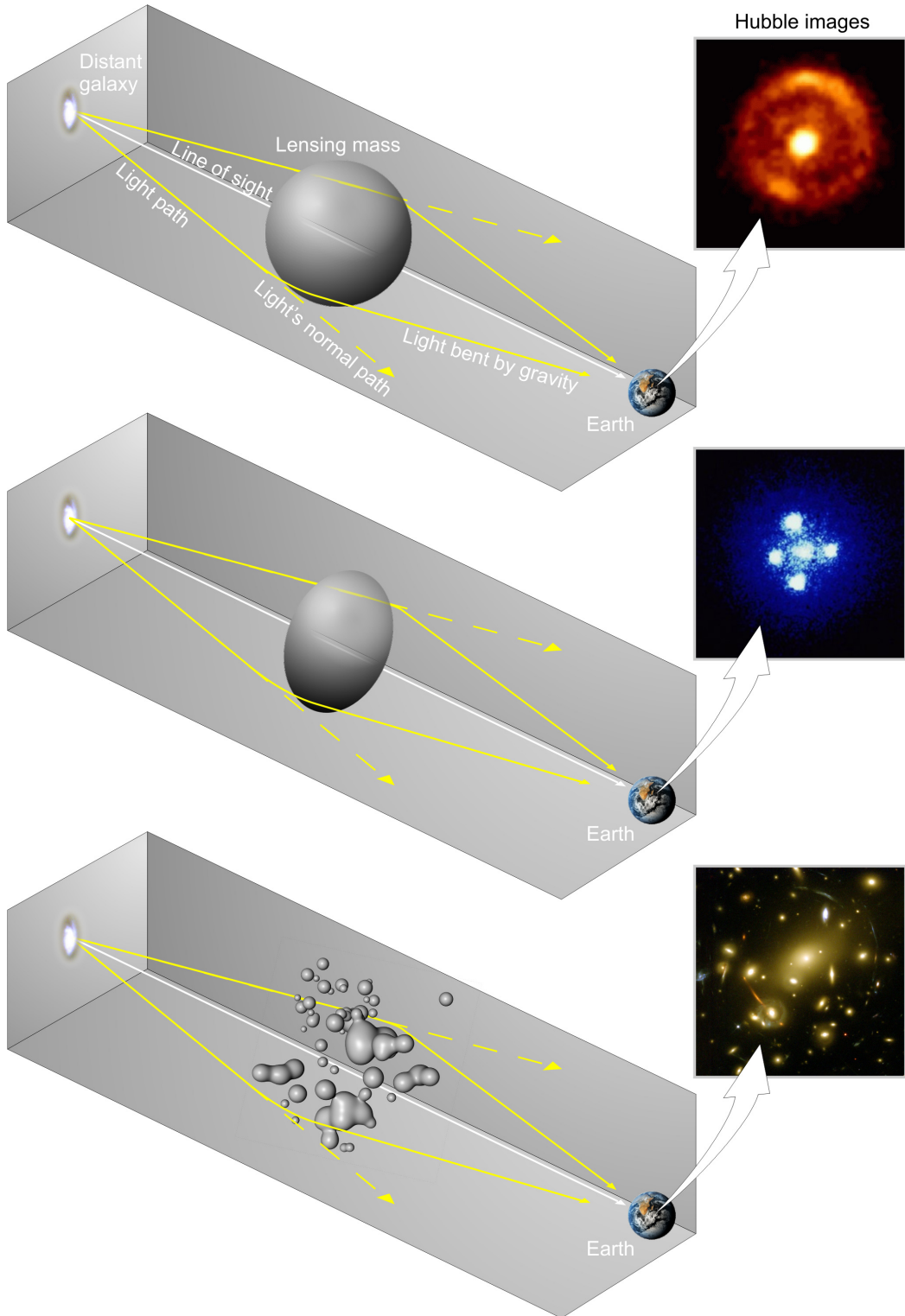


Figure 2.2 Light from distant galaxy is bent in unique ways depending on the distribution of mass between the galaxy and Earth. Yellow dashed lines indicate where the light would have gone if the matter were not present [8].

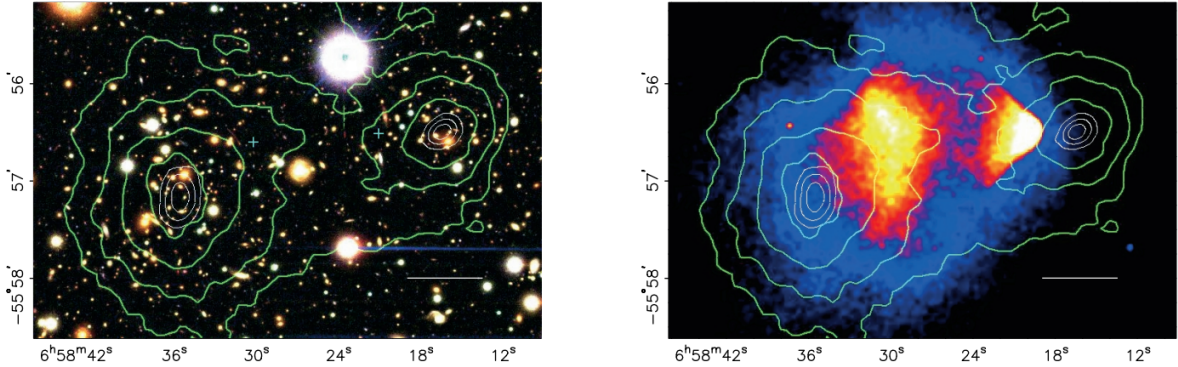


Figure 2.3 (left) Optical image of galactic cluster 1E0657-558. (right) X-ray image of the cluster with redder meaning hotter and higher baryon density. (both) Green contours are reconstruction of gravity contours from weak lensing. White rings are the best fit mass maxima at 68.3%, 95.5%, and 99.7% confidence. The matter maxima of the clusters are clearly separated from x-ray maxima. [9]

446 light, see Figure 2.2. With a sufficient understanding of light sources behind a massive object, we
 447 can reconstruct the contours of the gravitational lenses. The gradient of the contours shown in
 448 Figure 2.3 then indicates how dense the matter is and where it is.

449 The x-ray emission can then be observed from the clusters. Since these galaxies are mostly gas
 450 and are merging, then the gas should be getting hotter. If they are merging, the x-ray emissions
 451 should be the strongest where the gas is mostly moving through each other. Hence, X-ray emission
 452 maps out where the gas is in the merging galaxy cluster.

453 The lensing and x-ray observations were done on the Bullet cluster featured on Figure 2.3.
 454 The x-ray emissions do not align with the gravitational contours from lensing. The incongruence
 455 in mass density and baryon density suggests that there is a lot of matter somewhere that does
 456 not interact with light. Moreover, this dark matter cannot be baryonic [9]. The Bullet Cluster
 457 measurement did not really tell us what DM is exactly, but it did give the clue that DM also does
 458 not interact with itself very strongly. If DM did interact strongly with itself, then it would have been
 459 more aligned with the x-ray emission [9]. There have been follow-up studies of galaxy clusters with
 460 similar results. The Bullet Cluster and others like it provide a persuasive case against something
 461 possibly amiss in our gravitational theories.

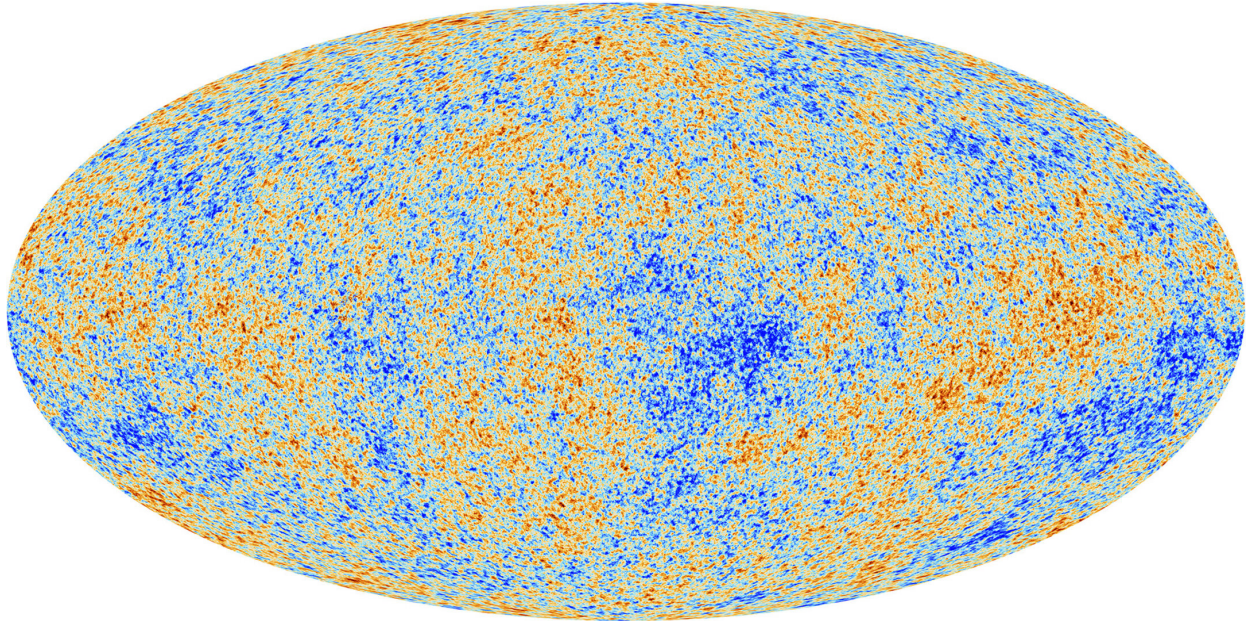


Figure 2.4 Plank CMB sky. Sky map features small variations in temperature in primordial light. These anisotropies are used to make inferences about the universe’s energy budget and developmental history. [10]

462 **2.3.3 Evidence for Dark Matter: Cosmic Microwave Background**

463 The Cosmic Microwave Background (CMB) is the primordial light from the early universe
464 when Hydrogen atoms formed from the free electron and proton soup in the early universe. The
465 CMB is the earliest light we can observe; released when the universe was about 380,000 years old.
466 Then we look at how the simulated universes look like compared to what we see. Figure 2.4 is the
467 most recent CMB image from the Plank satellite after subtracting the average value and masking the
468 galactic plane [10]. Redder regions indicate a slightly hotter region in the CMB, and blue indicates
469 colder. The intensity variations are on the order of 1 in 1000 with respect to the average value.

470 The Cosmic Microwave Background shows that the universe had DM in it from an incredibly
471 early stage. To measure the DM, Dark Energy, and matter fractions of the universe from the CMB,
472 the image is analyzed into a power spectrum, which shows the amplitude of the fluctuations as
473 a function of spherical multipole moments. Λ CDM provides the best fit to the power spectra of
474 the CMB as shown in Figure 2.5. The CMB power spectrum is quite sensitive to the fraction
475 of each energy contribution in the early universe. Low l modes are dominated by variations
476 in gravitational potential. Intermediate l emerge from oscillations in photon-baryon fluid from

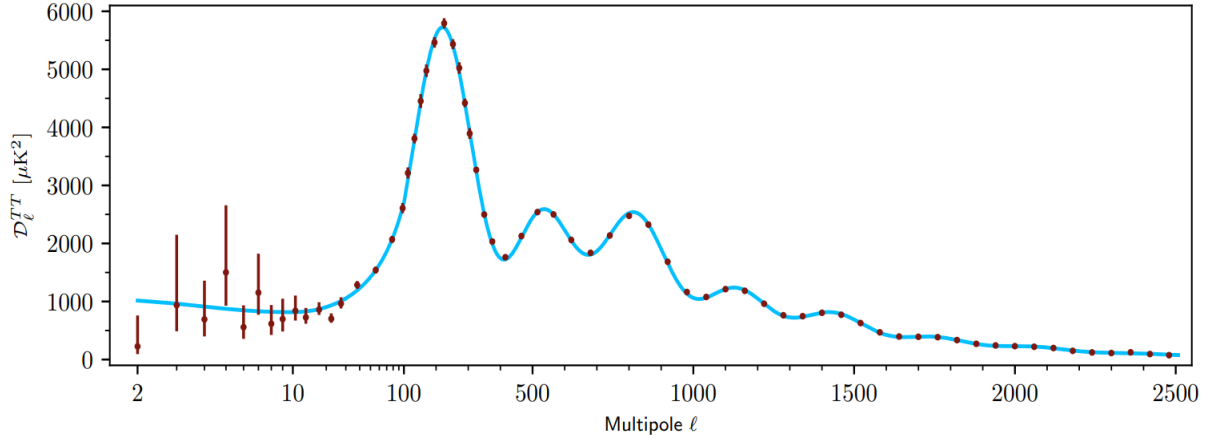


Figure 2.5 Observed Cosmic Microwave Background power spectrum as a function of multipole moment from Plank [10]. Blue line is best fit model from Λ CDM. Red points and lines are data and error, respectively.

477 competing baryon pressures and gravity. High l is a damped region from the diffusion of photons
 478 during electron-proton recombination. [1]

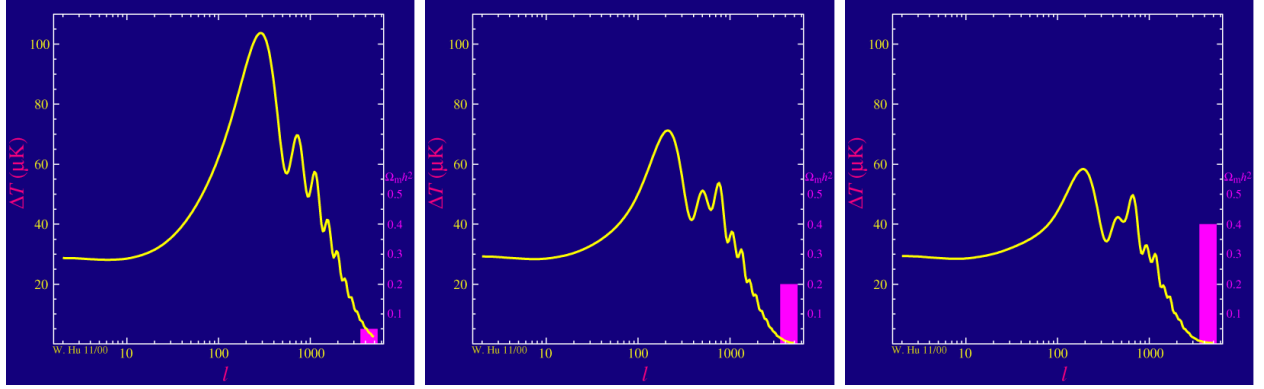


Figure 2.6 Predicted power spectra of CMB for different $\Omega_m h^2$ values for fixed baryon density from [11]. (left) Low $\Omega_m h^2$ increases the prominence of first and second peaks. (middle) $\Omega_m h^2$ is most similar to the observed power spectrum. The second and third peaks are similar in height. (right) $\Omega_m h^2$ is large which suppresses the first peak and raises the prominence of the third peak.

479 The harmonics would look quite different for a universe with less DM. Figure 2.6 demonstrates
 480 the effect $\Omega_m h^2$ has on the expected power spectrum for fixed baryon matter density. [11] Sweeping
 481 $\Omega_m h^2$ in this way clearly shows the effect dark matter has on the CMB power spectrum. The
 482 observations fit well with the Λ CDM model, and the derived fractions are as follows. The matter
 483 fraction: $\Omega_m = 0.3153$; and the baryon fraction: $\Omega_b = 0.04936$ [10]. Plank's observations also
 484 provide a measure of the Hubble constant, H_0 . H_0 especially has seen a growing tension in the

485 past decade that continues to deepened with observations from instruments like the James Webb
486 Telescope [12, 13]. As Hubble tensions deepen, we may find that perhaps Λ **CDM**, despite its
487 successes, is missing some critical physics.

488 Overall, the Newtonian motion of stars in galaxies, weak lensing from galactic clusters, and
489 power spectra from primordial light form a compelling body of research in favor of dark matter.
490 It takes another leap of theory and experimentation to make observations of DM that are non-
491 gravitational in nature. In Section 2.3, the evidence for DM implies strongly that the DM is matter
492 and not a lost parameter in the gravitational fields between massive objects. Finally, if we take one
493 axiom: that this matter has quantum behavior, such as being described by some Bohr wavelength
494 and abiding by some fermion or boson statistics; then we arrive at particle dark matter. One particle
495 DM hypothesis is the Weakly Interacting Massive Particle (WIMP). This DM candidate theory is
496 discussed further in the next section and is the focus of this thesis.

497 **2.4 Searching for Dark Matter: Particle DM**

498 Section 2.4 shows the Standard Model of particle physics and is currently the most accurate
499 model for the dynamics of fundamental particles like electrons and photons. The current status
500 of the SM does not have a viable DM candidate. When looking at the standard model, we can
501 immediately exclude any charged particle because charged particles interact strongly with light.
502 Specifically, this will rule out the following charged, fundamental particles: $e, \mu, \tau, W, u, d, s, c, t, b$
503 and their corresponding antiparticles. Recalling from Section 2.2 that DM must be long-lived and
504 stable over the age of the universe which excludes all SM particles with decay half-lives at or shorter
505 than the age of the universe. The lifetime constraint additionally eliminates the Z and H bosons.
506 Finally, the candidate DM needs to be somewhat massive. Recall from Section 2.2 that DM is cold
507 or not relativistic through the universe. This eliminates the remaining SM particles: $\nu_{e,\mu,\tau}, g, \gamma$ as
508 DM candidates. Because there are no DM candidates within the SM, the DM problem strongly
509 hints to physics beyond the SM (BSM).

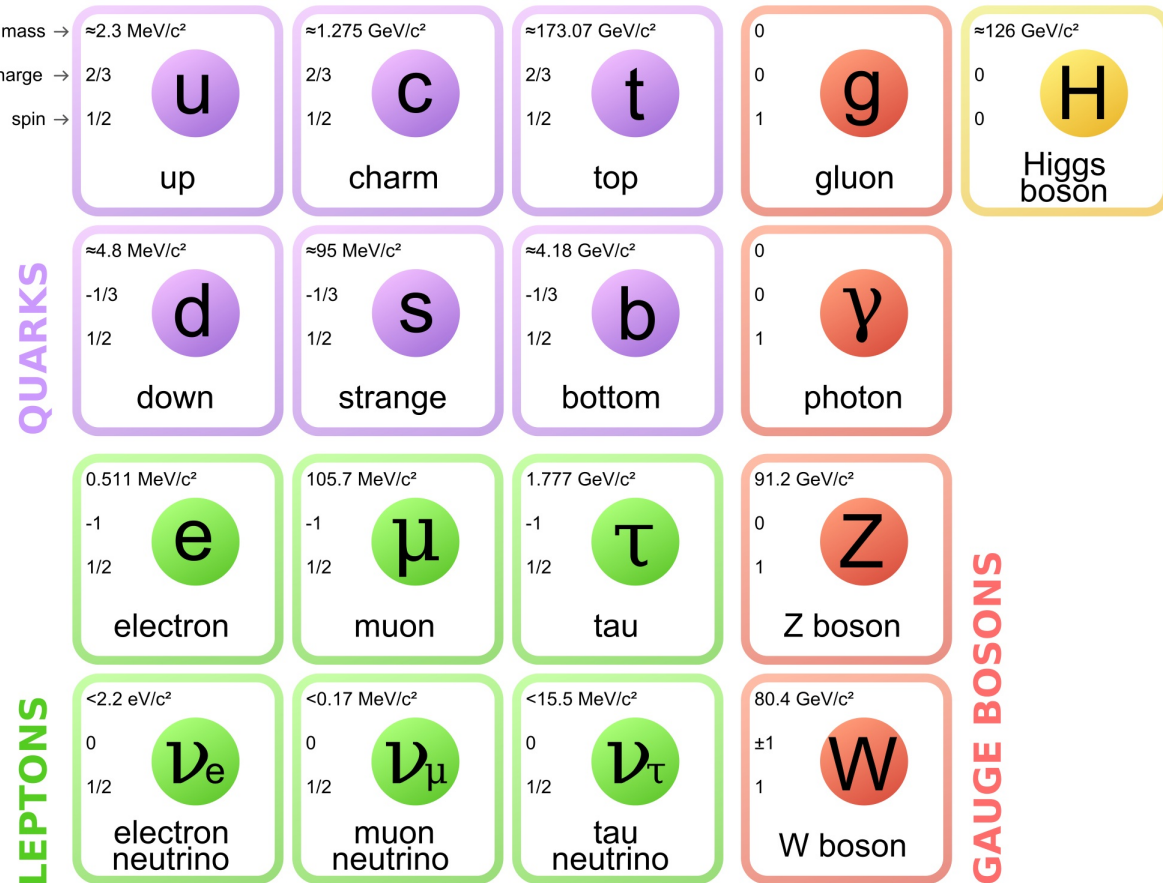


Figure 2.7 The Standard Model (SM) of particle physics. Figure taken from <http://www.quantumdiaries.org/2014/03/14/the-standard-model-a-beautiful-but-flawed-theory/>

510 2.4.1 Shake it, Break it, Make it

511 When considering DM that couples in some way with the SM, the interactions are roughly
 512 demonstrated by interaction demonstrated in Figure 2.8. The figure is a simplified Feynman
 513 diagram where the arrow of time represents the interaction modes of: **Shake it, Break it, Make it.**

514 **Shake it** refers to the direct detection of dark matter. Direct detection interactions start with
 515 a free DM particle and an SM particle. The DM and SM interact via elastic or inelastic collision
 516 and recoil away from each other. The DM remains in the dark sector and imparts some momentum
 517 onto the SM particle. The hope is that the momentum imparted onto the SM particle is sufficiently
 518 high enough to pick up with extremely sensitive instruments. Because we cannot create the DM in
 519 the lab, a direct detection experiment must wait until DM is incident on the detector. Most direct
 520 detection experiments are therefore placed in low-background environments with inert detection

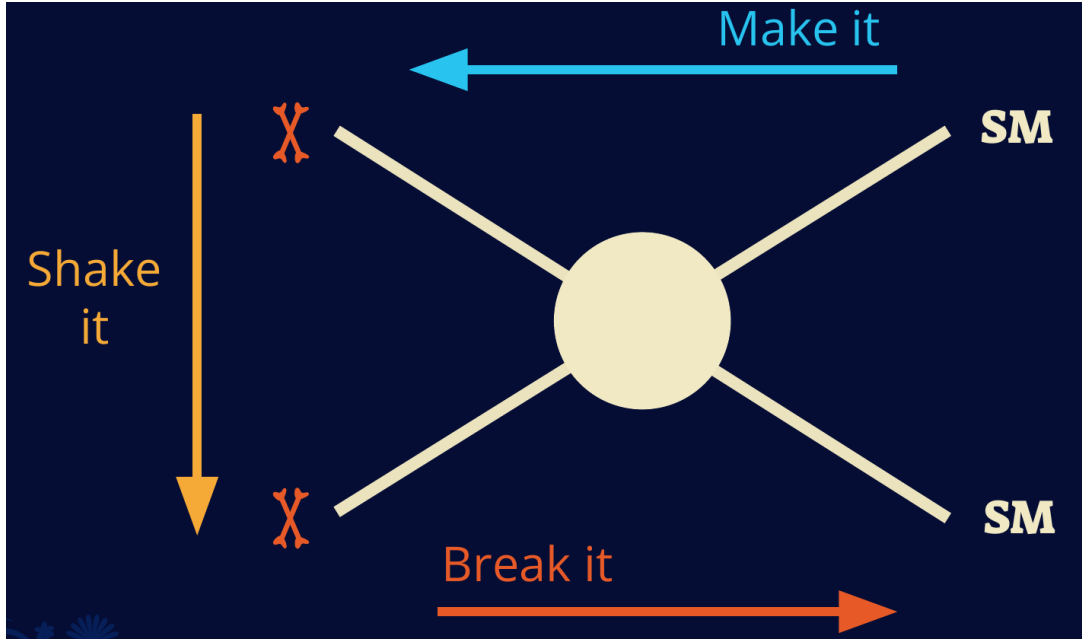


Figure 2.8 Simplified Feynman diagram demonstrating different ways DM can interact with SM particles. The 'X's refer to the DM particles whereas the SM refer to fundamental particles in the SM. The large circle in the center indicates the vertex of interaction and is purposely left vague. The colored arrows refer to different directions of time as well as their respective labels. The arrows indicate the initial and final state of the DM -SM interaction in time.

521 media like the noble gas Xenon. [14]

522 **Make it** refers to the production of DM from SM initial states. The experiment starts with
 523 particles in the SM. These SM particles are accelerated to incredibly high energies and then collide
 524 with each other. In the confluence of energy, DM hopefully emerges as a byproduct of the SM
 525 annihilation. Often it is the collider experiments that are energetic enough to hypothetically produce
 526 DM. These experiments include the world-wide collaborations ATLAS and CMS at CERN where
 527 proton collide together at extreme energies. The DM searches, however, are complex. DM likely
 528 does not interact with the detectors and lives long enough to escape the detection apparatus of
 529 CERN's colliders. This means any DM production experiment searches for an excess of events
 530 with missing momentum or energy in the events. An example event with missing transverse
 531 momentum is shown in Figure 2.9. The missing momentum with no particle tracks implies a
 532 neutral particle carried the energy out of the detector. However, there are other neutral particles
 533 in the SM, like neutrons or neutrinos, so any analysis has to account for SM signatures of missing

534 momentum. [15]

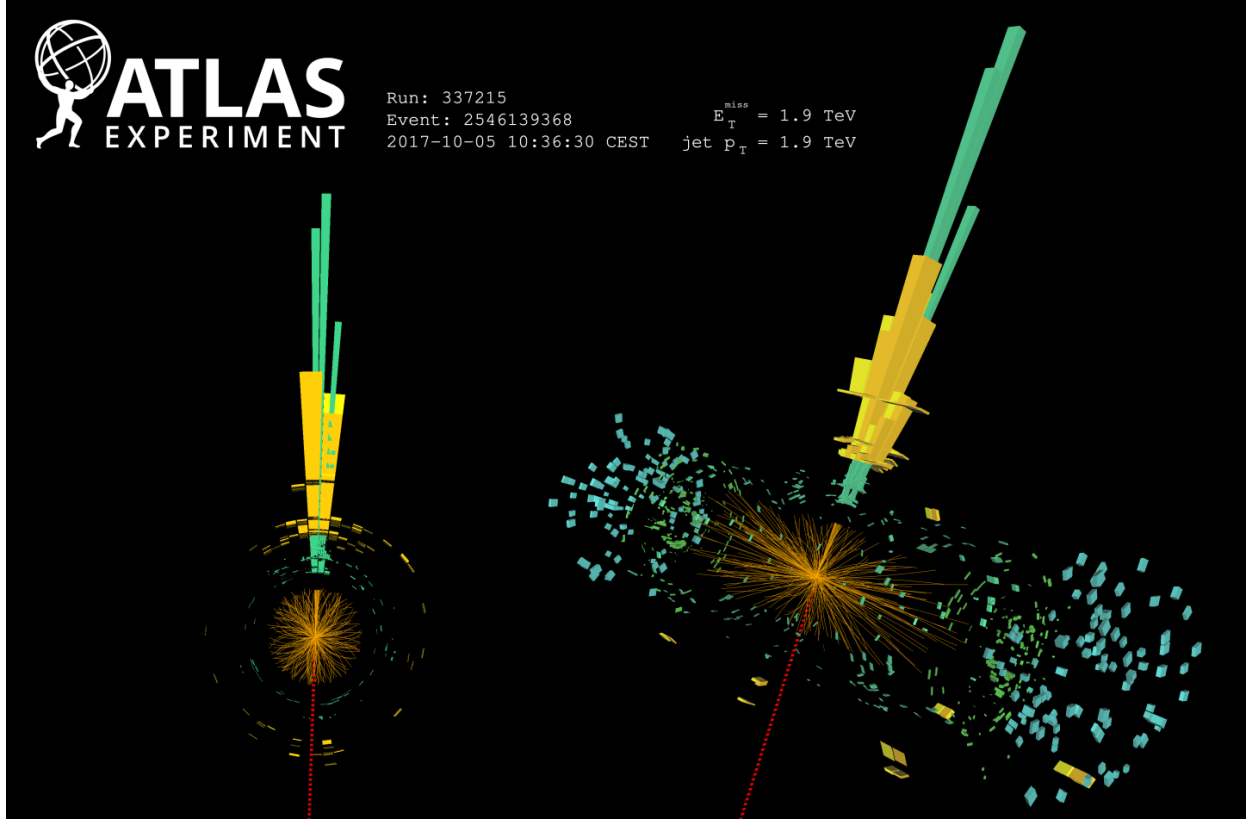


Figure 2.9 A single jet event in ATLAS detector from 2017 [16]. Jet momentum was observed to be 1.9 TeV. Missing transverse momentum was observed to be 1.9 TeV compared to the initial transverse momentum of the event was 0. Implied MET is traced by a red dashed line in event display.

535 2.4.2 Break it: Standard Model Signatures of Dark Matter through Indirect Searches

536 **Break it** refers to the creation of SM particles from the dark sector, and it is the primary focus
537 of this thesis. The interaction begins with DM or in the dark sector. The hypothesis is that this
538 DM will either annihilate with itself or decay and produce an SM byproduct. This method is
539 often referred to as the Indirect Detection of DM because we have no lab to directly control or
540 manipulate the DM. Therefore, most indirect DM searches are performed using observations of
541 known DM densities among the astrophysical sources. The strength is that we have the whole of the
542 universe and its 13.6-billion-year lifespan to use as a detector and particle accelerator. Additionally,
543 locations of dark matter are well cataloged since it was astrophysical observations that presented

544 the problem of DM in the first place.

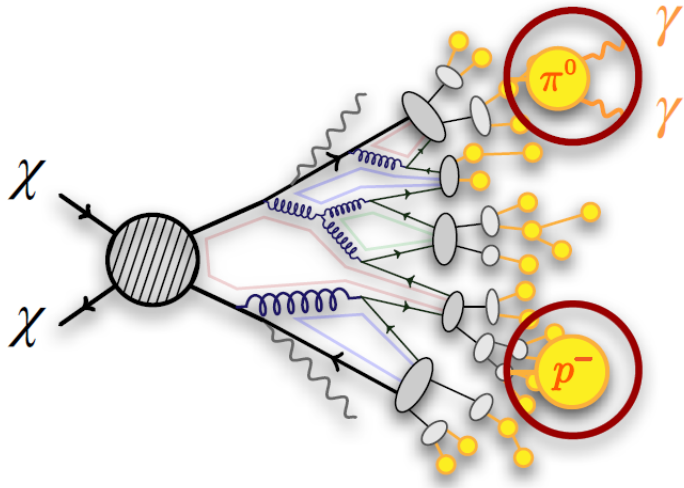


Figure 2.10 More detailed pseudo-Feynman diagram of particle cascade from dark matter annihilation into 2 quarks. The quarks hadronize and down to stable particles like γ or the anti-proton (p^-). Diagram pulled from ICRC 2021 presentation on DM annihilation search [17].

545 However, anything can happen in the universe. There are many difficult to deconvolve back-
546 grounds when searching for DM. One prominent example is the galactic center. We know the
547 galactic center has a large DM content because of stellar kinematics in our Milky Way and DM halo
548 simulations. Yet, any signal from the galactic center is challenging to parse apart from the extreme
549 environment of our supermassive black hole, unresolved sources, and diffuse emission from the
550 interstellar medium [18]. Despite the challenges, any DM model that yields evidence in the other
551 two observation methods, **Shake it or Make it** must be corroborated with indirect observations of
552 the known DM sources. Without corroborating evidence, DM observation in the lab is hard-pressed
553 to demonstrate that it is the model contributing to the DM seen at the universal scale.

554 In the case of WIMP DM, signals are described in terms of primary SM particles produced
555 from DM decay or annihilation. The SM initial state particles are then simulated down to stable
556 final states such as the γ , ν , p , or e which can traverse galactic lengths to reach Earth.

557 Figure 2.10 shows the quagmire of SM particles that emerges from SM initial states that are not
558 stable [17]. There are many SM particles with varying energies that can be produced in such an

559 interaction. For any arbitrary DM source and stable SM particle, the SM flux from DM annihilating
 560 to a neutral particle in the SM, ϕ , from a region in the sky is described by the following.

$$\frac{d\Phi_\phi}{dE_\phi} = \frac{\langle\sigma v\rangle}{8\pi m_\chi^2} \frac{dN_\phi}{dE_\phi} \times \int_{\text{source}} d\Omega \int_{l.o.s} \rho_\chi^2 dl(r, \theta') \quad (2.4)$$

561 In Equation (6.1), $\langle\sigma v\rangle$ is the velocity-weighted annihilation cross-section of DM to the SM. m_χ
 562 refers to the mass of DM, noted with Greek letter χ . $\frac{dN_\phi}{dE_\phi}$ is the N particle flux weighted by the
 563 particle energy. An example is provided in Figure 2.11 for the γ final state. The integrated terms
 564 are performed over the solid angle, $d\Omega$, and line of sight, l.o.s. ρ is the density of DM for a
 565 location (r, θ') in the sky. The terms left of the '×' are often referred to as the particle physics
 566 component. The terms on the right are referred to as the astrophysical component. For decaying
 567 DM, the equation changes to...

$$\frac{d\Phi_\phi}{dE_\phi} = \frac{1}{4\pi\tau m_\chi} \frac{dN_\phi}{dE_\phi} \times \int_{\text{source}} d\Omega \int_{l.o.s} \rho_\chi dl(r, \theta') \quad (2.5)$$

568 In Equation (7.1), τ is the decay lifetime of the DM. Just as in Equation (6.1), the left and right
 569 terms are the particle physics and the astrophysical components respectively. The integrated
 570 astrophysical component of Equation (6.1) is often called the J-Factor. Whereas the integrated
 571 astrophysical component of Equation (7.1) is often called the D-Factor.

572 Exact DM $\text{DM} \rightarrow \text{SM SM}$ branching ratios are not known, so it is usually assumed to go 100%
 573 into an SM particle/anti-particle. Additionally, when a DM annihilation or decay produces one of
 574 the neutral, long-lived SM particles (ν or γ), the particle is traced back to a DM source. For DM
 575 above GeV energies, there are very few SM processes that can produce particles with such a high
 576 energy. Seeing such a signal would almost certainly be an indication of the presence of dark matter.
 577 Fortunately, the universe provides us with the largest volume and lifetime ever for a particle physics
 578 experiment.

579 2.5 Sources for Indirect Dark Matter Searches

580 The first detection of DM relied on optical observations. Since then, we have developed new
 581 techniques to find DM dense regions. As described in Section 2.3.1, many DM dense regions were
 582 through observing galactic rotation curves. Our Milky Way galaxy is among DM dense regions

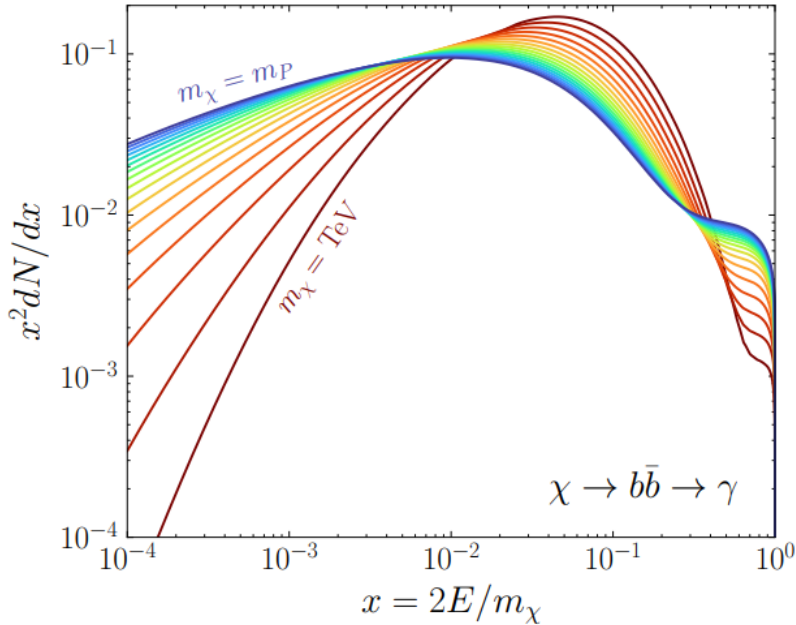


Figure 2.11 Dark Matter (DM) decay spectrum for $b\bar{b}$ initial state and γ final state. Redder spectra are for larger DM masses. Bluer spectra are light DM masses. x is a unitless factor defined as the ratio of the mass of DM, m_χ , and the final state particle energy E_γ . Figure from [19].

discovered, and it is the largest nearby DM dense region to look at. Additionally, the DM halo surrounding the Milky Way is clumpy [18]. There are regions in the DM halo of the Milky Way that have more DM than others that have captured gas over time. These sub-halos were dense enough to collapse gas and form stars. These apparent sub galaxies are known as dwarf spheroidal galaxies and are the main sources studied in this thesis. Each source type comes with different trade-offs. Galactic Center studies will be very sensitive to the assumed distribution of DM. The central DM density can vary substantially as demonstrated in Figure 2.12. At distances close to the center of the galaxy, or small r , the differences in DM densities can be 3-4 orders of magnitude. Searches toward the galactic center will therefore be quite sensitive to the assumed DM distribution.

Searches toward Dwarf Spheroidal Galaxies (dSph's) suffer from uncertainties in the DM density less than the galactic center studies. This is mostly from their diminutive size being smaller than the angular resolution of most γ -ray observatories [18]. The DM content dSph's are typically determined with the Virial theorem, Equation (2.1), and are usually majority DM [18] in mass. DSph's tend to be ideal sources to look at for DM searches. Their environments are quiet with little

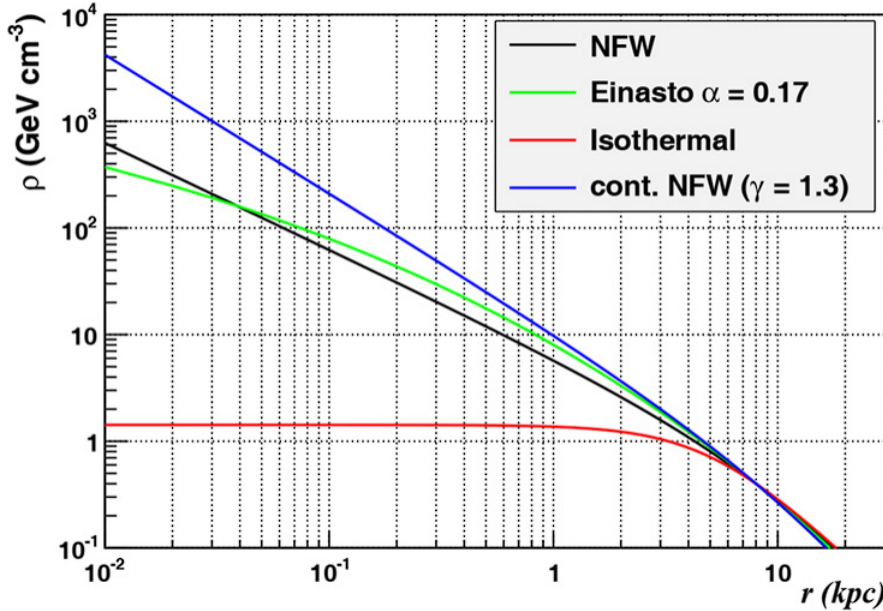


Figure 2.12 Different dark matter density profiles compared. Some models produce exceptionally large densities at small r [20].

597 astrophysical background. Unlike the galactic center, the most active components of dSph's are the
 598 stars within them versus a violent accretion disc around a black hole. All this together means that
 599 dSph's are among the best sources to look at for indirect DM searches. dSph's are the targets of
 600 focus for this thesis.

601 2.6 Multi-Messenger Dark Matter

602 Astrophysics entered a new phase in the past few decades that leverages our increasing sensitivity
 603 to SM channels and general relativity (GR). Up until the 21st century, astrophysical observations
 604 were performed with photons (γ) only. Astrophysics with this 'messenger' is fairly mature now.
 605 Novel observations of the universe have since only adjusted the sensitivity of the wavelength of
 606 light that is observed except at MeV energies. Gems like the CMB [10], and more have ultimately
 607 been observations of different wavelengths of light. Multi-messenger astrophysics proposes using
 608 other SM particles such the $p^{+/-}$, or ν or gravitation waves predicted by general relativity.

609 The experiment LIGO had a revolutionary discovery in 2016 with the first detection of a binary
 610 black hole merger [21]. This opened the collective imagination to observing the universe through
 611 gravitational waves. There has also been a surge of interest in the neutrino (ν) sector. IceCube

612 demonstrated that we are sensitive to neutrinos in regions that correlate with significant photon
 613 emission like the galactic plane [22]. Neutrinos, like gravitational waves and light, travel mostly
 614 unimpeded from their source to our observatories. This makes pointing to the originating source
 615 of these messengers much easier than it is for cosmic rays which are deflected from their source by
 616 magnetic fields.

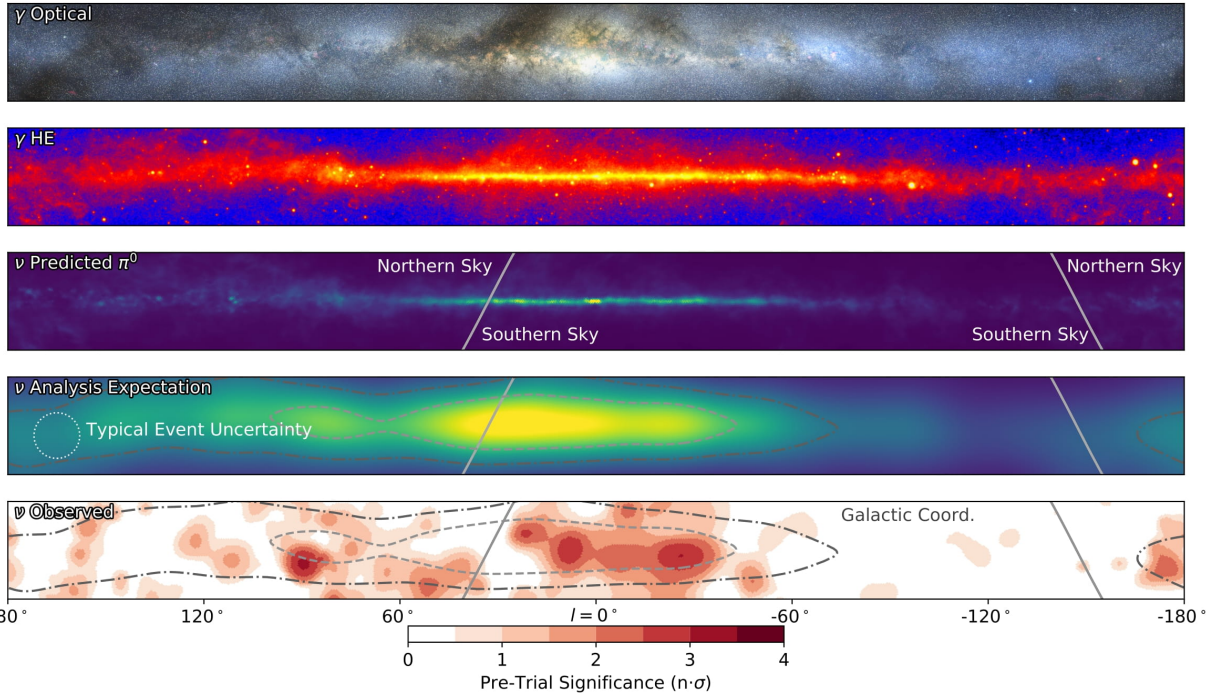


Figure 2.13 The Milky Way Galaxy in photons (γ) and neutrinos (ν) [22]. The Galactic center is at $l=0^\circ$ and is the brightest region in all panels. (top) An Optical color image of the Milky Way galaxy seen from Earth. Clouds of gas and dust obscure some light from stars. (2nd down) Integrated flux of γ -rays observed by the Fermi-LAT telescope [23]. (middle) Expected neutrino emission that corresponds with Fermi-LAT observations. (2nd up) Expected neutrino emission profile after considering detector systematics of IceCube. (bottom) Observed neutrino emission from region of the galactic plane. Substantial neutrino emission was detected.

617 The IceCube collaboration recently published a groundbreaking result of the Milky Way in
 618 neutrinos. The recent result from IceCube, shown in Figure 2.13, proves that we can make
 619 observations under different messenger regimes. The top two panels show the appearance of the
 620 galactic plane to different wavelengths of light. Some sources are more apparent in some panels,
 621 while others are not. This new channel is powerful because neutrinos are readily able to penetrate
 622 through gas and dust in the Milky Way. This new image also refines our understanding of how high

623 energy particles are produced. For example, the fit to IceCube data prefers neutrino production
 624 from the decay of π^0 [22].

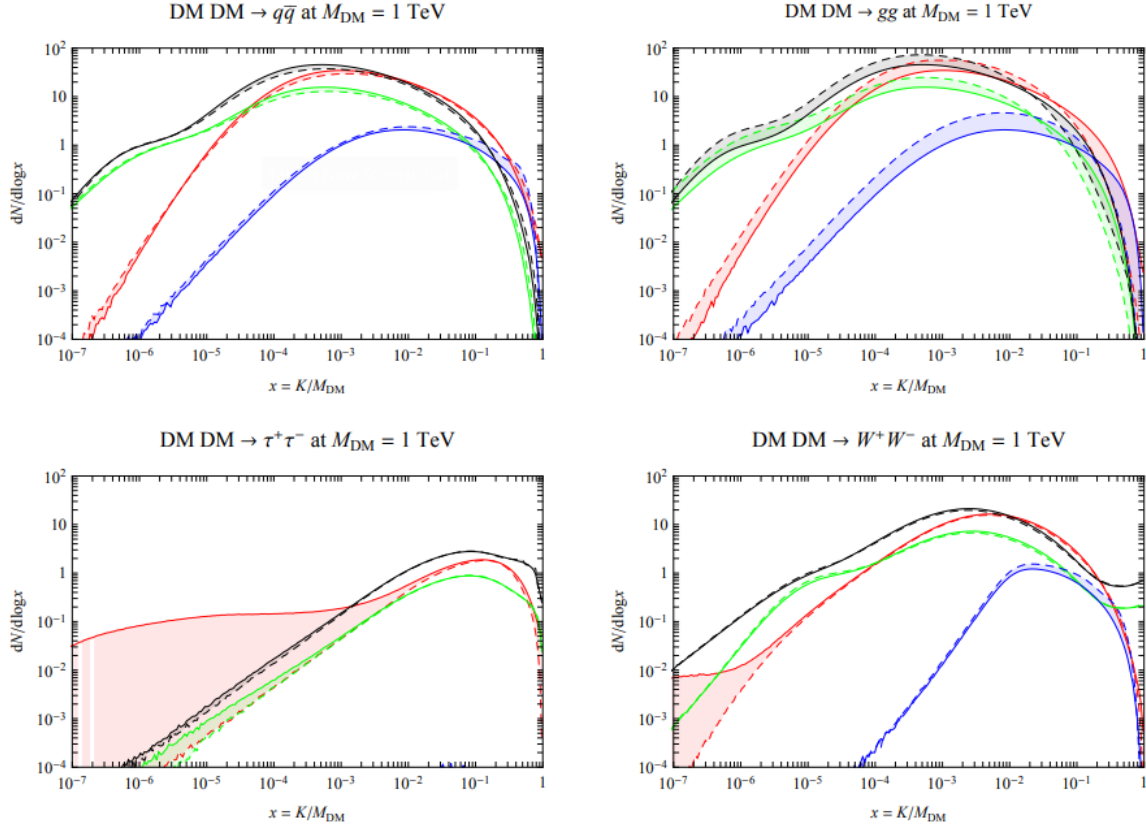


Figure 2.14 Dark Matter annihilation spectra for different final state particle and standard model annihilation channels [24]. Photons (red), e^\pm (green), \bar{p} (blue), ν (black).

625 Exposing our observations to more cosmic messengers greatly increases our sensitivity to
 626 rare processes. In the case of DM, Figure 2.14, there are many SM particles produced in DM
 627 annihilation. Among the final state fluxes are gammas and neutrinos. Charged particles are also
 628 produced however they would not likely make it to Earth since they will be deflected by magnetic
 629 fields between the source and Earth. This means observatories that can see the neutral messengers
 630 are especially good for DM searches and for combining data for a multi-messenger DM search.

CHAPTER 3

631 MULTIMESSENGER ASTROPHYSICS: DETECTING HIGH ENERGY NEUTRAL 632 MESSENGERS

633 3.1 Introduction

634 Before the 20th century, all astrophysics observations were optical in nature. We literally only
635 saw things with highly magnified optical observations. Then we discovered cosmic rays. cosmic
636 rays are charged particles, typically naked protons or H+. This was seen by Victor Hess in 19??.
637 Around the same time we discovered neutrinos from beta decay. Sometime around 1950 we started
638 to build neutrino detectors which were mostly sensitive to neutrinos from the sun. Finally, it was
639 theorized that compact objects like black holes and neutron stars would create waves in space-time
640 when they experience mergers or collisions.

641 In the 21st century, we have developed new observation techniques and detectors that are no only
642 sensitive to these four messengers - photons ([TODO: photon](#)), neutrinos ([TODO: nu](#)), Cosmic
643 Rays (CR), and Gravitational Wave (WV) - we're collect high energy versions of these events.
644 For the standad model particles, we're now sensitive to all messengers above the MeV eneryg
645 range. Additionally, the GW's were sensitive to are in the stellar mass black hole region and above
646 within our galactic neighborhood. This means were becoming sensitive to the fundamental physics
647 occuring within the universe and we can rely on the universe as a TeV+ particle accelerator. We
648 also have the abaility to correlate high energy events across messengers and gain new insights on
649 the processes that occur in our universe.

650 This thesis focuses on very high energy (VHE) gamma rays and neutrinos. These can both be
651 observed through the water cherenkov detection technique altho not exclusively. Methods on how
652 to detect and observe these neutral messengers are discussed Section 3.3 and Section 3.4

653 3.2 Charged Particles in a Medium

654 For high enery gamma-rays and neutrinos, we can exploit the same effect that charged particles
655 have with water. This effect is known as Cherenkov radiation. Cherenkov Radiation occurs when a
656 charged particle, usually electrons (e) or muons (μ), traverse a medium, like water, faster than the

657 speed of light in that medium. This is similar to sonic boom where an object moves through air
658 faster than the speed of sound in air. Cherenkov radiation can therefore be thought of as an 'optic
659 boom'. Many astro-particle physics experiments will use water as the medium as because water
660 has a unique set of properties ideal for charged particle tracking.



Figure 3.1 TODO: Show a nuclear reactor with cherenkov radiation[NEEDS A SOURCE][FACT CHECK THIS]

661 The frequency of light emitted due to cherenkov radiation follows the equation:

$$INSERT\ Cherenkov\ wavelength\ calc\ HERE. \quad (3.1)$$

662 The absorption spectra is shown in the following figure:

663 **3.3 Photons (γ)**

664 **3.4 Neutrinos (ν)**

665 **3.5 Opportunities to Combine for Dark Matter**



Figure 3.2 TODO: absorption spectrum of liquid and solid water[NEEDS A SOURCE][FACT CHECK THIS]

CHAPTER 4

666 **HIGH ALTITUDE WATER CHERENKOV (HAWC) OBSERVATORY**

667 **4.1 The Detector**

668 **4.2 Events Reconstruction and Data Acquisition**

669 **4.2.1 G/H Discrimination**

670 **4.2.2 Angle**

671 **4.2.3 Energy**

672 **4.3 Remote Monitoring**

673 **4.3.1 ATHENA Database**

674 **4.3.2 HOMER**

675

CHAPTER 5

ICECUBE NEUTRINO OBSERVATORY

676 **5.1 The Detector**

677 **5.2 Events Reconstruction and Data Acquisition**

678 **5.2.1 Angle**

679 **5.2.2 Energy**

680 **5.3 Northern Test Site**

681 **5.3.1 PIgeon remote dark rate testing**

682 **5.3.2 Bulkhead Construction**

CHAPTER 6

GLORY DUCK: MULTI-WAVELENGTH SEARCH FOR DARK MATTTER ANNIHILATION TOWARDS DWARF SPHEROIDAL GALAXIES

6.1 Introduction

The field of astrophysics now has several instruments and observatories sensitive to high energy gamma-rays. The energy sensitivity for the modern gamma-ray program spans many orders of magnitude. Figure 6.1 demonstrates these similar sensitivities across energies for the five experiments: Fermi-LAT, HAWC, HESS, MAGIC, and VERITAS.

Each of the five experiments featured in Figure 6.1 have independently searched for DM annihilation from dwarf spheroidal galaxies (dSph) and set limits. Intriguingly, there are regions of substantial overlap in their energy sensitivities. This clearly motivates an analysis that combines data from these five. Each experiment has unique gamma-ray detection methods and their weaknesses and strengths can be leveraged with each other. The HAWC gamma-ray observatory is extensively introduced in chapter 4, so it is not introduced here. A brief description of the remaining experiments are in the following paragraphs.

The Large Area Telescope (LAT) is a pair conversion telescope mounted on the NASA Fermi satellite in orbit \sim 550 km above the Earth [26]. LAT's field of view covers about 20% of the whole sky, and it sweeps the whole sky approximately every 3 hours. LAT's gamma-ray energy sensitivity ranges from 20 MeV up to 1 TeV. Previous DM searches towards dSphs using Fermi-LAT are published in [27] and [28]

The High Energy Spectroscopic System (HESS), Major Atmospheric Gamma Imaging Cherenkov (MAGIC), and Very Energetic Radiation Imaging Telescope Array System (VERITAS) are arrays of Imaging Atmospheric Cherenkov Telescopes (IACT). These telescopes observe the Cherenkov light emitted from gamma-ray showers in the Earth's atmosphere. The field of view for these telescopes is no larger than 5° with energy sensitivities ranging from 30 GeV up to 100 TeV [29, 30, 31]. IACTs are able to make precise observations in selected regions of the sky, however can only be operated in ideal dark conditions. HESS's observations of the dwarves

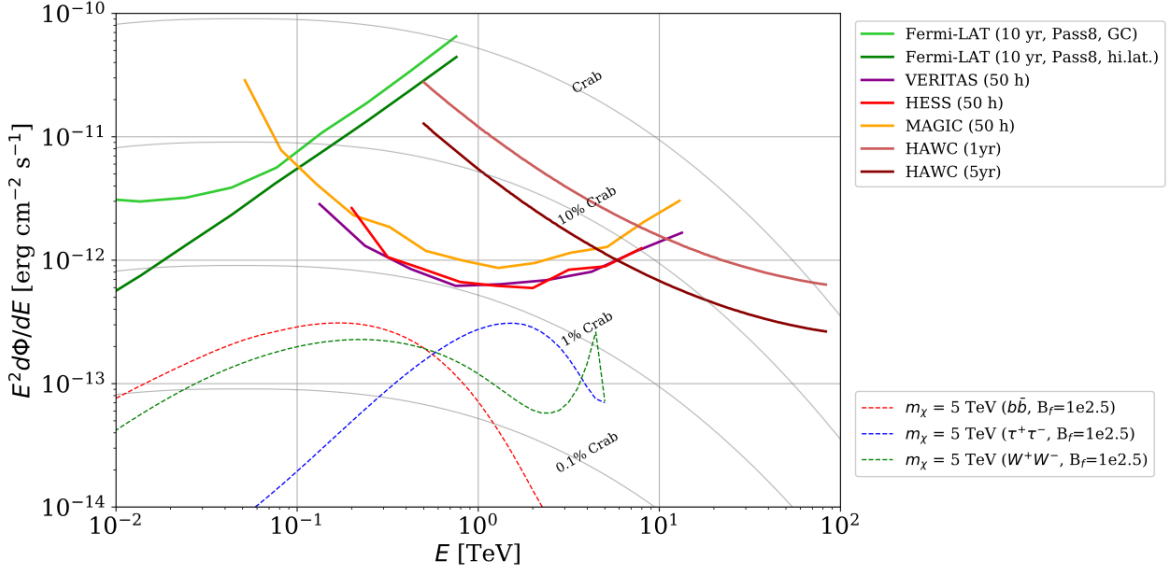


Figure 6.1 Sensitivities of five gamma-ray experiments compared to percentages of the Crab nebula’s emission and dark matter annihilation. Solid lines present estimated sensitivities to power law spectra [FACT CHECK THIS] for each experiment. Green lines are Fermi-LAT sensitivities where lighter green is the sensitivity to the galactic center and dark green is its sensitivity to higher declinations. Orange, red, and purple solid lines represent the MAGIC, HESS, and VERITAS 50 hour sensitivities respectively. The maroon and brown lines are the HAWC 1 year and 5 year sensitivities. Across four decades of gamma-ray energy, these experiments have similar sensitivities on the order 10^{-12} erg $\text{cm}^{-2}\text{s}^{-1}$. The dotted lines are estimated dark matter fluxes assuming $m_\chi = 5$ TeV DM annihilating to bottom quarks (red), tau leptons (blue), and W bosons (green). Faded gray lines outline percentage flux of the Crab nebula. Figure is an augmented version of [25]

709 Sculptor and Carina were between January 2008 and December 2009. HESS’s observations of
 710 Coma Berenices were from 2010 to 2013, and Fornax was observed in 2010 [32, 33, 34]. MAGIC
 711 provided deep observations of Segue1 between 2011 and 2013 [35]. MAGIC also provides data
 712 for three dwarves: Coma Berenices, Draco, and Ursa Major II where observations were made
 713 in: January - June 2019 [36], March - September 2018 [36], and 2014 - 2016 [37] respectively.
 714 VERITAS provided data for Boötes I, Draco, Segue 1, and Ursa Minor from 2009 to 2016 [38].

715 This chapter presents the Glory Duck analysis, the name given for the search for dark matter
 716 annihilation from dSph by combining data from the five gamma-ray observatories: Fermi-LAT,
 717 HAWC, HESS, MAGIC, and VERITAS. Specifically, the methods in analysis and modeling are
 718 presented for the HAWC gamma-ray observatory. This work was published to the Journal of
 719 Cosmology and Astroparticle Physics and presented at the International Cosmic Ray Conference

720 in 2019, 2021, and 2023 [39, 40, 41] and others.

721 **6.2 Dataset and Background**

722 This section enumerates the data and background methods used for HAWC’s study of dSphs.
723 Section 6.2.1 and Section 6.2.2 are most useful for fellow HAWC collaborators looking to replicate
724 the Glory Duck analysis.

725 **6.2.1 Itemized HAWC files**

- 726 • Detector Resolution: `response_aerie_svn_27754_systematics_best_mc_test_no`
727 `broadpulse_10pctlogchargesmearing_0.63qe_25kHzNoise_run5481_curvatu`
728 `re0_index3.root`
- 729 • Data Map: `maps-20180119/liff/maptree_1024.root`
- 730 • Spectral Dictionary: `DM_CirrelliSpectrum_dict_gammas.npy`
- 731 • Analysis wiki: https://private.hawc-observatory.org/wiki/index.php/Glory_Duck_Multi-Experiment_Dark_Matter_Search

733 **6.2.2 Software Tools and Development**

734 This analysis was performed using HAL and 3ML [42, 43] in Python version 2. I built software
735 to implement the *A Poor Particle Physicist Cookbook for Dark Matter Indirect Detection* (PPPC)
736 [44] DM spectral model and dSphs spatial model from [45] for HAWC analysis. A NumPy version
737 of this dictionary was made for both Py2 and Py3. The code base for creating this dictionary is
738 linked on my GitLab sandbox:

- 739 • Py2: [Dictionary Generator \(Deprecated\)](#)
- 740 • Py3: [PPPC2Dict](#)

741 The analysis was performed using the f_{hit} framework performed in the HAWC Crab paper
742 [42]. The Python2 NumPy dictionary file for gamma-ray final states is `dmCirSpecDict.npy`. The
743 corresponding Python3 file is `DM_CirrelliSpectrum_dict_gammas.npy`. These files can also

744 be used for decay channels and the PPPC describes how [44]. All other software used for data
745 analysis, DM profile generation, and job submission to SLURM are also kept in my sandbox for
746 [the Glory Duck](#) project.

747 **6.2.3 Data Set and Background Description**

748 The HAWC data maps used for this analysis contain 1017 days of data between runs 2104
749 (2014-11-26) and 7476 (2017-12-20). They were generated from pass 4.0 reconstruction. The
750 analysis is performed using the f_{hit} energy binning scheme with bins (1-9) similar to what was done
751 for the Crab and previous HAWC dSph analysis [42, 46]. Bin 0 was excluded as it has substantial
752 hadronic contamination and poor angular resolution.

753 This analysis was done on dSphs because of their large DM mass content relative to baryonic
754 mass. We consider the following to estimate the background to this study.

- 755 • The dSphs are small in HAWC’s field of view, so the analysis is not sensitive to large or small
756 scale anisotropies.
- 757 • The dSphs used in this analysis are off the galactic plane.
- 758 • The dSphs are baryonically faint relative to their expected dark matter content and are not
759 expected to contain high energy gamma-ray sources.

760 Therefor we make no additional assumptions on the background from our sources and use
761 HAWC’s standard direct integration method for background estimation [42]. It is possible for
762 gamma rays from DM annihilation to scatter in transit to HAWC via Inverse Compton Scattering
763 (ICS). This was investigated and its impact on the flux is basically zero. Supporting information
764 on this is in Section 6.7.1

765 **6.3 Analysis**

766 The expected differential photon flux from DM-DM annihilation to standard model particles,
767 $d\Phi_\gamma/dE_\gamma$, over solid angle, Ω is described by the familiar equation.

$$\frac{d\Phi_\gamma}{dE_\gamma} = \frac{\langle\sigma v\rangle}{8\pi m_\chi^2} \frac{dN_\gamma}{dE_\gamma} \times \int_{\text{source}} d\Omega \int_{l.o.s} \rho_\chi^2 dl(r, \theta') \quad (6.1)$$

768 Where $\langle \sigma v \rangle$ is the velocity weighted annihilation cross-section. $\frac{dN}{dE}$ is the expected differential
 769 number of photons produced at each energy per annihilation. m_χ is the rest mass of the supposed
 770 DM particle. ρ_χ is the DM density. J is the astrophysical J-factor and is defined as

$$J = \int d\Omega \int_{l.o.s} dl \rho_\chi^2(r, \theta') \quad (6.2)$$

771 l is the distance to the source from Earth. r is the radial distance from the center of the source. θ' is
 772 the half angle defining a cone containing the DM source. How each component is synthesized and
 773 considered for HAWC's analysis is presented in the following sections. Section 6.3.1 presents the
 774 particle physics model for DM annihilation. Section 6.3.2 presents the spatial distributions built
 775 for each dSph.

776 6.3.1 $\frac{dN_\gamma}{dE_\gamma}$ - Particle Physics Component

777 For these spectra, we import the PPPC with Electroweak (EW) corrections [44]. The spectrum
 778 is implemented as a model script in astromodels for 3ML. The EW corrections were previously not
 779 considered for HAWC and are significant for DM annihilating to EW coupled SM particles such
 780 as all leptons, and the γ , Z , and W bosons [46]. Figure 6.2 demonstrates the significance of EW
 781 corrections for W boson annihilation. Across EW SM channels, the gamma-ray spectra become
 782 harder than spectra without EW corrections. Tables from the PPPC were reformatted into Python
 783 NumPy dictionaries for collaboration-wide use. A class in astromodels was developed to include
 784 the EW correction from the PPPC and is aptly named `PPPCSpectra` within `DM_models.py`.

785 6.3.2 J - Astrophysical Component

786 The J-factor profiles for each source are imported from Geringer-Sameth (referred to with \mathcal{GS})
 787 [45]. These were pulled from the publication as $J(\theta)$, where θ is the angular separation from the
 788 center of the source. HAWC requires maps in terms of $\frac{dJ}{d\Omega}$, so the conversion from the maps was
 789 done in the following way...

790 First, convert the angular distances to solid angles

$$\Omega = 2 \cdot \pi(1 - \cos(\theta)) \quad (6.3)$$

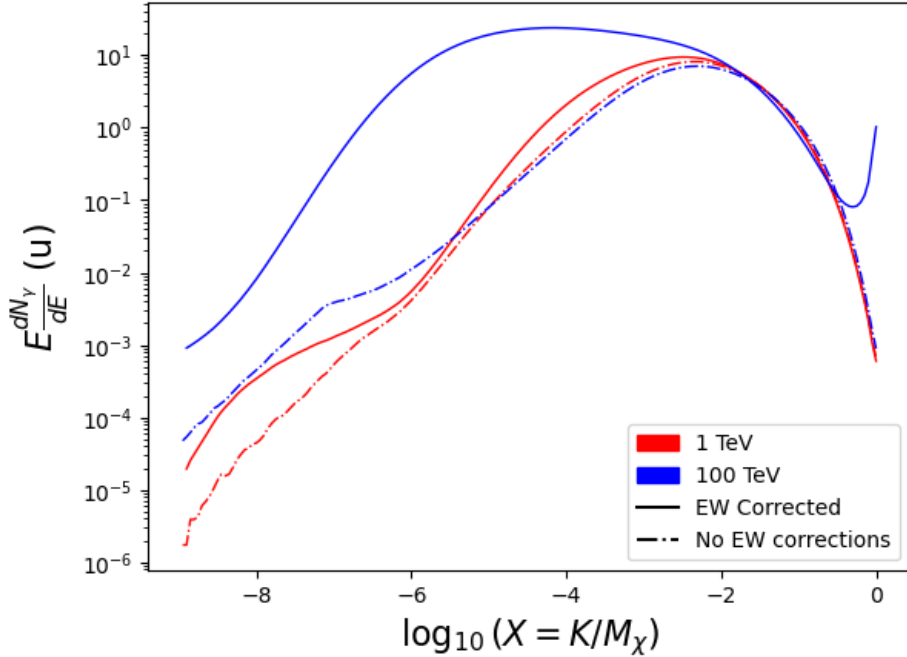


Figure 6.2 Effect of Electroweak (EW) corrections on expected DM annihilation spectrum for $\chi\chi \rightarrow W^-W^+$. Solid lines are spectral models that consider EW corrections. Dash-dot lines are spectral models without EW corrections. Red lines are models for $M_\chi = 1$ TeV. Blue lines represent models for $M_\chi = 100$ TeV. All models are sourced from the PPPC4DMID [44].

791 which reduces with a small angle approximation to $\pi\theta^2$. Next, the central difference for both the
 792 ΔJ and $\Delta\Omega$ value were calculated from the discretized $J(\theta)$ with the central difference stencil:

$$\Delta\phi_i = \phi_{i+1} - \phi_{i-1} \quad (6.4)$$

793 Where ϕ is either Ω or J . These were done separately in case the grid spacing in θ was not uniform.
 794 Finally, these lists are divided so that we are left with an approximation of the $dJ/d\Omega$ profile that
 795 is a function of θ . Admittedly, this is an approximation method for the map which introduces small
 796 errors compared to the true profile estimate. This was checked as a systematic against the author's
 797 profiling of the spatial distribution and is documented in Section 6.8.1.

798 With $\frac{dJ}{d\Omega}(\theta)$, a map is generated, first by filling in the north-east quadrant of the map. This
 799 quadrant is then reflected twice, vertically then horizontally, to fill the full map. Maps are then
 800 normalized by dividing the discrete 2D integral of the map. The 2D integral was a simple height

801 of bins, Newton's integral:

$$p^2 \cdot \sum_{i,j=0}^{N,M} \frac{dJ}{d\Omega}(\theta_{i,j}, \phi_{i,j}) \quad (6.5)$$

802 These maps are HEALpix maps with NSIDE 16384 and saved in the `.fits` format.

803 Another DM spatial distribution model from Bonnivard (\mathcal{B}) [47] was used for the Glory Duck
804 study. However, to save computational time, limits from \mathcal{GS} were scaled to \mathcal{B} instead of each
805 experiment performing a full study a second time. How these models compare is demonstrated
806 for each dSph in Figure 6.16 and Figure 6.17 Plots of these maps are provided for each source
807 in chapter A Examples of the two most impactful dSphs derived from \mathcal{GS} , Segue1 and Coma
808 Berenices are featured in Figure 6.3

809 6.3.3 Source Selection and Annihilation Channels

810 We use many of the dSphs presented in HAWC's previous dSph DM search [46]. HAWC's
811 sources for Glory Duck include Boötes I, Coma Berenices, Canes Venatici I + II, Draco, Hercules,
812 Leo I, II, + IV, Segue 1, Sextans, and Ursa Major I + II. A full description of all sources used
813 in Glory Duck is found in Table 6.1. Triangulum II was excluded from the Glory Duck analysis
814 because of large uncertainties in its J factor. Ursa Minor was excluded from HAWC's contribution
815 to the combination because the source extension model extended Ursa Minor beyond HAWC's field
816 of view. Ursa Minor was not expected to contribute significantly to the combined limit, so work
817 was not invested in a solution to include Ursa Minor.

818 This analysis improves on the previous HAWC dSph paper [46] in the following ways. Pre-
819 viously, the dSphs were treated and implemented as point sources. For this analysis, dSphs are
820 modeled and treated as extended source. The impact of this change with respect to the upper limit
821 is source dependent and is explored in Section 6.7.2. Previously, the particle physics model used for
822 gamma-ray spectra from DM annihilation did not have EW corrections where the PPPC includes
823 them. Finally, the gamma-ray ray dataset is much larger. The study performed here analyzes over
824 1000 days of data compared to 507.

825 The SM annihilation channels probed for the Glory Duck combination include $b\bar{b}$, $e\bar{e}$, $\mu\bar{\mu}$, $\tau\bar{\tau}$,
826 $t\bar{t}$, W^+W^- , and ZZ . A summary of all sources, with a description of each experiments' sensitivity

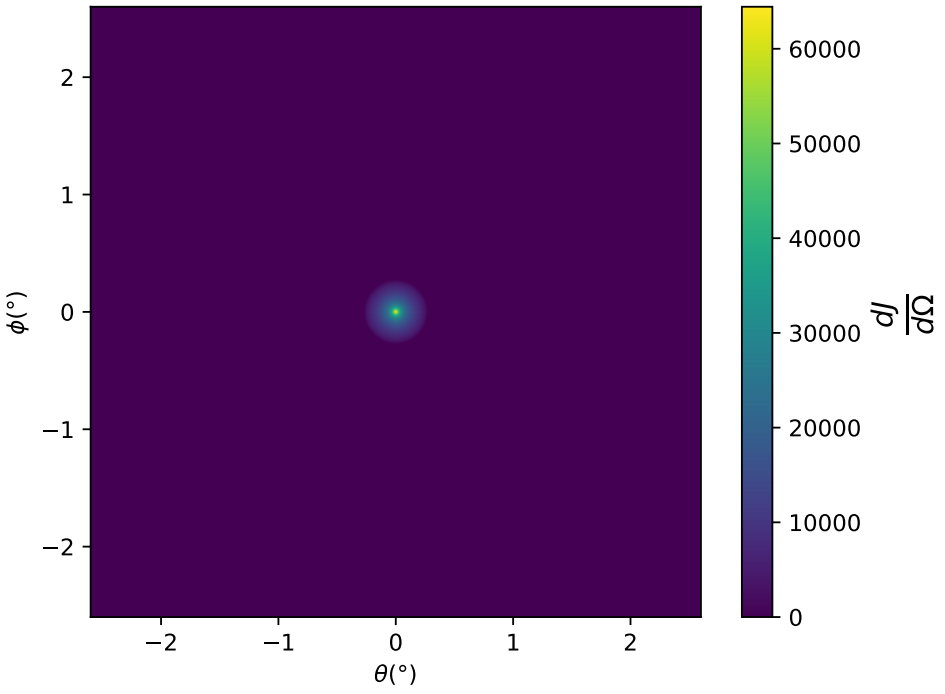
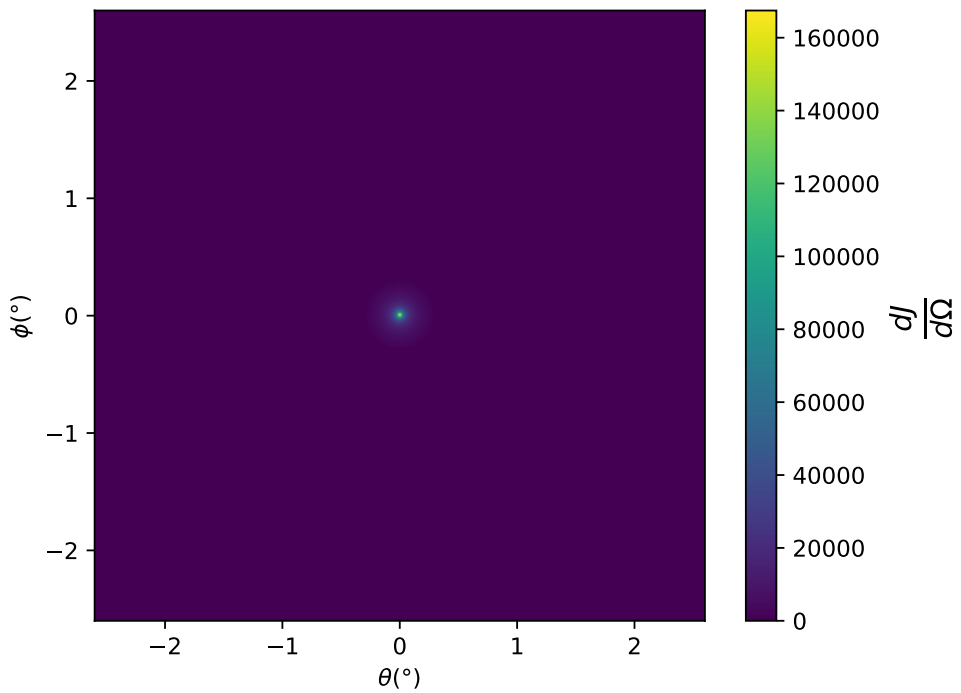


Figure 6.3 $\frac{dJ}{d\Omega}$ maps for Segue1 (top) and Coma Berenices (bottom). Origin is centered on the specific dwarf spheroidal galaxies (dSph). X and Y axes are the angular separation from the center of the dwarf. Plots of the remaining 11 dSph HAWC studied are linked in Fig. A.1.

Table 6.1 Summary of the relevant properties of the dSphs used in the present work. Column 1 lists the dSphs. Columns 2 and 3 present their heliocentric distance and galactic coordinates, respectively. Columns 4 and 5 report the J -factors of each source given from the \mathcal{GS} and \mathcal{B} independent studies and their estimated $\pm 1\sigma$ uncertainties. The values $\log_{10} J$ (\mathcal{GS} set) [45] correspond to the mean J -factor values for a source extension truncated at the outermost observed star. The values $\log_{10} J$ (\mathcal{B} set) [47] are provided for a source extension at the tidal radius of each dSph. **Bolded sources are within HAWC's field of view and provided to the Glory Duck analysis.**

Name	Distance (kpc)	l, b ($^{\circ}$)	$\log_{10} J$ (\mathcal{GS} set) $\log_{10}(\text{GeV}^2 \text{cm}^{-5} \text{sr})$	$\log_{10} J$ (\mathcal{B} set) $\log_{10}(\text{GeV}^2 \text{cm}^{-5} \text{sr})$
Boötes I	66	358.08, 69.62	$18.24^{+0.40}_{-0.37}$	$18.85^{+1.10}_{-0.61}$
Canes Venatici I	218	74.31, 79.82	$17.44^{+0.37}_{-0.28}$	$17.63^{+0.50}_{-0.20}$
Canes Venatici II	160	113.58, 82.70	$17.65^{+0.45}_{-0.43}$	$18.67^{+1.54}_{-0.97}$
Carina	105	260.11, -22.22	$17.92^{+0.19}_{-0.11}$	$18.02^{+0.36}_{-0.15}$
Coma Berenices	44	241.89, 83.61	$19.02^{+0.37}_{-0.41}$	$20.13^{+1.56}_{-1.08}$
Draco	76	86.37, 34.72	$19.05^{+0.22}_{-0.21}$	$19.42^{+0.92}_{-0.47}$
Fornax	147	237.10, -65.65	$17.84^{+0.11}_{-0.06}$	$17.85^{+0.11}_{-0.08}$
Hercules	132	28.73, 36.87	$16.86^{+0.74}_{-0.68}$	$17.70^{+1.08}_{-0.73}$
Leo I	254	225.99, 49.11	$17.84^{+0.20}_{-0.16}$	$17.93^{+0.65}_{-0.25}$
Leo II	233	220.17, 67.23	$17.97^{+0.20}_{-0.18}$	$18.11^{+0.71}_{-0.25}$
Leo IV	154	265.44, 56.51	$16.32^{+1.06}_{-1.70}$	$16.36^{+1.44}_{-1.65}$
Leo V	178	261.86, 58.54	$16.37^{+0.94}_{-0.87}$	$16.30^{+1.33}_{-1.16}$
Leo T	417	214.85, 43.66	$17.11^{+0.44}_{-0.39}$	$17.67^{+1.01}_{-0.56}$
Sculptor	86	287.53, -83.16	$18.57^{+0.07}_{-0.05}$	$18.63^{+0.14}_{-0.08}$
Segue I	23	220.48, 50.43	$19.36^{+0.32}_{-0.35}$	$17.52^{+2.54}_{-2.65}$
Segue II	35	149.43, -38.14	$16.21^{+1.06}_{-0.98}$	$19.50^{+1.82}_{-1.48}$
Sextans	86	243.50, 42.27	$17.92^{+0.35}_{-0.29}$	$18.04^{+0.50}_{-0.28}$
Ursa Major I	97	159.43, 54.41	$17.87^{+0.56}_{-0.33}$	$18.84^{+0.97}_{-0.43}$
Ursa Major II	32	152.46, 37.44	$19.42^{+0.44}_{-0.42}$	$20.60^{+1.46}_{-0.95}$
Ursa Minor	76	104.97, 44.80	$18.95^{+0.26}_{-0.18}$	$19.08^{+0.21}_{-0.13}$

827 to the source, is provided in Table 6.2.

828 6.4 Likelihood Methods

829 6.4.1 HAWC Likelihoods

830 For every analysis bin in energy, f_{hit} bins (1-9), and location, we can expect N signal events and
831 B background events. The expected number of excess signal events from dark matter annihilation,

Table 6.2 Summary of dSph observations by each experiment used in this work. A ‘-’ indicates the experiment did not observe the dSph for this study. For Fermi-LAT, the exposure at 1 GeV is given. For HAWC, $|\Delta\theta|$ is the absolute difference between the source declination and HAWC latitude. HAWC is more sensitive to sources with smaller $|\Delta\theta|$. For IACTs, we show the zenith angle range, the total exposure, the energy range, the angular radius θ of the signal or ON region, the ratio of exposures between the background-control (OFF) and signal (ON) regions (τ), and the significance of gamma-ray excess in standard deviations, σ .

Source name	Fermi-LAT	HAWC	H.E.S.S, MAGIC, VERITAS						
	Exposure (10^{11} s m 2)	$ \Delta\theta $ ($^\circ$)	IACT	Zenith ($^\circ$)	Exposure (h)	Energy range (GeV)	θ ($^\circ$)	τ	S (σ)
Boötes I	2.6	4.5	VERITAS	15 – 30	14.0	100–41000	0.10	8.6	-1.0
Canes Venatici I	2.9	14.6	–	–	–	–	–	–	–
Canes Venatici II	2.9	15.3	–	–	–	–	–	–	–
Carina	3.1	–	H.E.S.S.	27 – 46	23.7	310 – 70000	0.10	18.0	-0.3
Coma Berenices	2.7	4.9	H.E.S.S.	47 – 49	11.4	550 – 70000	0.10	14.4	-0.4
Draco	3.8	38.1	MAGIC	5 – 37	49.5	60 – 10000	0.17	1.0	–
			MAGIC	29 – 45	52.1	70 – 10000	0.22	1.0	–
			VERITAS	25 – 40	49.8	120 – 70000	0.10	9.0	-1.0
Fornax	2.7	–	H.E.S.S.	11 – 25	6.8	230 – 70000	0.10	45.5	-1.5
Hercules	2.8	6.3	–	–	–	–	–	–	–
Leo I	2.5	6.7	–	–	–	–	–	–	–
Leo II	2.6	3.1	–	–	–	–	–	–	–
Leo IV	2.4	19.5	–	–	–	–	–	–	–
Leo V	2.4	–	–	–	–	–	–	–	–
Leo T	2.6	–	–	–	–	–	–	–	–
Sculptor	2.7	–	H.E.S.S.	10 – 46	11.8	200 – 70000	0.10	19.8	-2.2
Segue I	2.5	2.9	MAGIC	13 – 37	158.0	60 – 10000	0.12	1.0	-0.5
			VERITAS	15 – 35	92.0	80 – 50000	0.10	7.6	0.7
Segue II	2.7	–	–	–	–	–	–	–	–
Sextans	2.4	20.6	–	–	–	–	–	–	–
Ursa Major I	3.4	32.9	–	–	–	–	–	–	–
Ursa Major II	4.0	44.1	MAGIC	35 – 45	94.8	120 – 10000	0.30	1.0	-2.1
Ursa Minor	4.1	–	VERITAS	35 – 45	60.4	160 – 93000	0.10	8.4	-0.1

832 S , is estimated by convolving Equation (6.1) with HAWC's energy response and pixel point spread
 833 functions. I then compute the test statistic (TS) with the log-likelihood ratio test,

$$\text{TS} = -2 \ln \left(\frac{\mathcal{L}_0}{\mathcal{L}^{\max}} \right) \quad (6.6)$$

835 where \mathcal{L}_0 is the null hypothesis, or no DM emission, likelihood. \mathcal{L}^{\max} is the best fit signal
 836 hypothesis where $\langle \sigma v \rangle$ maximizes the likelihood. We calculate the likelihood of each source and
 837 model, assuming events are Poisson distributed, with

$$\mathcal{L} = \prod_i \frac{(B_i + S_i)^{N_i} e^{-(B_i + S_i)}}{N_i!} \quad (6.7)$$

838 where S_i is the sum of expected number of signal counts. B_i is the number of background counts
 839 observed. N_i is the total number of counts.

840 I also calculate an upper limit on $\langle \sigma v \rangle$ by calculating the 95% confidence level (CL). For the
 841 CL, we define a parameter, TS_{95} , as

$$\text{TS}_{95} \equiv \sum_{\text{bins}} \left[2N \ln \left(1 + \frac{\epsilon S_{\text{ref}}}{B} \right) - 2\epsilon S_{\text{ref}} \right] \quad (6.8)$$

842 where the expected signal counts from a dSph is scaled by ϵ . S_{ref} is the expected number of excess
 843 counts in a bin from DM emission from a dSph with a corresponding annihilation cross-section,
 844 $\langle \sigma v \rangle$. We scan ϵ such that

$$2.71 = \text{TS}_{\max} - \text{TS}_{95} \quad (6.9)$$

845 6.4.2 Glory Duck Joint Likelihood

846 The joint likelihood for the 5-experiment combination was done similarly as Section 6.4.1. We
 847 calculate upper limits on $\langle \sigma v \rangle$ from the TS, Eq. (6.6), and define the likelihood ratio more generally

$$\lambda(\langle \sigma v \rangle | \mathcal{D}_{\text{dSphs}}) = \frac{\mathcal{L}(\langle \sigma v \rangle; \hat{\nu} | \mathcal{D}_{\text{dSphs}})}{\mathcal{L}(\widehat{\langle \sigma v \rangle}; \hat{\nu} | \mathcal{D}_{\text{dSphs}})} \quad (6.10)$$

848 $\mathcal{D}_{\text{dSphs}}$ is the totality of observations across experiments and dSphs. ν are the nuisance parameters
 849 which are the J factors in this study. $\widehat{\langle \sigma v \rangle}$ and $\hat{\nu}$ are the respective estimate that maximize \mathcal{L}
 850 globally. Finally, $\hat{\nu}$ is the set of nuisance parameters that maximize \mathcal{L} for a fixed value of $\langle \sigma v \rangle$.

851 The *complete* joint likelihood, \mathcal{L} that encompasses all observations from all instruments and
 852 dSphs can be factorized into *partial* functions for each dSph l (with $\mathcal{L}_{\text{dSph},l}$) and its J factor (\mathcal{J}_l):

$$\mathcal{L} (\langle \sigma v \rangle; \nu | \mathcal{D}_{\text{dSphs}}) = \prod_{l=1}^{N_{\text{dSphs}}} \mathcal{L}_{\text{dSph},l} (\langle \sigma v \rangle; J_l, \nu_l | \mathcal{D}_l) \times \mathcal{J}_l (J_l | J_{l,\text{obs}}, \sigma_{\log J_l}). \quad (6.11)$$

853 For this study, $N_{\text{dSphs}} = 20$ is the number of dSphs studied. \mathcal{D}_l are the gamma-ray observations
 854 of dSph, l . ν_l are the nuisance parameters modifying the gamma-ray observations of dSph, l ,
 855 but excludes \mathcal{J}_l . \mathcal{J}_l is the J factor for dSph, l , as defined in Equation (6.2), and it is a nuisance
 856 parameter whose value is unknown. $\log_{10} J_{l,\text{obs}}$ and $\sigma_{\log J_l}$ are obtained from fitting a log-normal
 857 function of $J_{l,\text{obs}}$ to the posterior distribution of J_l [48]. $\log_{10} J_{l,\text{obs}}$ and $\sigma_{\log J_l}$ values are provided
 858 in Table 6.1. The term \mathcal{J}_l constraining J_l is written as:

$$\mathcal{J}_l (J_l | J_{l,\text{obs}}, \sigma_{\log J_l}) = \frac{1}{\ln(10) J_{l,\text{obs}} \sqrt{2\pi} \sigma_{\log J_l}} \exp\left(-\frac{(\log_{10} J_l - \log_{10} J_{l,\text{obs}})^2}{2\sigma_{\log J_l}^2}\right). \quad (6.12)$$

859 Both the \mathcal{GS} and \mathcal{B} , displayed in Table 6.1, sets of J factors are used in this analysis. Equation (6.12)
 860 is also normalized, so it can also be interpreted as a probability density function (PDF) for $J_{l,\text{obs}}$.
 861 From Equation (6.1), we can also see that $\langle \sigma v \rangle$ and J_l are degenerate when computing $\mathcal{L}_{\text{dSph},l}$.
 862 Therefore, as noted in [49], it is sufficient to compute $\mathcal{L}_{\text{dSph},l}$ versus $\langle \sigma v \rangle$ for a fixed value of J_l .
 863 We used $J_{l,\text{obs}}(\mathcal{GS})$ reported in Tab. 6.1, in order to perform the profile of \mathcal{L} with respect to J_l .
 864 The degeneracy implies that for any $J'_l \neq J_{l,\text{obs}}$ (in practice in our case we used $J'_l = J_{l,\text{obs}}(\mathcal{B})$ to
 865 compute results from a different set of J factors):

$$\mathcal{L}_{\text{dSph},l} (\langle \sigma v \rangle; J'_l, \nu_l | \mathcal{D}_l) = \mathcal{L}_{\text{dSph},l} \left(\frac{J'_l}{J_{l,\text{obs}}} \langle \sigma v \rangle; J_{l,\text{obs}}, \nu_l | \mathcal{D}_l \right), \quad (6.13)$$

866 which is a straightforward rescaling operation that reduces the computational needs of the profiling
 867 operation since:

$$\mathcal{L} (\langle \sigma v \rangle; \hat{\nu} | \mathcal{D}_{\text{dSphs}}) = \prod_{l=1}^{N_{\text{dSphs}}} \max_{J_l} \left[\mathcal{L}_{\text{dSph},l} (\langle \sigma v \rangle; J_l, \hat{\nu}_l | \mathcal{D}_l) \times \mathcal{J}_l (J_l | J_{l,\text{obs}}, \sigma_{\log J_l}) \right]. \quad (6.14)$$

868 In addition, Eq. (6.13) enables the combination of data from different gamma-ray instruments and
 869 observed dSphs via tabulated values of $\mathcal{L}_{\text{dSph},l}$, or equivalently of λ from Eq. (6.10) as was done in

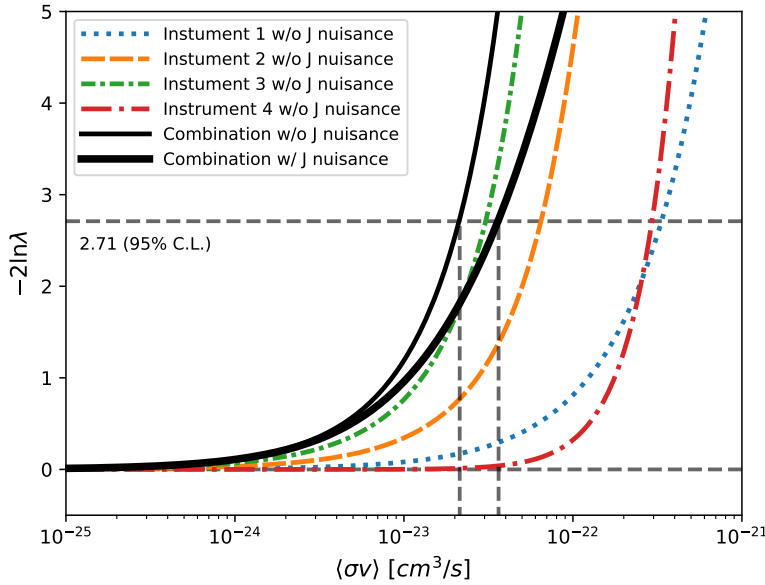


Figure 6.4 Illustration of the combination technique showing a comparison between $-2 \ln \lambda$ provided by four instruments (colored lines) from the observation of the same dSph without any J nuisance and their sum, *i.e.* the resulting combined likelihood (thin black line). According to the test statistics of Equation (6.6), the intersection of the likelihood profiles with the line $-2 \ln \lambda = 2.71$ indicates the 95% C.L. upper limit on $\langle \sigma v \rangle$. The combined likelihood (thin black line) shows a smaller value of upper limit on $\langle \sigma v \rangle$ than those derived by individual instruments. We also show how the uncertainties on the J factor effects the combined likelihood and degrade the upper limit on $\langle \sigma v \rangle$ (thick black line). All likelihood profiles are normalized so that the global minimum $\widehat{\langle \sigma v \rangle}$ is 0. We note that each profile depends on the observational conditions in which a target object was observed. The sensitivity of a given instrument can be degraded and the upper limits less constraining if the observations are performed in non-optimal conditions such as a high zenith angle or a short exposure time.

870 this work, versus $\langle \sigma v \rangle$. $\mathcal{L}_{\text{dSph},l}$ is computed for a fixed value of J_l and profiled with respect to all
 871 instrumental nuisance parameters ν_l , these nuisance parameters are discussed in more detail below.
 872 These values are produced by each detector independently and therefore there is no need to share
 873 sensitive low-level information used to produce them, such as event lists. Figure 6.4 illustrates the
 874 multi-instrument combination technique used in this study with a comparison of the upper limit
 875 on $\langle \sigma v \rangle$ obtained from the combination of the observations of four experiments towards one dSph
 876 versus the upper limit from individual instruments. It also shows graphically the effect of the
 877 J -factor uncertainty on the combined observations.

878 The *partial* joint likelihood function for gamma-ray observations of each dSph ($\mathcal{L}_{\text{dSph},l}$) is

written as the product of the likelihood terms describing the $N_{\text{exp},l}$ observations performed with any of our observatories:

$$\mathcal{L}_{\text{dSph},l} (\langle \sigma v \rangle; J_l, \nu_l | \mathcal{D}_l) = \prod_{k=1}^{N_{\text{exp},l}} \mathcal{L}_{lk} (\langle \sigma v \rangle; J_l, \nu_{lk} | \mathcal{D}_{lk}), \quad (6.15)$$

where each \mathcal{L}_{lk} term refers to an observation of the l -th dSph with associated k -th instrument responses. $N_{\text{exp},l}$ varies from dSph to dSph and can be inferred from Table 6.2.

Each collaboration separately analyzes their data for \mathcal{D}_{lk} corresponding to dSph l and gamma-ray detector k , using as many common assumptions as possible in the analysis. HAWC’s treatment was described earlier in Section 6.4.1 whereas the specifics of the remaining experiments is left to the publication. We compute the values for the likelihood functions \mathcal{L}_{lk} (see Eq. (6.15)) for a fixed value of J_l and profile over the rest of the nuisance parameters ν_{lk} . Then, values of λ from Eq. (6.10) are computed as a function of $\langle \sigma v \rangle$, and shared using a common format. Results are computed for seven annihilation channels, W^+W^- , ZZ , $b\bar{b}$, $t\bar{t}$, e^+e^- , $\mu^+\mu^-$, and $\tau^+\tau^-$ over 62 m_χ values between 5 GeV and 100 TeV provided in [44]. The $\langle \sigma v \rangle$ range is defined between 10^{-28} and $10^{-18} \text{cm}^3 \cdot \text{s}^{-1}$, with 1001 logarithmically spaced values. The likelihood combination, i.e. Equation (6.11), and profile over the J -factor to compute the profile likelihood ratio λ , Equation (6.10), are carried out with two different public analysis software packages, namely `gLike` [50] and `LklCom` [51], that provide the same results [52].

As mentioned previously, each experiment computes the \mathcal{L}_{lk} from Equation (6.10) differently. The remainder of this section highlights the differences in this calculation across the experiments. Four experiments, namely *Fermi*-LAT, H.E.S.S., HAWC and MAGIC, use a binned likelihood to compute the \mathcal{L}_{lk} . For these experiments, for each observation \mathcal{D}_{lk} of a given dSph l carried out using a given gamma-ray detector k , the binned likelihood function is:

$$\mathcal{L}_{lk} (\langle \sigma v \rangle; J_l, \nu_{lk} | \mathcal{D}_{lk}) = \prod_{i=1}^{N_E} \prod_{j=1}^{N_P} \left[\mathcal{P}(s_{lk,ij}(\langle \sigma v \rangle, J_l, \nu_{lk}) + b_{lk,ij}(\nu_{lk}) | N_{lk,ij}) \right] \times \mathcal{L}_{lk,\nu} (\nu_{lk} | \mathcal{D}_{\nu_{lk}}) \quad (6.16)$$

where N_E and N_P are the number of considered bins in reconstructed energy and arrival direction, respectively; \mathcal{P} represents a Poisson PDF for the number of gamma-ray candidate events $N_{lk,ij}$

902 observed in the i -th bin in energy and j -th bin in arrival direction, when the expected number is
 903 the sum of the expected mean number of signal events s_{ij} (produced by DM annihilation) and of
 904 background events b_{ij} ; $\mathcal{L}_{lk,\nu}$ is the likelihood term for the extra ν_{lk} nuisance parameters that vary
 905 from one instrument k to another. The expected counts for signal events s_{ij} for a given dSph l and
 906 detector k is given by:

$$s_{ij}(\langle\sigma\nu\rangle, J) = \int_{E'_{\min,i}}^{E'_{\max,i}} dE' \int_{P'_{\min,j}}^{P'_{\max,j}} d\Omega' \int_0^\infty dE \int_{\Delta\Omega_{tot}} d\Omega \int_0^{T_{\text{obs}}} dt \frac{d^2\Phi(\langle\sigma\nu\rangle, J)}{dEd\Omega} \text{IRF}(E', P' | E, P, t) \quad (6.17)$$

907 where E' and E are the reconstructed and true energies, P' and P the reconstructed and true
 908 arrival directions; $E'_{\min,i}$, $P'_{\min,j}$, $E'_{\max,i}$, and $P'_{\max,j}$ are their lower and upper limits of the i -th
 909 energy bin and the j -th arrival direction bin; T_{obs} is the (dead-time corrected) total observation
 910 time; t is the time along the observations; $d^2\Phi/dEd\Omega$ is the DM flux in the source region (see
 911 Equation (6.1)); and $\text{IRF}(E', P' | E, P, t)$ is the IRF, which can be factorized as the product of the
 912 effective collection area of the detector $A_{\text{eff}}(E, P, t)$, the PDFs for the energy estimator $f_E(E' | E, t)$,
 913 and arrival direction $f_P(P' | E, P, t)$ estimators. Note that for Fermi-LAT, HAWC, MAGIC, and
 914 VERITAS the effect of the finite angular resolution is taken into account through the convolution
 915 of $d\Phi/dEd\Omega$ with f_P in Equation (6.17), whereas in the cases of H.E.S.S. f_P is approximated by a
 916 delta function. This approximation has been made in order to maintain compatibility of the result
 917 with what has been previously published. The difference introduced by this approximation is $< 5\%$
 918 for all considered dSphs. A more comprehensive review of the differences between the analyses of
 919 different instruments can be found in [25].

920 6.5 HAWC Results

921 13 of the 20 dSphs considered for the Glory Duck analysis are within HAWC's field of view.
 922 These dSph are analyzed for emission from DM annihilation according to the likelihood method
 923 described in Section 6.4. The 13 likelihood profiles are then stacked to synthesize a combined
 924 limit on the dark matter cross-section, $\langle\sigma\nu\rangle$. This combination is done for the 7 SM annihilation
 925 channels used in the Glory Duck analysis. Figure 6.5 shows the combined limit for all annihilation
 926 channels with HAWC only observations. We also perform 300 studies of Poisson trials on the

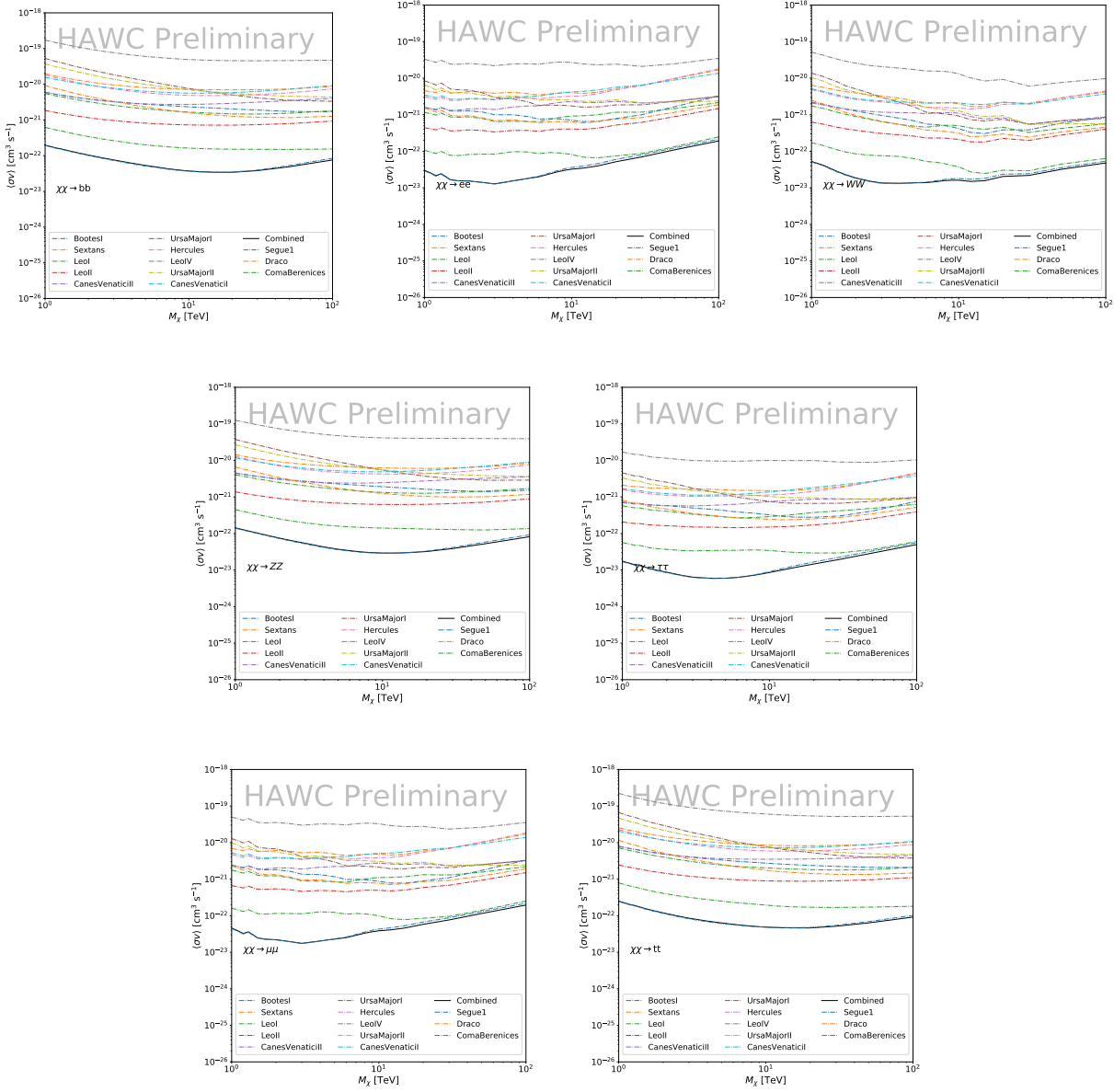


Figure 6.5 HAWC upper limits at 95% confidence level on $\langle\sigma v\rangle$ versus DM mass for seven annihilation channels, using the set of J -factors from Ref. [53]. The solid line represents the observed combined limit. Dashed lines represent limits from individual dSphs.

background. These trials are used to produce HAWC Brazil bands which were shared with the other collaborators for combined Brazil Bands. The results on fitting to HAWC's Poisson trials of the DM hypothesis is shown in Figure 6.7 for all the DM annihilation channels studied for Glory Duck.

No DM was found in HAWC observations. HAWC's limits are dominated by the dSphs Segue1

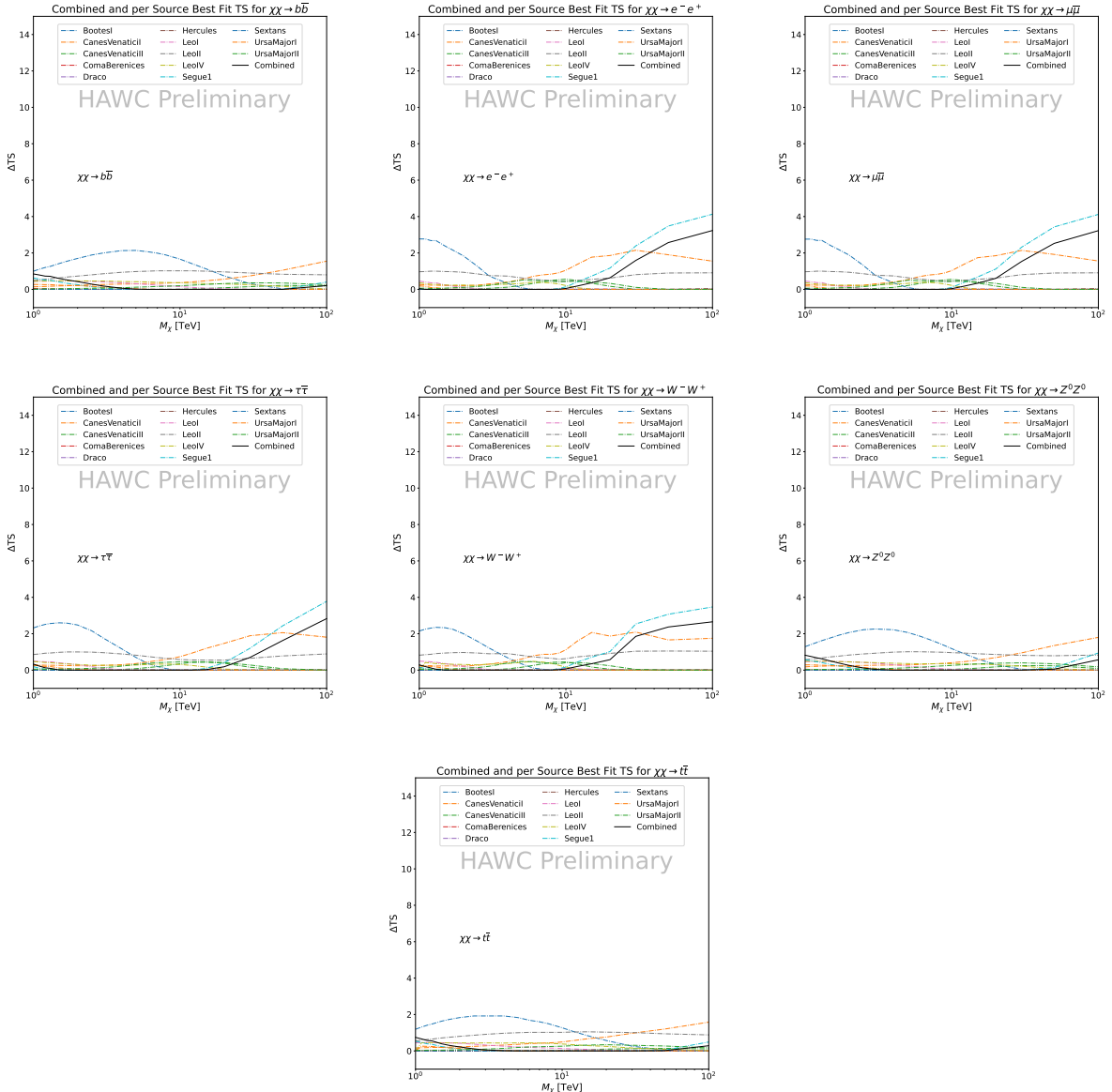


Figure 6.6 HAWC TS values for best fit $\langle \sigma v \rangle$ versus m_χ for seven SM annihilation channels with J factors from \mathcal{GS} . The solid black line shows the combined best fit TS values. The colored, dashed lines are the TS values for each of the 13 sources HAWC studied.

and Coma Berenices. The remaining 11 dSphs do not contribute significantly to the limit because they are at high zenith and/or have much smaller J factors. Even though some remaining dSphs have large J factors, they are towards the edge of HAWC's field of view where HAWC analysis is less sensitive.

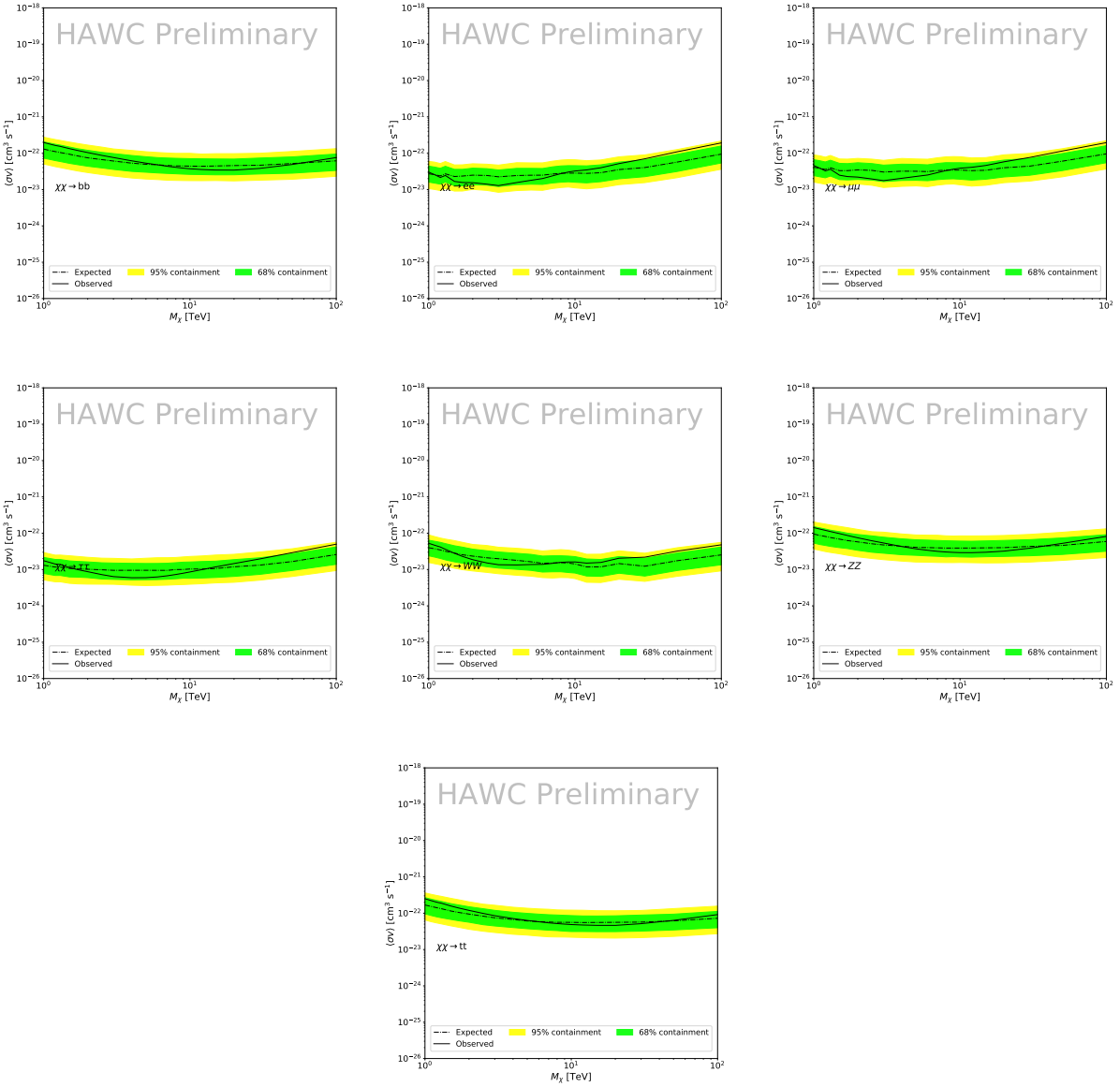


Figure 6.7 HAWC Brazil bands at 95% confidence level on $\langle\sigma v\rangle$ versus DM mass for seven annihilation channels with J -factors from \mathcal{GS} [53]. The solid line represents the combined limit from 13 dSphs. The dashed line is the expected limit. The green band is the 68% containment. The yellow band is the 95% containment.

936 6.6 Glory Duck Combined Results

937 The crux of this analysis is that HAWC's results are combined with 4 other gamma-ray observa-
 938 tories: Fermi-LAT, H.E.S.S., MAGIC, and VERITAS. No significant DM emission was observed
 939 by any of the five instruments. We present the upper limits on $\langle\sigma v\rangle$ assuming seven independent
 940 DM self annihilation channels, namely W^+W^- , Z^+Z^- , $b\bar{b}$, $t\bar{t}$, e^+e^- , $\mu^+\mu^-$, and $\tau^+\tau^-$. The 68%

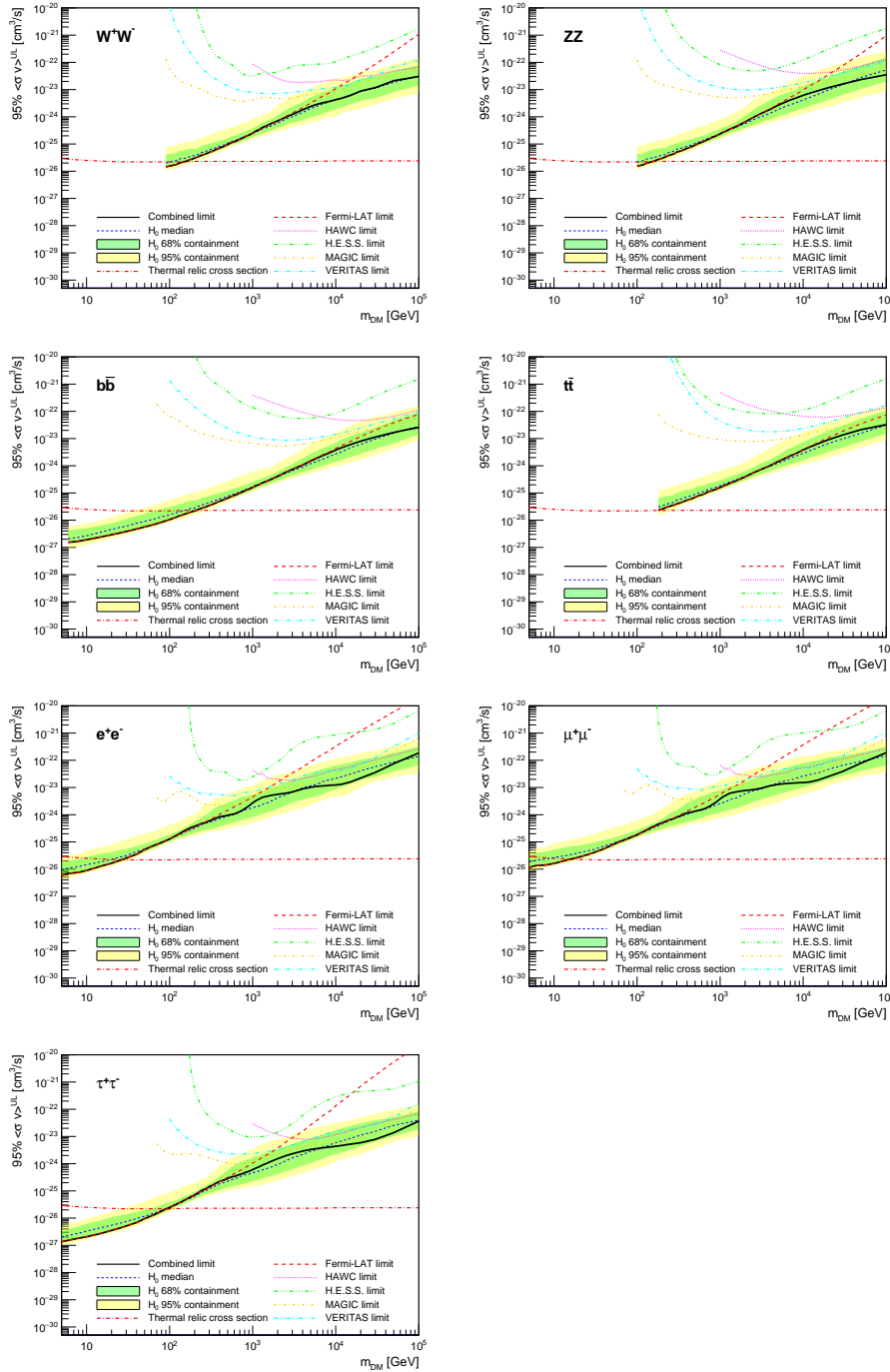


Figure 6.8 Upper limits at 95% confidence level on $\langle\sigma v\rangle$ in function of the DM mass for eight annihilation channels, using the set of J factors from Ref. [53] (\mathcal{GS} set in Table 6.1). The black solid line represents the observed combined limit, the black dashed line is the median of the null hypothesis corresponding to the expected limit, while the green and yellow bands show the 68% and 95% containment bands. Combined upper limits for each individual detector are also indicated as solid, colored lines. The value of the thermal relic cross-section in function of the DM mass is given as the red dotted-dashed line [54].

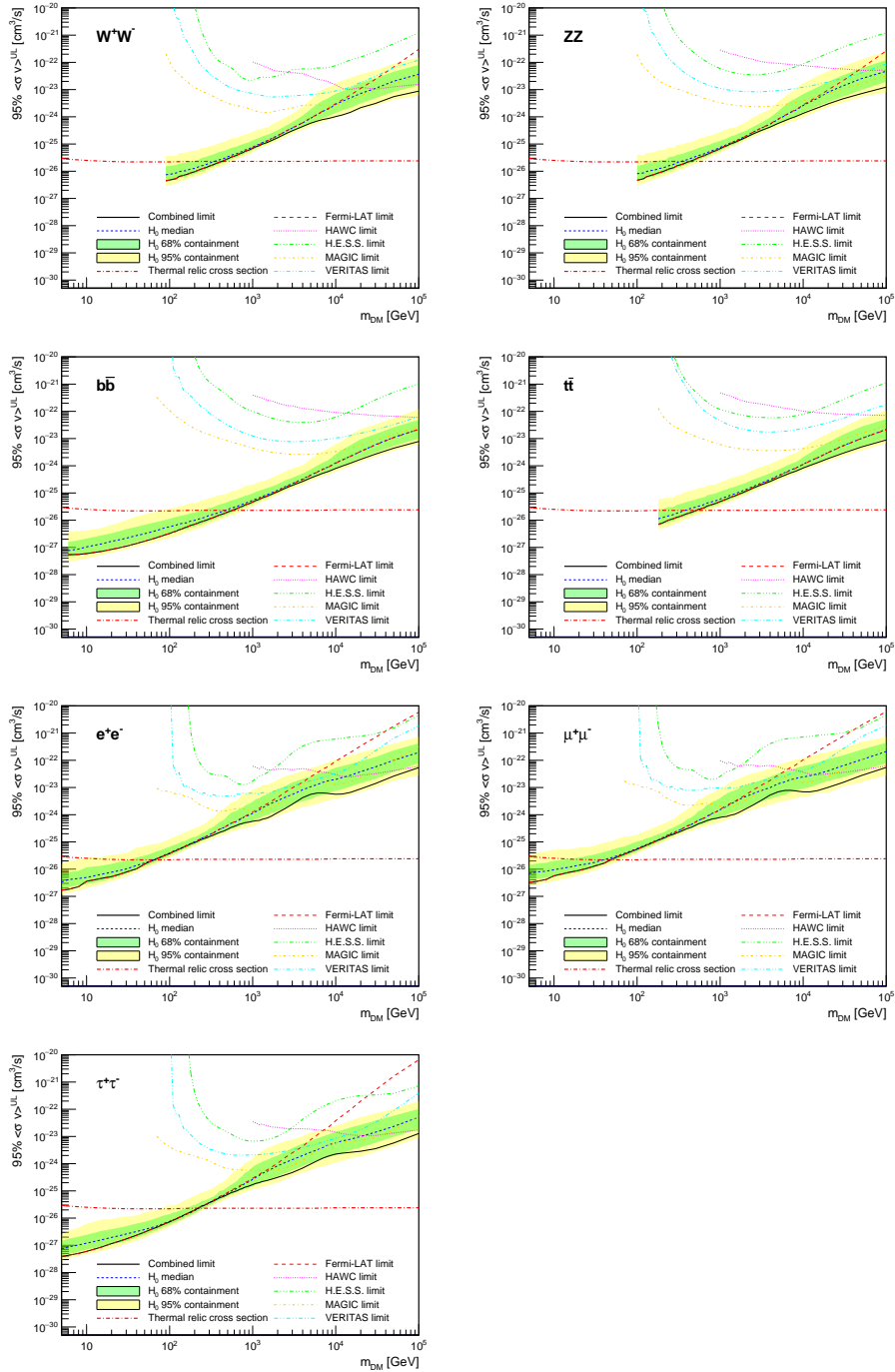


Figure 6.9 Same as Fig. 6.8, using the set of J factors from Ref. [47, 55] (\mathcal{B} set in Table 6.1).

and 95% containment bands are produced from 300 Poisson realizations of the null hypothesis corresponding to each of the combined datasets. These 300 realizations are combined identically to dSph observations. The containment bands and the median are extracted from the distribution of resulting limits on the null hypothesis. These 300 realizations are obtained either by fast simu-

945 lations of the OFF observations, for H.E.S.S., MAGIC, VERITAS, and HAWC, or taken from real
946 observations of empty fields of view in the case of Fermi-LAT [48, 56, 57].

947 The obtained limits are shown in Figure 6.8 for the $\mathcal{G}\mathcal{S}$ set of J -factors [53] and in Figure 6.9
948 for the \mathcal{B} set of J -factors [47, 55]. The combined limits are presented with their 68% and 95%
949 containment bands, and are expected to be close to the median limit when no signal is present.
950 We observe agreement with the null hypothesis for all channels, within 2σ standard deviations,
951 between the observed limits and the expectations given by the median limits. Limits obtained from
952 each detector are also indicated in the figures, where limits for all dSphs observed by the specific
953 instrument have been combined.

954 Below ~ 300 GeV, the *Fermi*-LAT dominates the DM limits for all annihilation channels. From
955 ~ 300 GeV to ~ 2 TeV, *Fermi*-LAT continues to dominate for the hadronic and bosonic DM channels,
956 yet the IACTs (H.E.S.S., MAGIC, and VERITAS) and *Fermi*-LAT all contribute to the limit for
957 leptonic DM channels. For DM masses between ~ 2 TeV to ~ 10 TeV, the IACTs dominate leptonic
958 DM annihilation channels, whereas both the *Fermi*-LAT and the IACTs dominate bosonic and
959 hadronic DM annihilation channels. From ~ 10 TeV to ~ 100 TeV, both the IACTs and HAWC
960 contribute significantly to the leptonic DM limit. For hadronic and bosonic DM, the IACTs and
961 *Fermi*-LAT both contribute strongly.

962 We notice that the limits computed using the \mathcal{B} set of J -factor are always better compared to the
963 ones calculated with the $\mathcal{G}\mathcal{S}$ set. For the W^+W^- , Z^+Z^- , $b\bar{b}$, and $t\bar{t}$ channels, the ratio between the
964 limits computed with the two sets of J -factor is varying between a factor of ~ 3 and ~ 5 depending
965 on the energy, with the largest ratio around 10 TeV. For the channels e^+e^- , $\mu^+\mu^-$, and $\tau^+\tau^-$, the
966 ratio lies between ~ 2 to ~ 6 , being maximum around 1 TeV. Examining Figure 6.16 and Figure 6.17
967 in Section 6.8, these differences are explained by the fact that the \mathcal{B} set provides higher J -factors
968 for the majority of the studied dSphs, with the notable exception of Segue I. The variation on the
969 ratio of the limits for the two sets is due to different dSph dominating the limits depending on the
970 energy. This pushes the range of thermal cross-section which can be excluded to higher mass. This
971 comparison demonstrates the magnitude of systematic uncertainties associated with the choice of

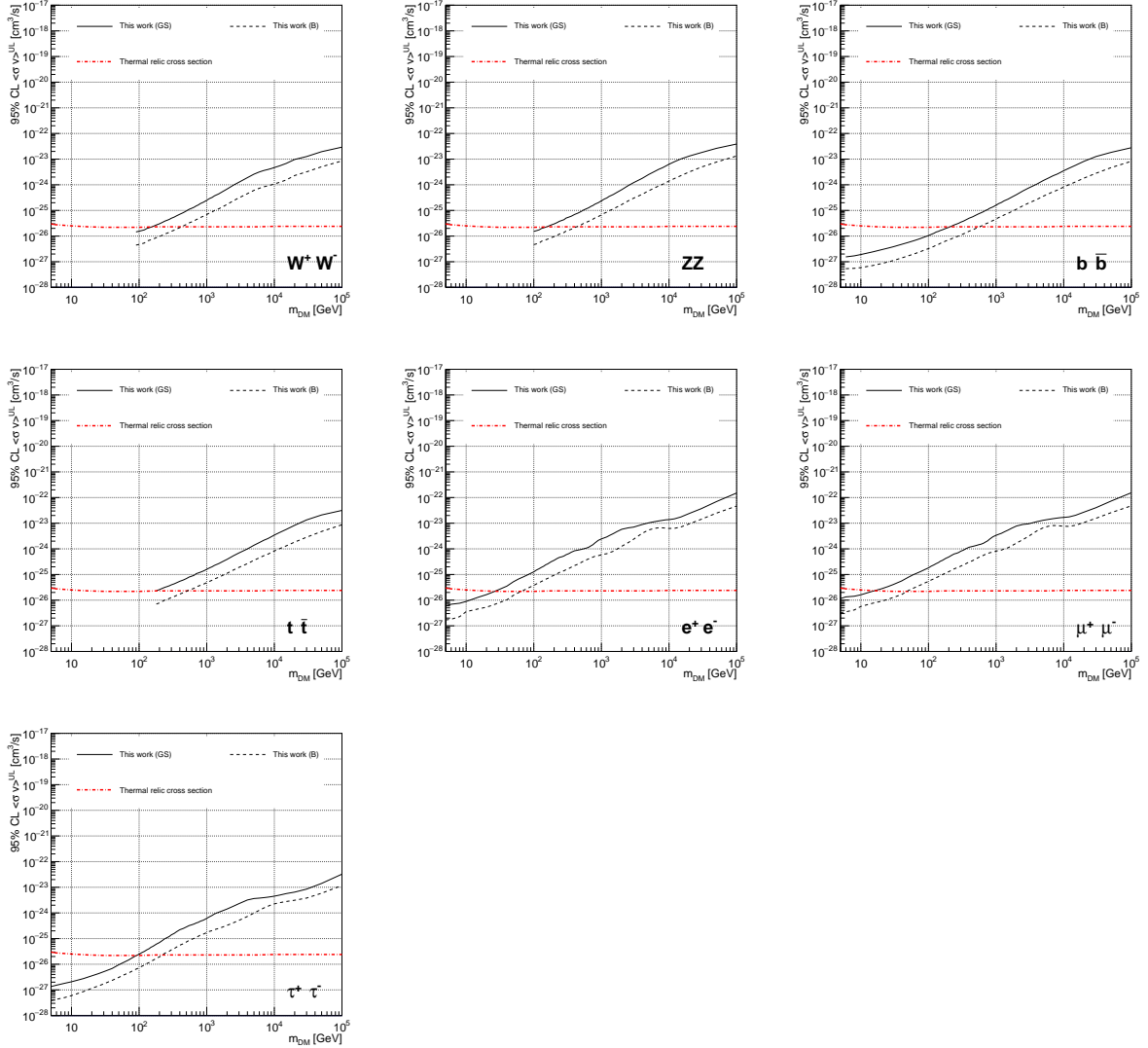


Figure 6.10 Comparisons of the combined limits at 95% confidence level for each of the eight annihilation channels when using the J factors from Ref. [53] (\mathcal{GS} set in Table 6.1), plain lines, and the J factor from Ref. [47, 55] (\mathcal{B} set in Table 6.1), dashed lines. The cross-section given by the thermal relic is also indicated [54].

972 the J -factor

973 This comparison demonstrates the magnitude of systematic uncertainties associated with the
 974 choice of the J -factor calculation. The \mathcal{GS} and \mathcal{B} sets present a difference in the limits for all
 975 channels of about This difference is explained, see Figure 6.16 and Figure 6.17 in Appendix, by the
 976 fact that the \mathcal{B} set provides higher J factors for all dSph except for Segue I. This pushes the range
 977 of thermal cross-section which can be excluded to higher mass.

978 **6.7 HAWC Systematics**

979 **6.7.1 Inverse Compton Scattering**

980 The DM-DM annihilation channels produce many high energy electrons regardless of the
981 primary annihilation channel. These high energy electrons can produce high energy gamma-rays
982 through Inverse Compton Scattering (ICS). If this effect is strong, it would change the morphology
983 of the source and increase the total expected gamma-ray counts from any source. The PPPC [44]
984 provides tools in Mathematica for calculating the impact of ICS for an arbitrary location in the
985 sky for a specified annihilation channel. We calculated the change in gamma-ray counts for DM
986 annihilation to primary $e\bar{e}$ for RA and Dec corresponding to Segue1 and Coma Berenices. These
987 dSphs were chosen because they are the strongest contributors to the limit. $e\bar{e}$ was selected because
988 it would have the largest number of high energy electrons. The effect was found to be on the order
989 of 10^{-7} on the gamma-ray spectrum. As a result, this systematic is not considered in our analysis.

990 **6.7.2 Point Source Versus Extended Source Limits**

991 The previous DM search toward dSph approximated the dSphs as point sources [46]. In
992 this analysis, the dSphs are implemented as extended with J-factor distributions following those
993 produced by [53]. The resolution of the cited map is much finer than HAWC's angular resolution.
994 The vast majority of the J-factor distribution is represented on the central HAWC pixel of the dSph
995 spatial map. However, the neighboring 8 pixels are not negligible and contribute to our limit.

996 Figure 6.11 shows a substantial improvement to the limit for Segue1. Fig. 6.12 however showed
997 identical limits. These disparities are best explained by the relative difference in their J-Factors.
998 Both dSphs pass almost overhead the HAWC detector, however Segue1 has the larger J-Factor
999 between the two. Adjacent pixels to the central pixel will therefore contribute to the limits. This is
1000 the case for other dSph that are closer to overhead the HAWC detector.

1001 Comparison plots for all sources and the combined limit can be found in the sandbox for the
1002 Glory Duck project.

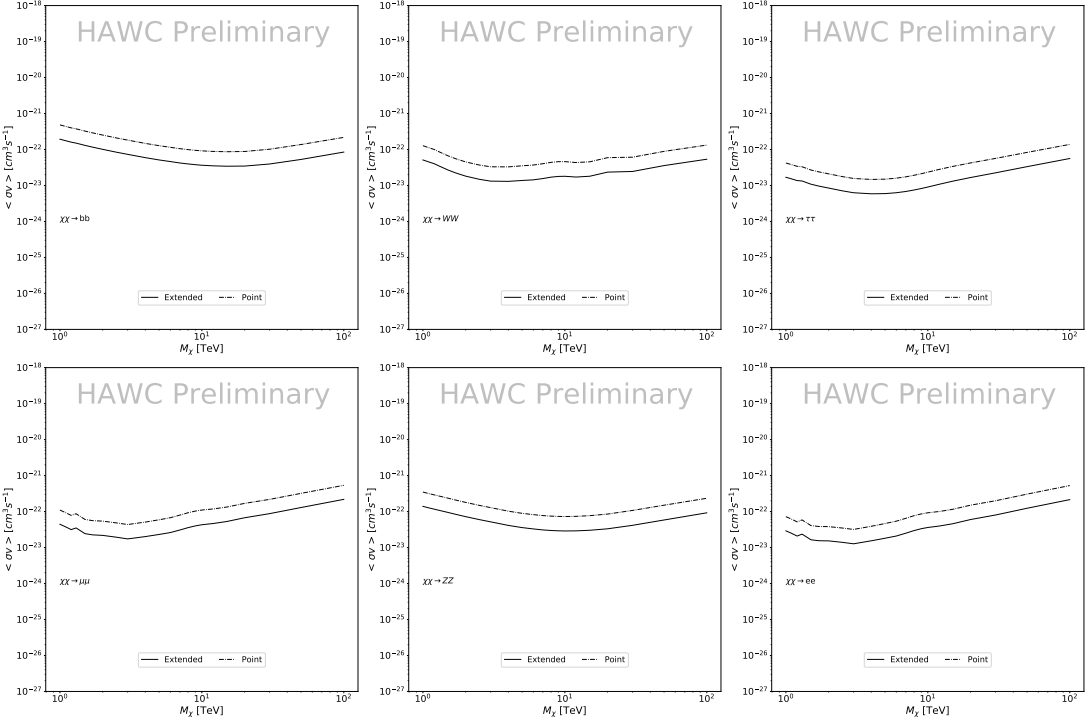


Figure 6.11 Comparisons of the combined limits at 95% confidence level for a point source analysis and extended source using [53] \mathcal{GS} J-factor distributions and PPPC [44] annihilation spectra. Shown are the limits for Segue1 which will have the most significant impact on the combined limit. 6 of the 7 DM annihilation channels are shown. Solid lines are extended source studies. Dashed lines are point source studies. Overall, the extended source analysis improves the limit by a factor of 2.

1003 6.7.3 Impact of Pointing Systematic

1004 During the analysis it was discovered that reconstruction of gamma-rays. Slides describing this
 1005 systematic can be found [here](#). Shown on the presentation is dependence on the pointing systematic
 1006 on declination. New spatial profiles were generated for every dSph and limits were computed for
 1007 the adjusted declination.

1008 Section 6.7.3 demonstrates the impact of this systematic for all DM annihilation channels
 1009 studied by HAWC. The impact is a tiny improvement, yet mostly identical, to the combined limits.

1010 6.8 J-factor distributions

1011 6.8.1 Numerical integration of \mathcal{GS} maps

1012 It was discovered well after the HAWC analysis was completed that the published tables from
 1013 \mathcal{GS} [45] quoted median J-factors were computed in a non-trivial manner. The assumption myself

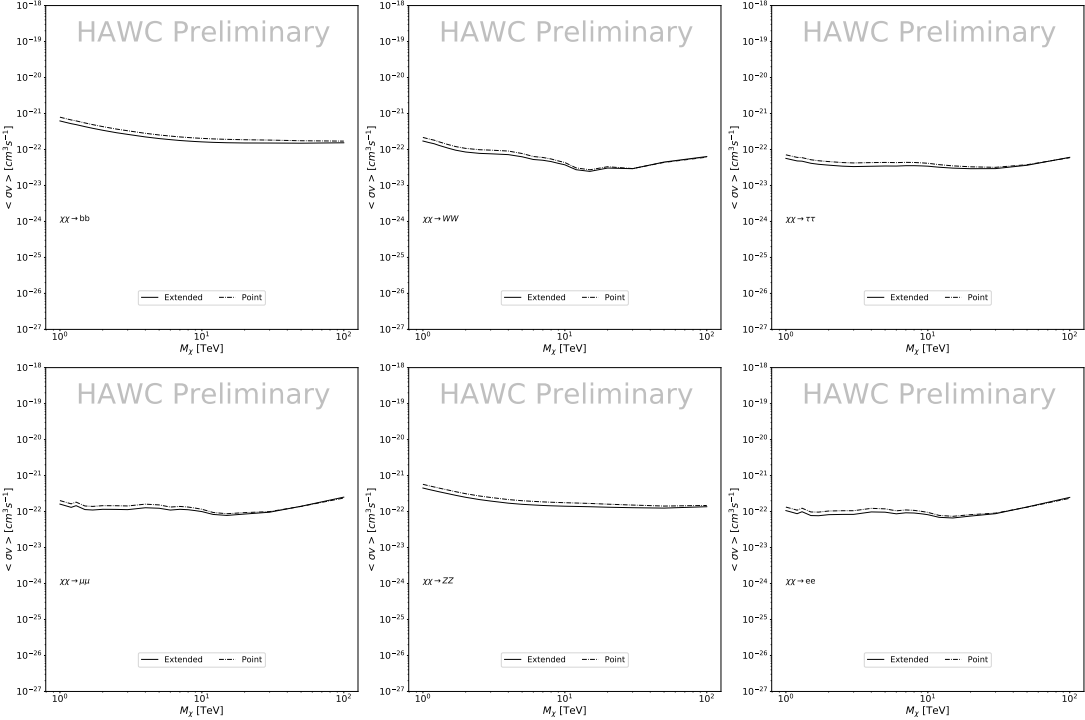


Figure 6.12 Same as Fig. 6.11 on Coma Berenices. This dSph also contributes significantly to the limit. The limits are identical in this case.

and collaborators had been that the published tables represented the J -factor as a function of θ for the best global fit model on a per-source basis. However, this is not the case. Instead, what is published are the best fit model for each dwarf that only considers stars up to the angular separation θ . Therefore, the model is changing for each value of θ for each dwarf. Yet, the introduced features from unique models at each θ are much smaller than the angular resolution of HAWC. It is not expected for these effects to impact the limits and TS greatly as a result.

Median J -factor model profiles were provided by the authors. New maps were generated and analyzed for Segue1 and Coma Berenices. Figure 6.14 shows the differential between maps generated with the method from Section 6.8.1 and from the authors of [45]. These maps were reanalyzed for all SM DM annihilation channels. Upper limits for these channels are shown in Figure 6.15

From Figure 6.15, we can see that the impact of these model difference was no substantial. The observed impact was a fractional effect which is much smaller than the impact from selecting another DM spatial distribution model as was shown in Figure 6.10.

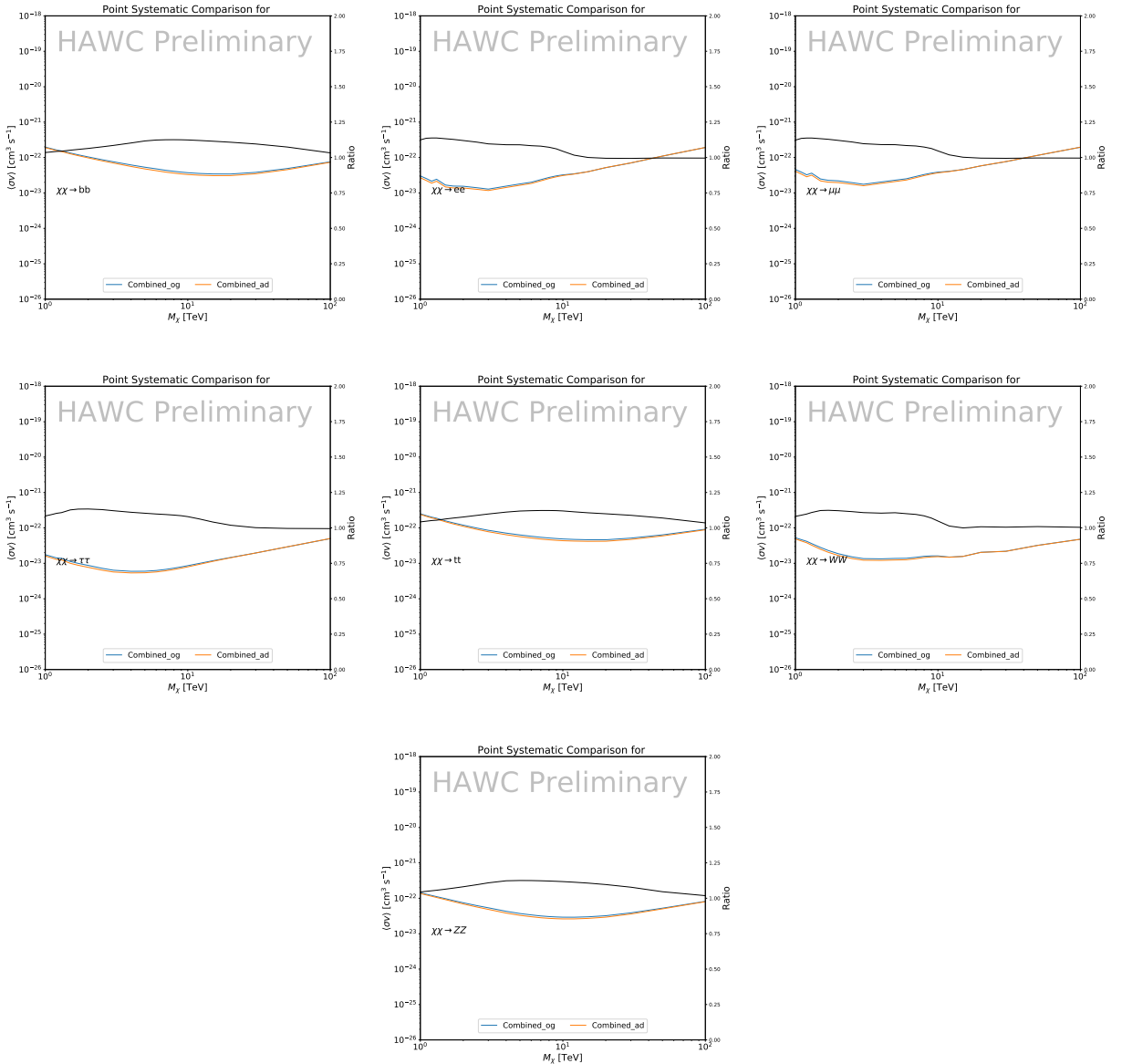


Figure 6.13 Comparison of combined limits when correcting for HAWC's pointing systematic. All DM annihilation channels are shown. The solid black line is the ratio between published limit to the declination corrected limit. The blue solid line or "Combined_og" represented the limits computed for Glory Duck. The solid orange line or "Combined_ad" represented the limits computed after correcting for the pointing systematic.

1028 6.8.2 $\mathcal{G}\mathcal{S}$ Versus \mathcal{B} spatial models

1029 We show in this appendix a comparison between the J -factors computed by Geringer-Sameth
 1030 *et al.* [53] (the $\mathcal{G}\mathcal{S}$ set) and the ones computed by Bonnivard *et al.* [47, 55] (the \mathcal{B} set). The
 1031 $\mathcal{G}\mathcal{S}$ J -factors are computed through a Jeans analysis of the kinematic stellar data of the selected

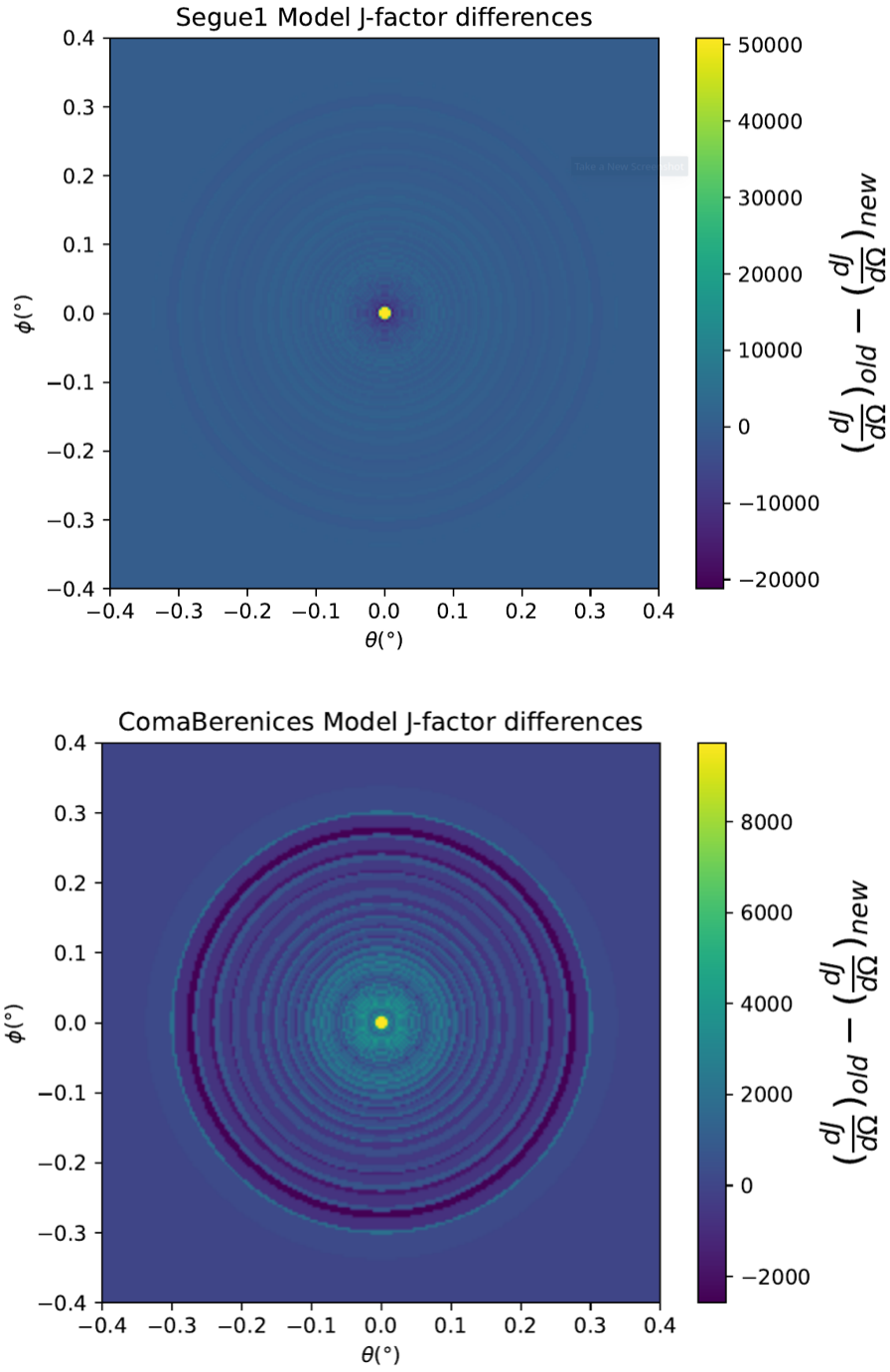


Figure 6.14 Differential map of dJ/Ω from model built in Section 6.8.1 and profiles provided directly from authors. (Top) Differential from Segue1. (bottom) Differential from Coma Berenices. Note that their scales are not the same. Segue1 shows the deepest discrepancies which is congruent with its large uncertainties. Both models show anuli where unique models become apparent.

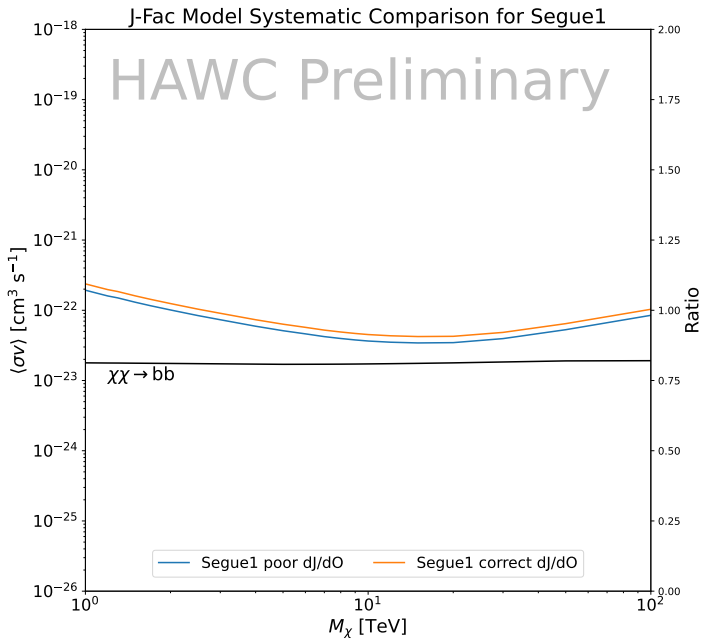
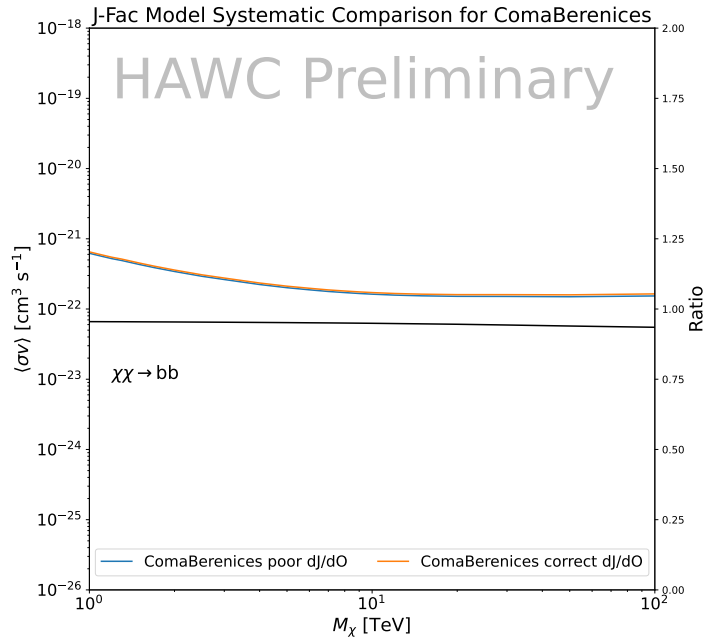


Figure 6.15 HAWC limits for Coma Berenices (top) and Segue1 (bottom) for two different map sets. Blue lines are limits calculated on maps with poor model representation. Orange lines are limits calculated on spatial profiles provided by the authors of [45]. Black line is the ratio of the poor spatial model limits to the corrected spatial models. The left y-axis measures $\langle \sigma v \rangle$ for the blue and orange lines. The right y-axis measures the ratio and is unitless.

1032 dSphs, assuming a dynamic equilibrium and a spherical symmetry for the dSphs. They adopted
1033 the generalized DM density distribution, known as Zhao-Hernquist, introduced by [58], carrying
1034 three additional index parameters to describe the inner and outer slopes, and the break of the
1035 density profile. Such a profile parametrization allows the reduction of the theoretical bias from
1036 the choice of a specific radial dependency on the kinematic data. In other words, the increase of
1037 free parameters with the use of the Zhao-Hernquist profile allows a better description of the mass
1038 density distribution of dark matter.

1039 In addition, a constant velocity anisotropy profile and a Plummer light profile [59] for the stellar
1040 distribution were assumed. The velocity anisotropy profile depends on the radial and tangential
1041 velocity dispersion. However, its determination remains challenging since only the line-of-sight
1042 velocity dispersion can be derived from velocity measurements. Therefore, the parametrization of
1043 the anisotropy profile is obtained from simulated halos (see [60] for more details). They provide the
1044 values of the J -factors of regions extending to various angular radius up to the outermost member
1045 star.

1046 The \mathcal{B} J -factors were computed through a Jeans analysis taking into account the systematic
1047 uncertainties induced by the DM profile parametrization, the radial velocity anisotropy profile, and
1048 the triaxiality of the halo of the dwarf galaxies. They performed a more complete study of the dSph
1049 kinematics and dynamics than \mathcal{GS} for the determination of the J -factor. Conservative values of the
1050 J -factors where obtained using an Einasto DM density profile [61], a realistic anisotropy profile
1051 known as the Baes & Van Hese profile [62] which takes into account that the inner regions can be
1052 significantly non-isotropic, and a Zhao-Hernquist light profile [58].

1053 For both sets, J -factor values are provided for all dSphs as a function of the radius of the
1054 integration region [53, 47, 55]. Table 6.1 shows the heliocentric distance and Galactic coordinates
1055 of the twenty dSphs, together with the two sets of J -factor values integrated up to the outermost
1056 observed star for \mathcal{GS} and the tidal radius for \mathcal{B} . Both J -factor sets were derived through a Jeans
1057 analysis based on the same kinematic data, except for Draco where the measurements of [63] have
1058 been adopted in the computation of the \mathcal{B} value. The computations for producing the \mathcal{GS} and \mathcal{B}

1059 samples differ in the choice of the DM density, velocity anisotropy, and light profiles, for which the
1060 set \mathcal{B} takes into account some sources of systematic uncertainties.

1061 Figure 6.16 and Figure 6.17 show the comparisons for the J -factor versus the angular radius
1062 for each of the 20 dSphs used in this study. The uncertainties provided by the authors are also
1063 indicated in the figures. For the \mathcal{GS} set, the computation stops at the angular radius corresponding
1064 to the outermost observed star, while for the \mathcal{B} set, the computation stops at the angular radius
1065 corresponding to the tidal radius.

1066 6.9 Discussion and Conclusions

1067 In this multi-instrument analysis, we have used observations of 20 dSphs from the gamma-ray
1068 telescopes Fermi-LAT, H.E.S.S., MAGIC, VERITAS, and HAWC to perform a collective DM
1069 search annihilation signals. The data were combined across sources and detectors to significantly
1070 increase the sensitivity of the search. We have observed no significant deviation from the null, no
1071 DM, hypothesis, and so present our results in terms of upper limits on the annihilation cross-section
1072 for seven potential DM annihilation channels.

1073 Fermi-LAT brings the most stringent constraints for continuum channels below approximately
1074 1 TeV. The remaining detectors dominate at higher energies. Overall, for multi-TeV DM mass,
1075 the combined DM constraints from all five telescopes are 2-3 times stronger than any individual
1076 telescope for multi-TeV DM.

1077 Derived from observations of many dSphs, our results produce robust limits given the DM
1078 content of the dSphs is relatively well constrained. The obtained limits span the largest mass
1079 range of any WIMP DM search. Our combined analysis improves the sensitivity over previously
1080 published results from each detector which produces the most stringent limits on DM annihilation
1081 from dSphs. These results are based on deep exposures of the most promising known dSphs with
1082 the currently most sensitive gamma-ray instruments. Therefore, our results constitute a legacy of
1083 a generation of gamma-ray instruments on WIMP DM searches towards dSphs. Our results will
1084 remain the reference in the field until a new generation of more sensitive gamma-ray instruments
1085 begin operations, or until new dSphs with higher J -factors are discovered.

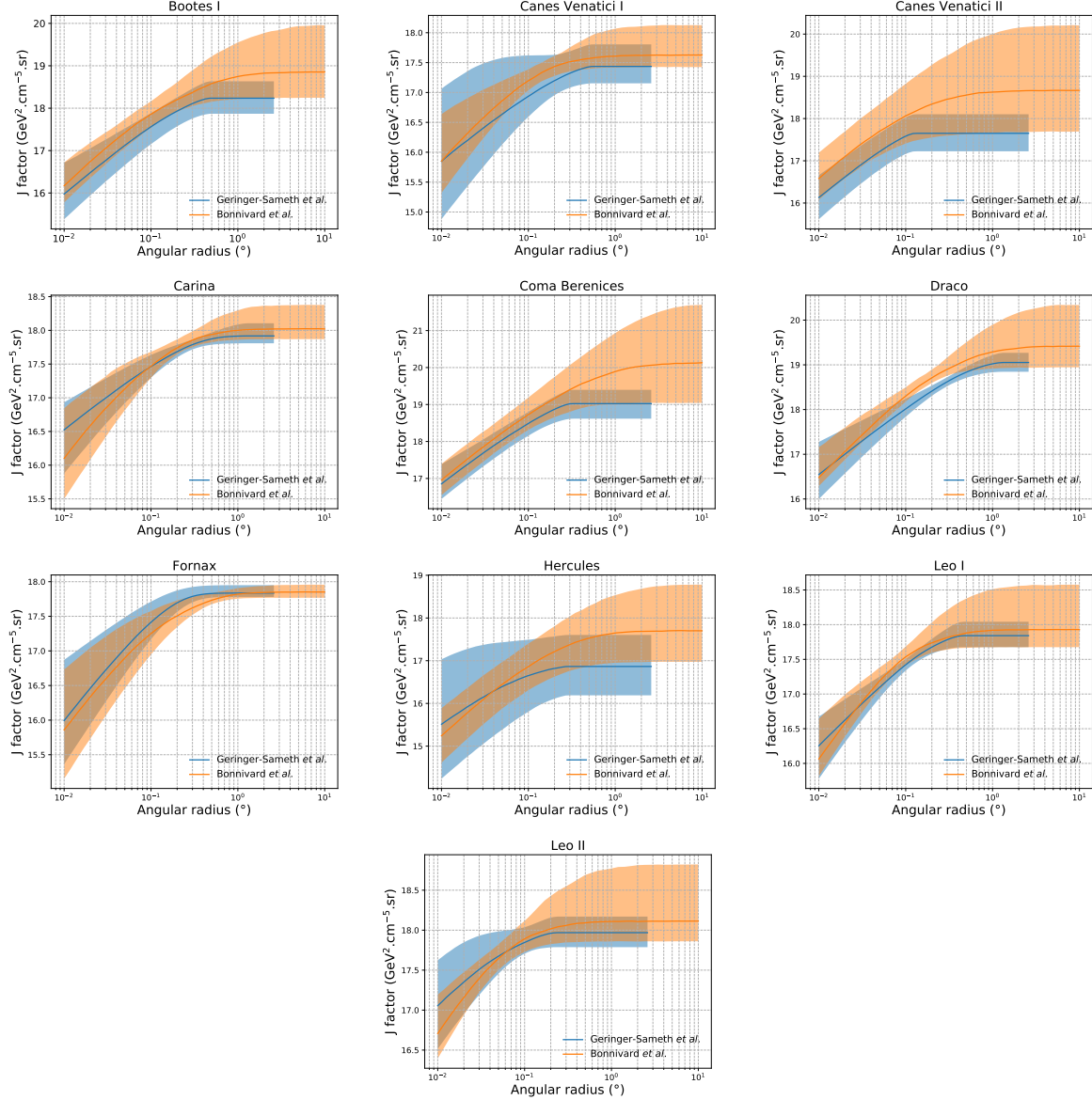


Figure 6.16 Comparisons between the J -factors versus the angular radius for the computation of J factors from Ref. [53] (\mathcal{GS} set in Table 6.1) in blue and for the computation from Ref. [47, 55] (\mathcal{B} set in Tab. 6.1) in orange. The solid lines represent the central value of the J -factors while the shaded regions correspond to the 1σ standard deviation.

This analysis serves as a proof of concept for future multi-instrument and multi-messenger combination analyses. With this collaborative effort, we have managed to sample over four orders in magnitude in gamma-ray energies with distinct observational techniques. Determining the nature of DM continues to be an elusive and difficult problem. Larger datasets with diverse measurement techniques could be essential to tackling the DM problem. A future collaboration using similar

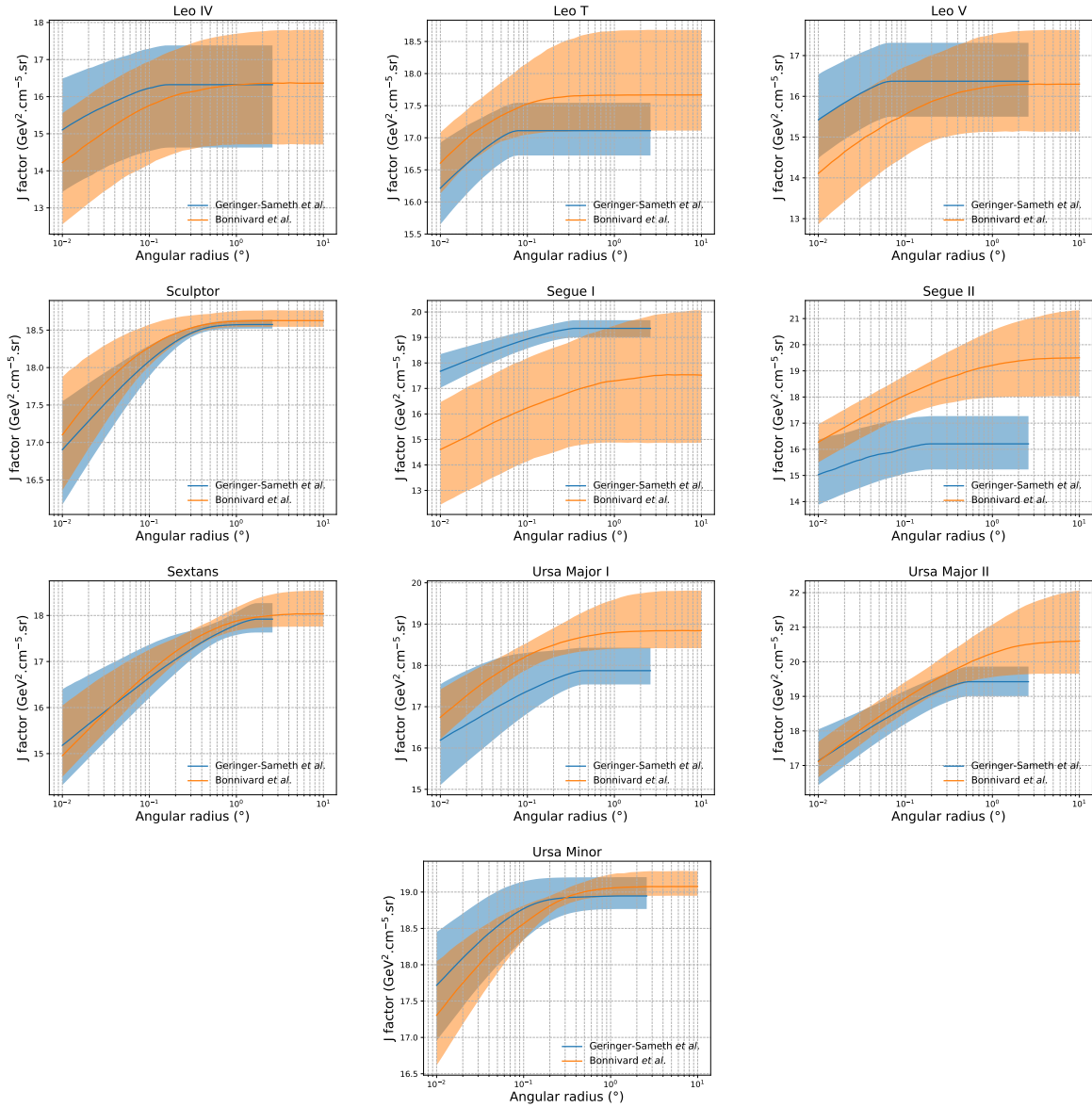


Figure 6.17 Comparisons between the J -factors versus the angular radius for the computation of J factors from Ref. [53] (\mathcal{GS} set in Tab. 6.1) in blue and for the computation from Ref. [47, 55] (\mathcal{B} set in Tab. 6.1) in orange. The solid lines represent the central value of the J -factors while the shaded regions correspond to the 1σ standard deviation.

1091 techniques as the ones described in this paper could grow even beyond gamma rays. The models we
 1092 used for this study include annihilation channels with neutrinos in the final state. Advanced studies
 1093 could aim to merge our results with those from neutrino observatories with large data sets. Efforts
 1094 are already underway to add data from the IceCube, ANTARES, and KM3NeT observatories to
 1095 these gamma-ray results.

1096 From this work, a selection of the best candidates for observations, according to the latest
1097 knowledge on stellar dynamics and modelling techniques for the derivation of the J -factors on
1098 the potential dSphs targets, is highly desirable at the time that new experiments are starting their
1099 dark matter programs using dSphs. Given the systematic uncertainty inherent to the derivation of
1100 the J -factors, an informed observational strategy would be to select both objects with the highest
1101 J -factors that could lead to DM signal detection, and objects with robust J -factor predictions, i.e.
1102 with kinematic measurements on many bright stars, which would strengthen the DM interpretation
1103 reliability of the observation outcome.

1104 This analysis combines data from multiple telescopes to produce strong constraints on astro-
1105 physical objects. From this perspective, these methods can be applied beyond just DM searches.
1106 Almost every astrophysical study can benefit from multi-telescope, multi-wavelength gamma-ray
1107 studies. We have enabled these telescopes to study the cosmos with greater precision and detail.
1108 Many astrophysical searches can benefit from multi-instrument gamma-ray studies, for which our
1109 analysis lays the foundation.

CHAPTER 7

MULTITHREADING HAWC ANALYSES FOR DARK MATTER SEARCHES

7.1 Introduction

HAWC's current software suite, plugins to 3ML, does not fully utilize computational advancements of recent decades. Said advancements include the proliferation of Graphical Processing Units (GPUs), and multithreading on multi-core processors. The analysis described in chapter 6 took up to 3 months of human time waiting for the full gambit of data analysis and simulation of background to run. Additionally, with the addition of a 2D binning scheme, f_{hit} and NN, the compute time is expected to grow. Although excessive computing time was, in part, from an intense use of a shared computing cluster, it was evident that there was room for improvement. In HAWC's next generation dSph DM search, I decided to develop codes that would utilize the multi-core processors on modern high performance computing clusters. The results of this work are featured in this chapter and brought a human timing improvement to computation that scales as $1/N$ where N is the number of threads.

7.2 Dataset and Background

This section enumerates the data and background methods used for HAWC's multi-threaded study of dSphs. Section 7.2.1 and Section 7.2.2 are most useful for fellow HAWC collaborators looking to replicate a multithreaded dSph DM search.

7.2.1 Itemized HAWC files

- Detector Resolution: `refit-Pass5-Final-NN-detRes-zenith-dependent.root`
- Data Map: `Pass5-Final-NN-maptree-ch103-ch1349-zenith-dependent.root`
- Spectral Dictionary: `HDMspectra_dict_gamma.npy`

7.2.2 Software Tools and Development

This analysis was performed using HAL and 3ML [42, 43] in Python version 3. I built software in collaboration with Michael Martin and Letrell Harris to implement the *Dark Matter Spectra from*

1134 *the Electroweak to the Planck Scale* (HDM) [64] and dSphs spatial model from [65] for HAWC
1135 analysis. A NumPy dictionary of HDM was made for Py3. The corresponding Python3 file is
1136 `HDMspectra_dict_gamma.npy`. These files can also be used for decay channels and tools are
1137 provided in HDM’s [git repository](#) [64]. The analysis was performed using the Neural Network
1138 energy estimator for Pass 5.F. A description of this estimator was provided in chapter 4. **TODO:**
1139 **define a subsection when it’s written** All other software used for data analysis, DM profile generation,
1140 and job submission to SLURM are also kept in my sandbox in the [Dark Matter HAWC](#) project.
1141 The above repository also incorporates the model inputs used previously in Glory Duck, described
1142 in chapter 6

1143 7.2.3 Data Set and Background Description

1144 The HAWC data maps used for this analysis contain 2565 days of data between runs 2104 (

1145 **TODO: Day start**) and 7476 (**TODO: day end**). They were generated from pass 4.0 reconstruction.

1146 The analysis is performed using the NN energy estimator with bin list:

1147 B1C0Ea, B1C0Eb, B1C0Ec, B1C0Ed, B1C0Ee, B2C0Ea, B2C0Eb, B2C0Ec, B2C0Ed, B2C0Ee,
1148 B3C0Ea, B3C0Eb, B3C0Ec, B3C0Ed, B3C0Ee, B3C0Ef, B4C0Eb, B4C0Ec, B4C0Ed, B4C0Ee,
1149 B4C0Ef, B5C0Ec, B5C0Ed, B5C0Ee, B5C0Ef, B5C0Eg, B6C0Ed, B6C0Ee, B6C0Ef, B6C0Eg,
1150 B6C0Eh, B7C0Ee, B7C0Ef, B7C0Eg, B7C0Eh, B7C0Ei, B8C0Ee, B8C0Ef, B8C0Eg, B8C0Eh,
1151 B8C0Ei, B8C0Ej, B9C0Ef, B9C0Eg, B9C0Eh, B9C0Ei, B9C0Ej, B10C0Eg, B10C0Eh,
1152 B10C0Ei, B10C0Ej, B10C0Ek, B10C0El

1153 Bin 0 was excluded as it has substantial hadronic contamination and poor angular resolution.

1154 Background considerations and source selection was identical to Section 6.2, and no additional
1155 arguments are provided here. Many of the HAWC systematics explored in Section 6.7 also apply
1156 for this DM search and are not added upon here.

1157 7.3 Analysis

1158 The analysis and its systematics are almost identical to Section 6.3. Importantly, we use the
1159 same Equation (6.1) and Equation (6.2) for estimating the gamma-ray flux at HAWC from our

1160 sources. We add on to the previous study with a search for DM decay. The flux equations for DM
 1161 decay are

$$\frac{d\Phi_\gamma}{dE_\gamma} = \frac{1}{4\pi\tau m_\chi} \frac{dN_\gamma}{dE_\gamma} \times \int_{\text{source}} d\Omega \int_{l.o.s} \rho_\chi dl(r, \theta') \quad (7.1)$$

1162 with a new quantity, the D factor, defined as

$$D = \int d\Omega \int_{l.o.s} dl \rho_\chi(r, \theta') \quad (7.2)$$

1163 Software was written to accomodate DM decay from dSphs, however decay profiles were not
 1164 received from $\mathcal{L}\mathcal{S}$ by the time of writing this tehsis.

1165 **7.3.1 $\frac{dN_\gamma}{dE_\gamma}$ - Particle Physics Component**

1166 For these spectra, we import HDM with Electroweak (EW) corrections and additional correc-
 1167 tions for neutrinos above the EW scale [64]. The spectrum is implemented as a model script in
 1168 astromodels for 3ML. A comprehensive description of EW corrections and neutrino considerations
 1169 are provided later in [TODO: refeance MM nu duck](#).

1170 Figure 7.1 demonstrates the impact of changes from HDM on DM annihilation to W bosons.
 1171 A class in astromodels was developed to include HDM and is aptly named `HDMspectra` within
 1172 `DM_models.py`. The SM DM annihilation channels studied here are $\chi\chi \rightarrow$:

1173 e^+e^- , $\mu^+\mu^-$, $\tau^+\tau^-$, $b\bar{b}$, $t\bar{t}$, gg , W^+W^- , ZZ , $c\bar{c}$, $u\bar{u}$, $d\bar{d}$, $s\bar{s}$, $\nu_e\bar{\nu}_e$, $\nu_\mu\bar{\nu}_\mu$, $\nu_\tau\bar{\nu}_\tau$, $\gamma\gamma$, hh .

1174 For $\gamma\gamma$ and ZZ , a substantial fraction of the signal photons are expected to have total energy equal
 1175 m_χ [64]. This introduces a δ -function that is much narrower than the energy resolution of the
 1176 HAWC detector. To ensure that this feature is not lost in the likelihood fits, the 'line' feature is
 1177 convolved with a gausian kernel with a 1σ width of $0.05 \cdot m_\chi$ and total kernel window of $\pm 4\sigma$.
 1178 This difers from HAWC's previous line study where 30% of HAWC's energy resolution was used
 1179 for the kernel [66]. The NN energy estimator's strength compared to f_{hit} at low gamma-ray energy
 1180 enables smaller resolutions in addition to low energy tails in the spectral models [64]. $\chi\chi \rightarrow \gamma\gamma$
 1181 and ZZ spectral hypotheses are shown in Figure 7.2. Spectral models for the remaining annihilation
 1182 channels are plotted for each m_χ in Figure B.1.

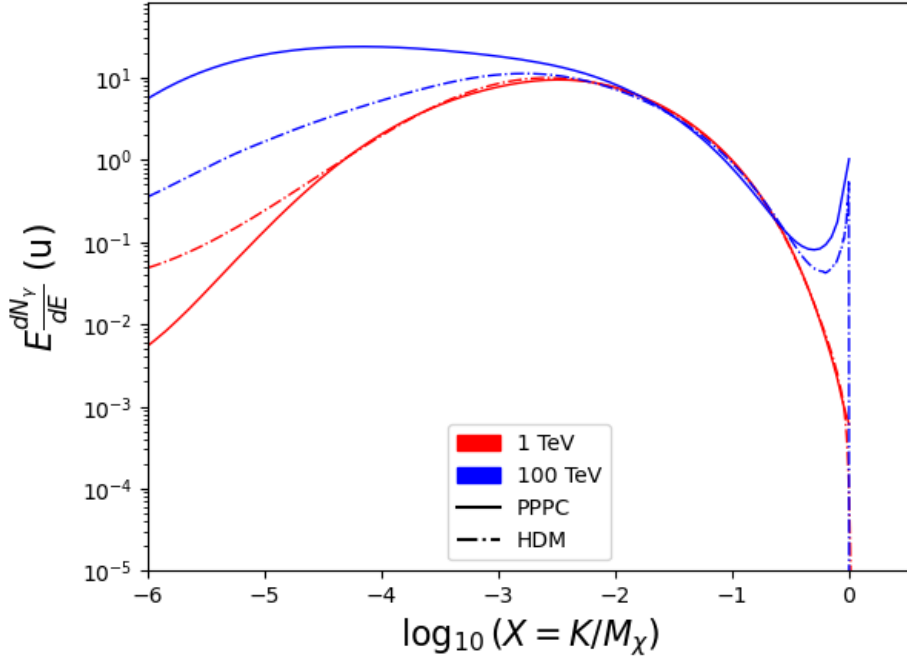


Figure 7.1 Difference between spectral hypotheses from PPPC [44] and HDM [64]. Shown is the expected DM annihilation spectrum for $\chi\chi \rightarrow W^-W^+$. Solid lines are spectral models with EW corrections from the PPPC. Dash-dot lines are spectral models from HDM. Red lines are models for $M_\chi = 1$ TeV. Blue lines represent models for $M_\chi = 100$ TeV.

7.3.2 *J* and *D*- Astrophysical Components

The *J*-factor profiles for each source are imported from Louis Strigari et al. (referred to with

$\mathcal{L}S$) [65]. Profiles in $\frac{dJ}{d\Omega}(\theta)$ up to $\theta = 0.5^\circ$ were provided directly from the authors. Map generation from these profiles were almost identical to Section 6.3.2 except that a higher order trapezoidal integral was used for the normalization of the square, uniformly-spaced map:

$$p^2 \cdot \sum_{i=0}^N \sum_{j=0}^M w_{i,j} \frac{d\mathcal{K}}{d\Omega}(\theta_{i,j}, \phi_{i,j}) \quad (7.3)$$

\mathcal{K} is either *J* or *D* for the spatial distributions of annihilation or decay respectively. *p* is the angular side of one pixel in the map. $w_{i,j}$ is a weight assigned the following ways:

$w_{i,j} = 1$ if $(\theta_{i,j}, \phi_{i,j})$ is fully within the region of integration

$w_{i,j} = 1/2$ if $(\theta_{i,j}, \phi_{i,j})$ is on an edge of the region of integration

$w_{i,j} = 1/4$ if $(\theta_{i,j}, \phi_{i,j})$ is on a corner of the region of integration

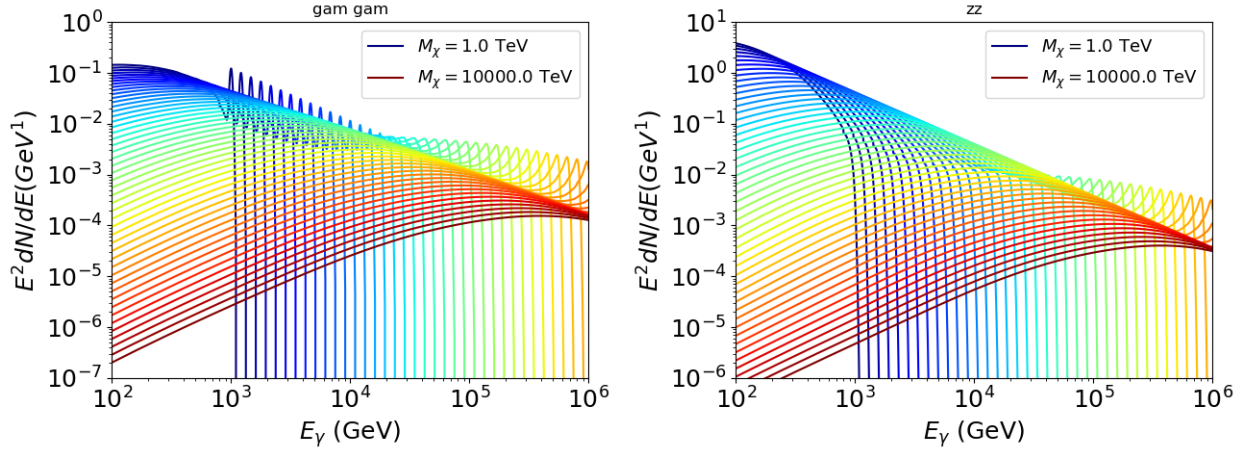


Figure 7.2 Photon spectra for $\chi\chi \rightarrow \gamma\gamma$ (left) and $\chi\chi \rightarrow ZZ$ (right) after gaussian convolution of line features. Both spectra have δ -features at photon energies equal to the DM mass. Bluer lines are annihilation spectra with lower DM mass. Redder lines are spectra from larger DM mass. All Spectral models are sourced from the Heavy Dark Matter models [64]. Axes are drawn roughly according to the energy sensitivity of HAWC.

1193 Figure 7.3 shows the median and $\pm 1\sigma$ maps used as input for DM annihilation studied by \mathcal{LS} .

1194 **7.3.3 Source Selection and Annihilation Channels**

1195 HAWC's sources for this multithreaded analysis include Coma Berenices, Draco, Segue 1, and
 1196 Sextans. \mathcal{LS} observes up to 43 sources in its publication, however only 4 of the best fit profiles were
 1197 provided at the time this thesis was written. A full description of each source used in this analysis
 1198 is found in Table 7.1.

1199 This analysis improves on chapter 6 in the following ways. Previously, the particle physics

Name	Distance (kpc)	l, b ($^\circ$)	$\log_{10} J$ (\mathcal{LS} set) $\log_{10}(\text{GeV}^2 \text{cm}^{-5} \text{sr})$
Coma Berenices	44	241.89, 83.61	$19.00^{+0.36}_{-0.35}$
Draco	76	86.37, 34.72	$18.83^{+0.12}_{-0.12}$
Segue I	23	220.48, 50.43	$19.12^{+0.49}_{-0.58}$
Sextans	86	243.50, 42.27	$17.73^{+0.13}_{-0.12}$

Table 7.1 Summary of the relevant properties of the dSphs used in the present work. Column 1 lists the dSphs. Columns 2 and 3 present their heliocentric distance and galactic coordinates, respectively. Column 4 reports the J -factors of each source given from the \mathcal{LS} studies and estimated $\pm 1\sigma$ uncertainties. The values $\log_{10} J$ (\mathcal{LS} set) [65] correspond to the mean J -factor values for a source extension truncated at 0.5° .

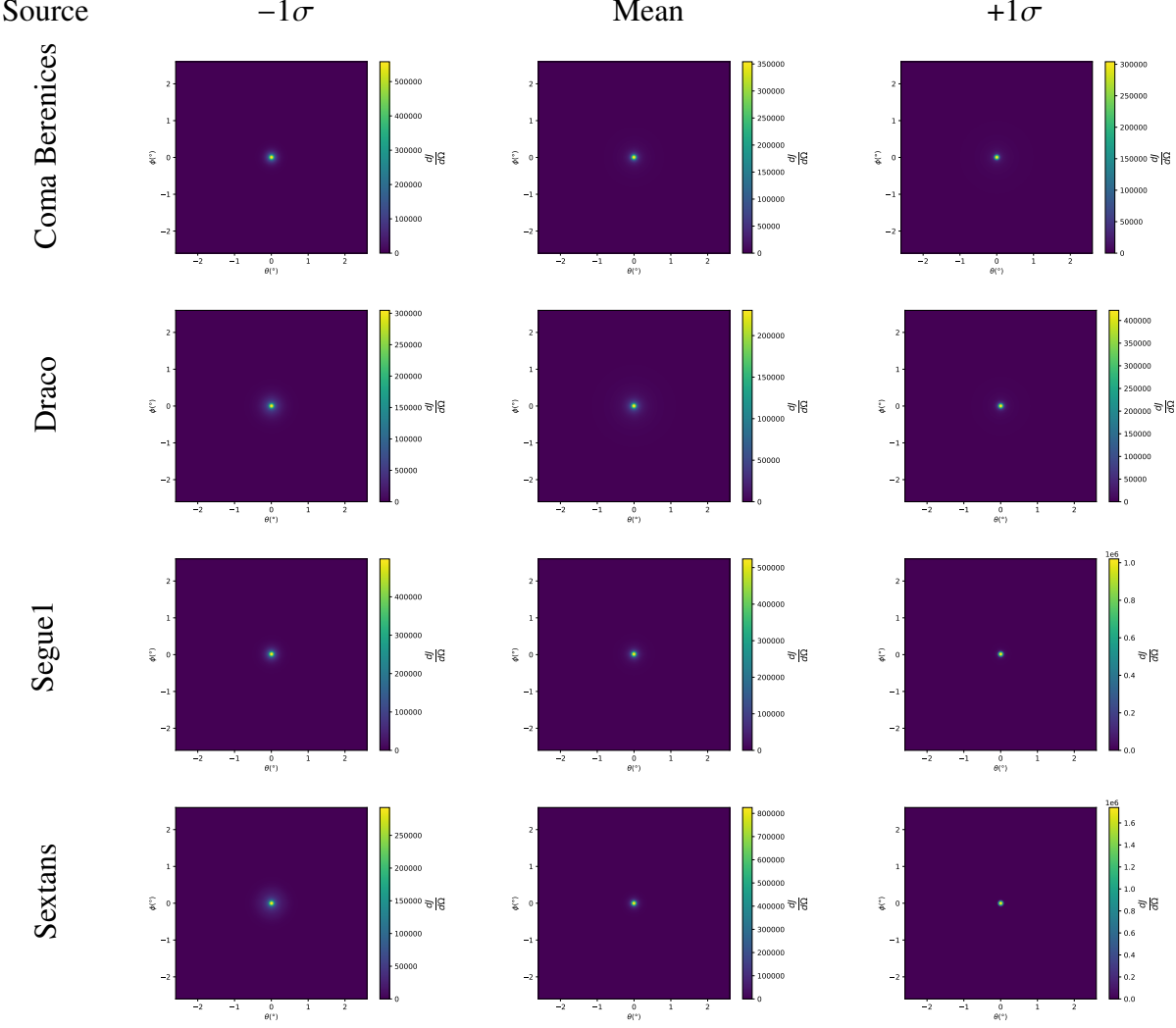


Figure 7.3 $\frac{dJ}{d\Omega}$ maps for Coma Berenices, Draco, Segue1, and Sextans. Columns are divided for the $\pm 1\sigma$ uncertainties in $dJ/d\Omega$ around the mean value from \mathcal{LS} [65]. Origin is centered on the specific dwarf spheroidal galaxies (dSph). θ and ϕ axes are the angular separation from the center of the dwarf

model used for gamma-ray spectra from DM annihilation was from the PPPC [44] which missed important considerations relevant for the neutrino sector. HDM is used to account for this shortfall [64]. HDM also models DM to the Planck scale which permits HAWC to probe PeV scale DM. For this study, we sample DM masses: 1 TeV - 10 PeV with 6 mass bins per decade in DM mass. In the case of line spectra ($\chi\chi \rightarrow \gamma\gamma$, or ZZ), we double the mass binning to 12 DM mass bins per decade in DM mass. A larger source catalog is used that uses a Navarro–Frenk–White (NFW) spatial DM distribution from \mathcal{LS} [65]. Because NFW has fewer parameters than what is used

1207 for \mathcal{GS} , \mathcal{LS} is able to fit ultra-faint dwarves, expanding the number of sources available for DM
1208 searches. Finally, the gamma-ray ray dataset is much larger. The study performed here analyzes
1209 2565 days of data compared to 1017 days analyzed in chapter 6.

1210 **7.4 Likelihood Methods**

1211 These are identical to Section 6.4.1 and no additional changes are made to the likelihood. Bins
1212 in this analysis are expanded to include HAWC’s NN energy estimator.

1213 **7.5 Computational Methods: Multithreading**

1214 Previously, as in Section 6.3, the likelihood was minimized for one model at a time. One
1215 model in this case representing a DM annihilation channel, DM mass, and dSph. In an effort
1216 to conserve human and CPU time, jobs submitted for high performance computing contained a
1217 list of DM masses to iterate over for likelihood fitting. Jobs were then trivially parallelized for
1218 each permutation of the two lists: CHANS (SM annihilation channel) and SOURCES (dSph spatial
1219 templates). The lists for CHANS and SOURCES are found in Section 7.3.1 and Table 7.1, respectively.
1220 Initially, 11 DM mass bins were serially sampled for one job defined by a [SM channel, dSph] set.
1221 Computing the likelihoods would take between 1.5 to 2 hrs, stocastically, for a job. We expect to
1222 compute likelihoods for data and 300 Poisson background trials. The estimated CPU time based on
1223 the above for all SM annihilation channels (17) and 25 sources (all \mathcal{LS} sources withing HAWC’s
1224 field of view) amounted to 127,925 jobs. In total, 1,407,175 likelihood fits and profiles would be
1225 computed for the 11 mass bins we wished to study. The estimated CPU time ranged between 10k
1226 CPU days - 8k CPU days. Human time is more challenging to estimate as job allocation is stochastic
1227 and highly dependant on what other users are submitting, yet it is unlikely that all jobs would run
1228 simultaneously. Therefore we can expect human time to be about as long as was seen in chapter 6
1229 which was on the order of months to fully compute on a smaller analysis. A visual aid to describe
1230 how jobs were organized is provided in Figure 7.4.

1231 The computational needs for this next generation DM analysis are extreme and is unlike other
1232 analyses performed on HAWC. It became clear that there was a lot to gain from optimzing how
1233 the likelihoods are computed. This section discusses how multi-threading was applied to solve and

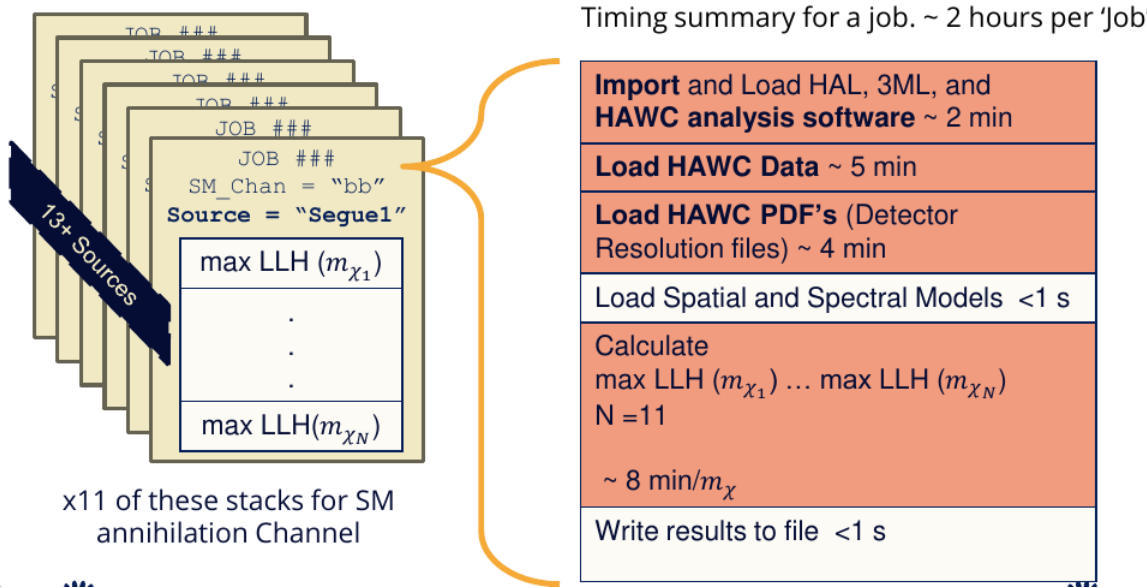


Figure 7.4 Infographic on how jobs and DM computation was organized in Section 6.3. Jobs were built for each permutation of CHANS and SOURCES shown by the left block in the figure. Each job, which took on the order 2 hrs to compute, had the following work flow: 1. Import HAWC analysis software, 2 min to run. 2. Load HAWC count maps, 5 min to run. 3. Load HAWC energy and spatial resolutions, 4 min. 5. Load DM spatial source templates and spectral models, less than 1 s. 6. Perform likelihood fit on data and model, about 8 min per DM mass. 7. Write results to file, less than 1s.

1234 reduce HAWC's computing of likelihoods for large parameter spaces like in DM searches.

1235 7.5.1 Relevant Foundational Information

1236 The profiling of the likelihood for HAWC is done via gradient descent where the normalization
 1237 of Equation (6.1) (linearly correlated with $\langle \sigma v \rangle$) is rescaled in the descent. Additionally, we sample
 1238 the likelihood space for a defined list of $\langle \sigma v \rangle$'s described in Section 6.4.2. The time to compute
 1239 these values is not predictable or consistent because many variables can change across the full
 1240 model-space. comprehensively, these variables are:

- 1241 • m_{χ} : DM rest mass
- 1242 • CHAN : DM SM annihilation channel.
- 1243 • SOURCE : dSph within HAWC's field of view. This involves a spatial template AND coordinate
 1244 in HAWC data.

1245 • $\langle \sigma v \rangle$: Effectevely the flux normalization and free parameter in the likelihood fit.
 1246 Therefore, we develop an asynchronous, functional-parallel coding pattern. Asyncronous meaning
 1247 that the instructions and computing within a function are independent and permitted to be out of sync
 1248 with sibling computations. Functional-parallel meaning that instructions are the subject of parral-
 1249 lelization rather than threading the likelihood computation. This is close to trivial parametrization
 1250 seen in Figure 7.4 except that we seek to consolidate the loading stages (software, data, and detector
 1251 resolution loading). Reducing the total instances of loading stages and distributing access to the
 1252 reduced loads across multiple asynchronous threads is expected to reduce serial processing time and
 1253 the overhead implicit to each job in addition to saving human time.

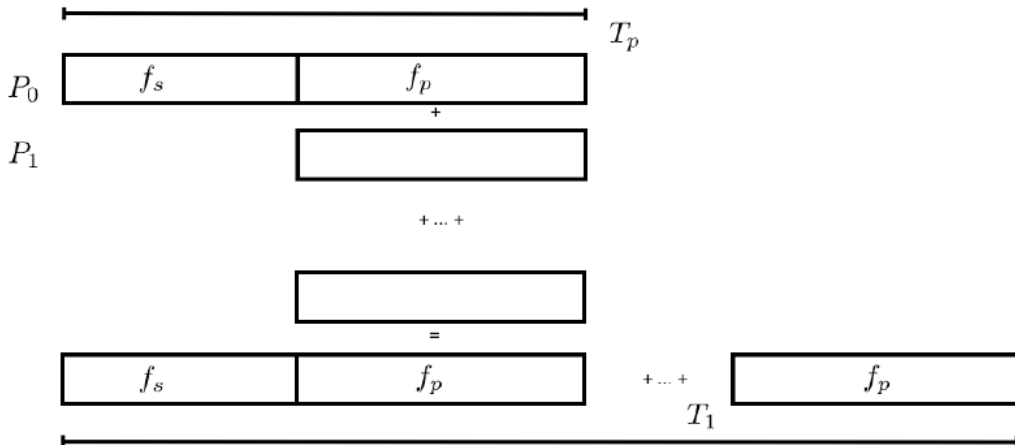


Figure 7.5 Graphic of Gustafson parallel coding pattern. f_s is the fraction of a program, in time, spent on serial computation. f_p is the fraction of computing time that is parallelizable. T_p is the total time for a parallel program to run. T_1 is the total time for a parallel program to run if only 1 processor is allocated. P_N is the N -th processor where it's row is the computation the processor performs. The Gustafson pattern is most similar to what is implemented for this analysis. Figure is pulled from [67].

1254 We need a way to measure and compare the expected speedup and efficiency gain for this
 1255 asynchronous coding pattern. I pull inspiration for timing measurement from [67] and use *Amdahl's law with hybrid programming*. Hybrid programming meaning that the computation is a mix of
 1256 distributed and shared memory programming. If we assume the code is fully parallelizable over p
 1257 processors and c threads, the ideal speedup is simply pc and ideal run-time is $T_1/(pc)$. T_1 is the
 1258

1259 total time for a parallel program to run if only 1 processor is allocated. However, the coding pattern
1260 contains some amount of unavoidable serial computation, as shown in Figure 7.5. In our case, the
1261 run time is estimated to be

$$T_{p,c} = \frac{T_1}{pc} (1 + F_s(c - 1)). \quad (7.4)$$

1262 F_s is the fraction of CPU time dedicated to serial computation. The expected speedup is

$$S_{p,c} \equiv \frac{T_1}{T_{p,c}} = \frac{pc}{1 + F_s(c - 1)}. \quad (7.5)$$

1263 From Equation (7.5), we can see that the speed up scales with p/F_s . We are free to minimize
1264 F_s asymptotically by enlarging the total models that are submitted to the thread pool, thereby
1265 shrinking the CPU fraction dedicated to serial operation. We are also free to define exactly how
1266 many threads and processors we utilize, yet eventually hit a hard cap at the hardware available on
1267 our computing cluster. HAWC uses Intel Xeon processors with 48 cores and 96 threads. This
1268 means when N-threads (c) are defined, $N \bmod 2$ cores (p) are needed. We see that a successful
1269 code scales well as the expected speedup is inversely correlated with F_s . As the total number of
1270 models sampled grows, the speedup will also.

1271 7.5.2 Implementation

1272 The multithreaded code was written in Python3 and is documented in the `dark_matter_hawc`
1273 [repository](#) within the script named `mpu_analysis.py`. A version of the script as of April 25
1274 [TODO: make sure to update on this date](#) is also provided in Section B.1 It has many dependancies
1275 including the HAWC analysis software. Figure 7.6 displays the workflow of a job with 3 threads.
1276 Within a job, SOURCE is kept fixedh . CHAN(S) remains 17 elements long. More m_χ are sampled
1277 from 11 bins up to 49 (for $\gamma\gamma$ and ZZ) and 25 (for remaining CHANS) which amounts to 12 or 6
1278 mass bins per decade. The DM mass, m_χ , and SM annihilation channels, CHANS, are permuted into
1279 a 473 element list which is split evenly across N threads where N ranges between 5 - 16. Within a
1280 thread, for each m_χ -CHAN tuple, 1001 $\langle\sigma v\rangle$ values are sampled in the likelihood, and the value of
1281 $\langle\sigma v\rangle$ that maximizes the likelihood is found. Although rare, fits that failed are handled on a case
1282 by case basis.

Timing summary for a multi-threaded job.

Import and Load HAL, 3ML, and HAWC analysis software ~ 2 min		
Load HAWC Data ~ 5 min		
Load HAWC PDF's (Detector Resolution files) ~ 4 min		
Load Spatial Model < 1s		
Load Spectra Models <1 s	Load Spectra Models <1 s	Load Spectra Models <1 s
Calculate max LLH (Chan_0, m_{χ_1}) ... max LLH (Chan_?, m_{χ_N}) N = TOTAL/N_THREADS ~ 8 min/Spec_model	Calculate max LLH (Chan_?, m_{χ_1}) ... max LLH (Chan_?, m_{χ_N}) N = TOTAL/N_THREADS ~ 8 min/Spec_model	Calculate max LLH (Chan_?, m_{χ_1}) ... max LLH (Chan_?, m_{χ_N}) N = TOTAL/N_THREADS ~ 8 min/Spec_model
Write results to file <1 s	Write results to file <1 s	Write results to file <1 s
Join Threads and terminate < 1s		

Figure 7.6 Task chart for one multi-threaded job developed for this project. Green blocks indicate a shared resource across the threads AND computation performed serially. Red blocks indicate functional parallel processing within each thread. 3 threads are represented here, yet many more can be employed during the full analysis. Jobs are defined by the SOURCE as these require unique maps to be loaded into the likelihood estimator. The m_{χ} , CHAN, and $\langle \sigma v \rangle$ variables are entered into the thread pool and allocated as evenly as possible across the threads.

1283 **7.5.3 Performance**

M Tasks	$T_{p,c}$ (hr:min:s)			
	$T_{1,1}$	$T_{1,2}$	$T_{1,8}$	$T_{1,16}$
50	1:40:37.5	0:52:43.7	0:19:13.8	0:13:44.0
74	2:22:30.0	1:15::00.6	0:25:21.3	0:15:49.8
100	(3:07:51.9)			0:20:01.4
200	(6:02:20.6)	-		0:30:44.4
473	(13:58:40.3)	-		1:09:42.9

Table 7.2 Timing summaries for analyses for serial and multithreaded processes. M tasks is the number of functional-parallel tasks ran for the computation. $T_{p,c}$ is a single run time in hours:minutes:seconds for runs utilizing p nodes and c threads. Runs are run interactively on the same computer to maximize consistency. Empty entries are indicated with '-'. (·) entries are estimated entries extrapolated from data earlier in the column.

1284 We see a tremendous reduction to human time waiting for our dSph analyses to run. Table 7.2
 1285 shows the timing summaries for analyses of different sizes and thread counts. Additionally, the
 1286 efficiency gained when consolidating the serial loading of data is also apparent in our ability to

1287 study many more tasks in about the same amount of wall time as a smaller serial computation. Trials
 1288 represented in the table were run on an AMD Opteron® processor 6344 with 48 cores, 2 threads
 1289 per core; 2.6 GHz clock. This is not the same architecture used for analysis on the computing
 1290 cluster however they are similar enough that results shown here are reasonably representative of
 1291 computing on the HAWC computing cluster. I use the Tab. 7.2 for the inferences and conclusions
 1292 in the following paragraphs.

1293 First, we want to find T_s , the time of serial computation. From Fig. 7.5, the timing for our
 1294 coding pattern can be written as

$$T_s + Mt_p = T_{1,1}^M. \quad (7.6)$$

1295 M is the number of functional-parallel tasks (represented as column 1 of Tab. 7.2), and t_p is the
 1296 average time to complete a single parallel task. $T_{1,1}^M$ is the total time for a parallel program to run if
 1297 only 1 processor is allocated for M parallel task. With two runs of different M ($M1$ and $M2$), we
 1298 can use a system of equations to derive

$$T_s = T_{1,1}^{M1} - M1 \left(\frac{T_{1,1}^{M1} - T_{1,1}^{M2}}{M1 - M2} \right). \quad (7.7)$$

1299 We also extract t_p using the same methods:

$$t_p = \frac{T_{1,1}^{M1} - T_{1,1}^{M2}}{M1 - M2}. \quad (7.8)$$

1300 From Tab. 7.2, we set $M1 = 50$ and $M2 = 74$ and take their corresponding $T_{1,1}$ from the table to
 1301 calculate T_s and t_p .

$$T_s = 803.1\text{s} \text{ and } t_p = 104.6\text{s} \quad (7.9)$$

1302 Now, we have specific estimation for the fraction of serial computing time, F_s :

$$F_s = \frac{803.1}{803.1 + 104.6 \cdot M}. \quad (7.10)$$

1303 The maximum M for this study is 473 which evaluates Eq. (7.10): $F_s = 0.016$ or 1.6% of computing
 1304 time. Table 7.3 shows the resulting speedups.

1305 We see a speedup that exceeds expectations from Eq. (7.5) for real trail runs. **TODO: reflect**
 1306 **on results when the tables are totally filled in.** We also see that there are diminishing returns as

M Tasks	$S_{p,c}$		
	$S_{1,2}$	$S_{1,8}$	$T_{1,16}$
50	1.90 [1.76]	5.23 [4.14]	6.35 [5.34]
74	1.90 [1.83]	5.62 [4.82]	9.00 [6.64]
100			
200	-		
473	-		1:09:42.9

Table 7.3 Speed up summaries for analyses for serial and multithreaded processes. M tasks is the number of functional-parallel tasks ran for the computation. $S_{p,c}$ is a single speedup comparison for runs utilizing p nodes and c threads. $[\cdot]$ are the estimated speedups calculated from Tab. 7.2, Eq. (7.10), and Eq. (7.5). Empty entries are indicated with '-'.

1307 the number of threads increases. For small jobs with large c , both the expected and observed
 1308 speedup are significantly smaller than c . One thing not considered in Eq. (7.5) is the time incurred
 1309 via communication latency. Communication latency increases with the number of threads and
 1310 contributes to diminishing returns. Therefor, these results are not conclusive. Each entry in
 1311 Tab. 7.2 represent only one run of the script and therefore the data are not precise and lacks the
 1312 full scope of timing costs. Yet, they do give us a good idea of what HAWC gains in multithreading
 1313 analysis software. We see very clearly that there is a lot to gain, and this new coding pattern will
 1314 expand HAWC's analysis capabilities.

1315 7.6 Analysis Results

1316 TODO: talk about the results

1317 We were not able to generate background trials in time of writing this thesis. These are not
 1318 shown and are an immediate next step for this analysis before publication.

1319 We did not see DM, but we did see some interesting excesses in the 10 Tev range at order 2σ .
 1320 Draco was not included as the PDF of some of our analysis bins were wider than what is reasonable
 1321 for a point source analysis. Draco is at a high zenith for HAWC, so the effort required to include it
 1322 was not justified by the benefits.

1323 7.7 Systematics

1324 These are identical to what was performed earlier in Glory Duck, Section 6.7. We are also
 1325 sensitive to the choice in spatial template, and this was explored in Section 6.7.2 and Section 6.8.2.

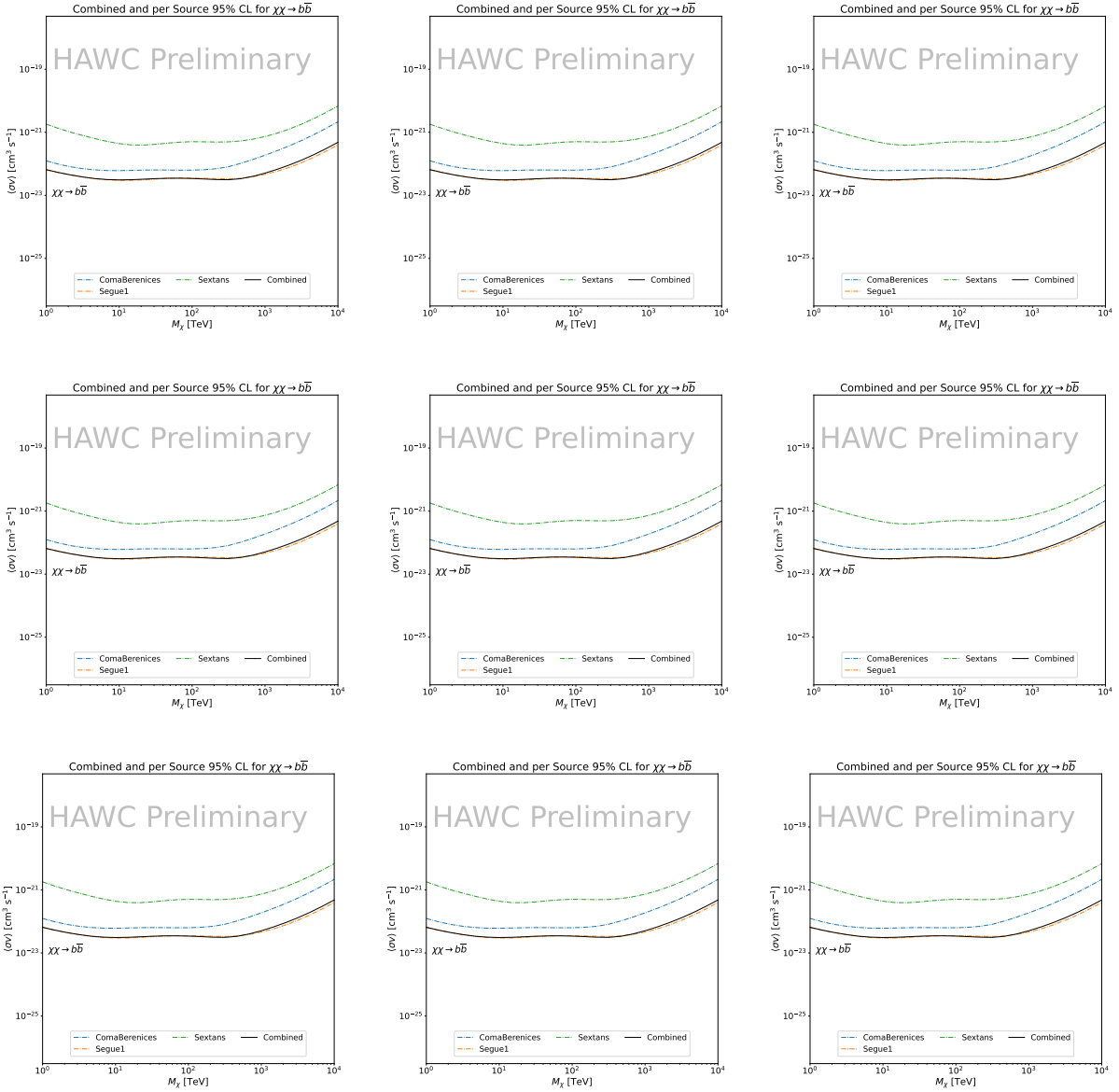


Figure 7.7 TODO: fill this out

1326 $\mathcal{L}\mathcal{S}$ also provided the uncertainty on their mean spatial models. We perform a study on the
 1327 $\pm 1\sigma$ spatial templates and show corresponding confidence limits in [TODO: link to figure](#)

1328 7.8 Conclusion and Discussion

1329 We want to include the remaining dSph and DM decay from the dSphs. We saw an improvement
 1330 of [TODO: value](#) compared to Glory Duck which had many more dSphs. [TODO: copy some text](#)
 1331 from earlier section.

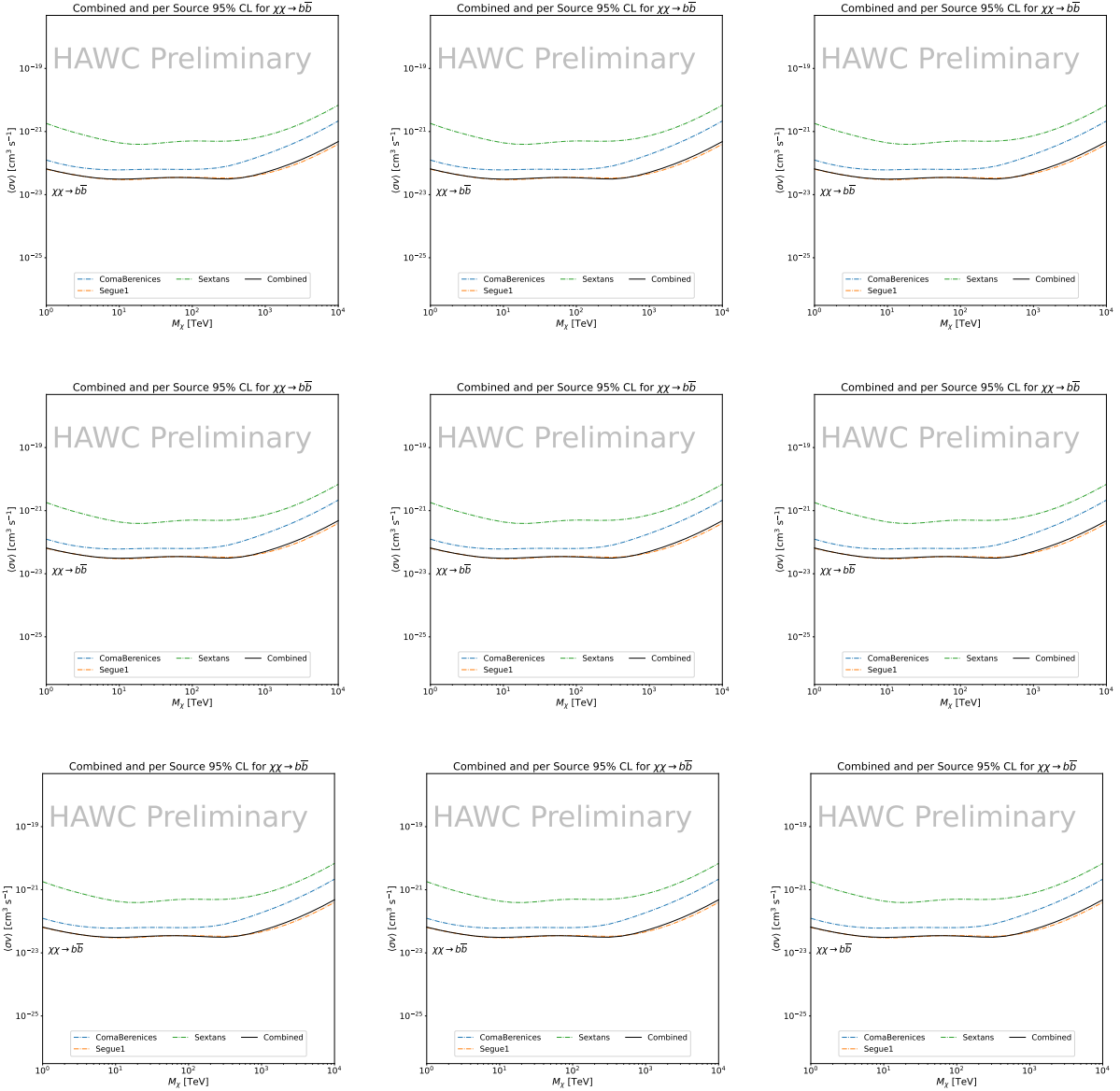


Figure 7.8 TODO: fill this out



Figure 7.9 TODO: TS of analysis of results. See if we can include Draco[NEEDS A SOURCE][FACT CHECK THIS]



Figure 7.10 TODO: TS of analysis of results. There will definitely be 2[NEEDS A SOURCE][FACT CHECK THIS]



Figure 7.11 TODO: Comparison of channels with GD combined results.[NEEDS A SOURCE][FACT CHECK THIS]

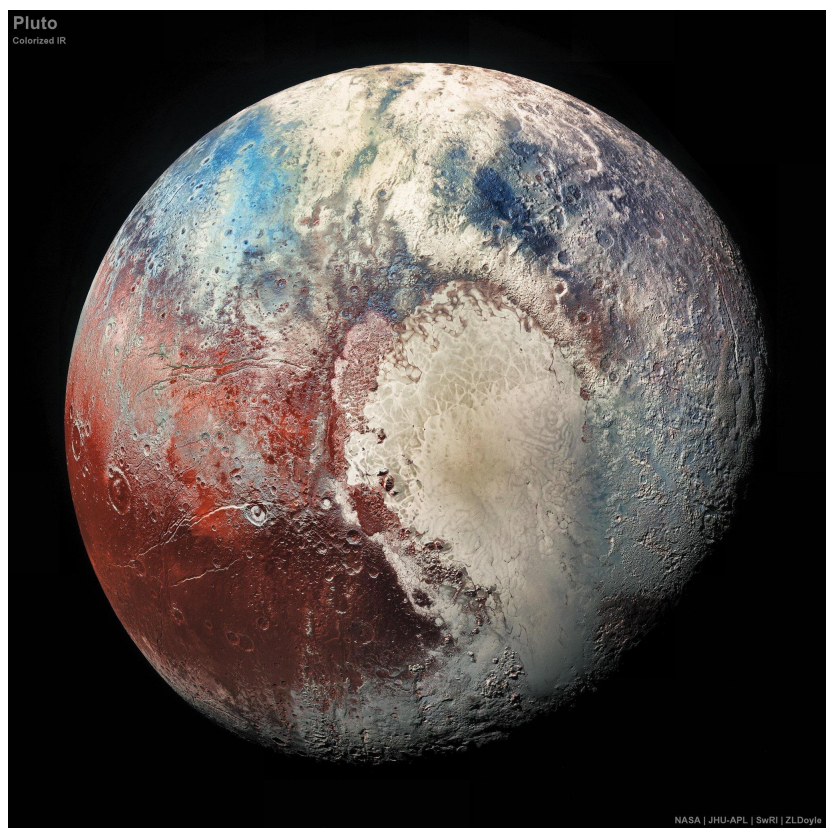


Figure 7.12 TODO: show p1 and m1 limits around[NEEDS A SOURCE][FACT CHECK THIS]



Figure 7.13 TODO: there will be 2[NEEDS A SOURCE][FACT CHECK THIS]

CHAPTER 8

**1332 HEAVY DARK MATTER ANNIHILATION SEARCH WITH ICECUBE'S NORTH SKY
1333 TRACK DATA**

CHAPTER 9

NU DUCK

1334

APPENDIX A

MULTI-EXPERIMENT SUPPLEMENTARY FIGURES

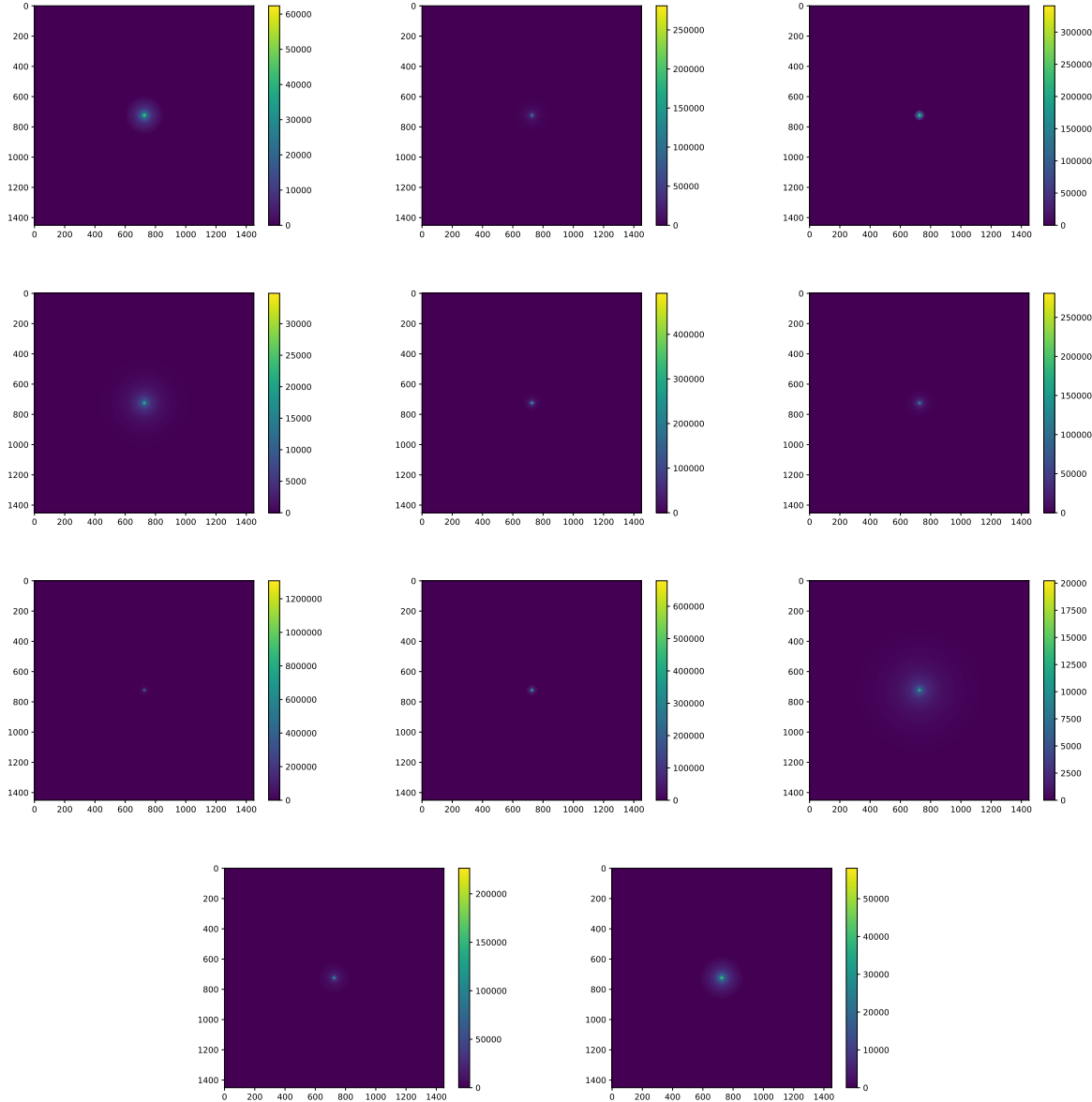


Figure A.1 Sister figure to Figure 6.3. Sources in the first row from left to right: Bootes I, Canes Venatici I, II. In second row: Draco, Hercules, Leo I. In the first row: Leo II, Leo IV, Sextans. In the final row: Ursa Major I, Ursa Major II.

APPENDIX B

1336

MULTITHREADING SUPPLEMENTARY FIGURES

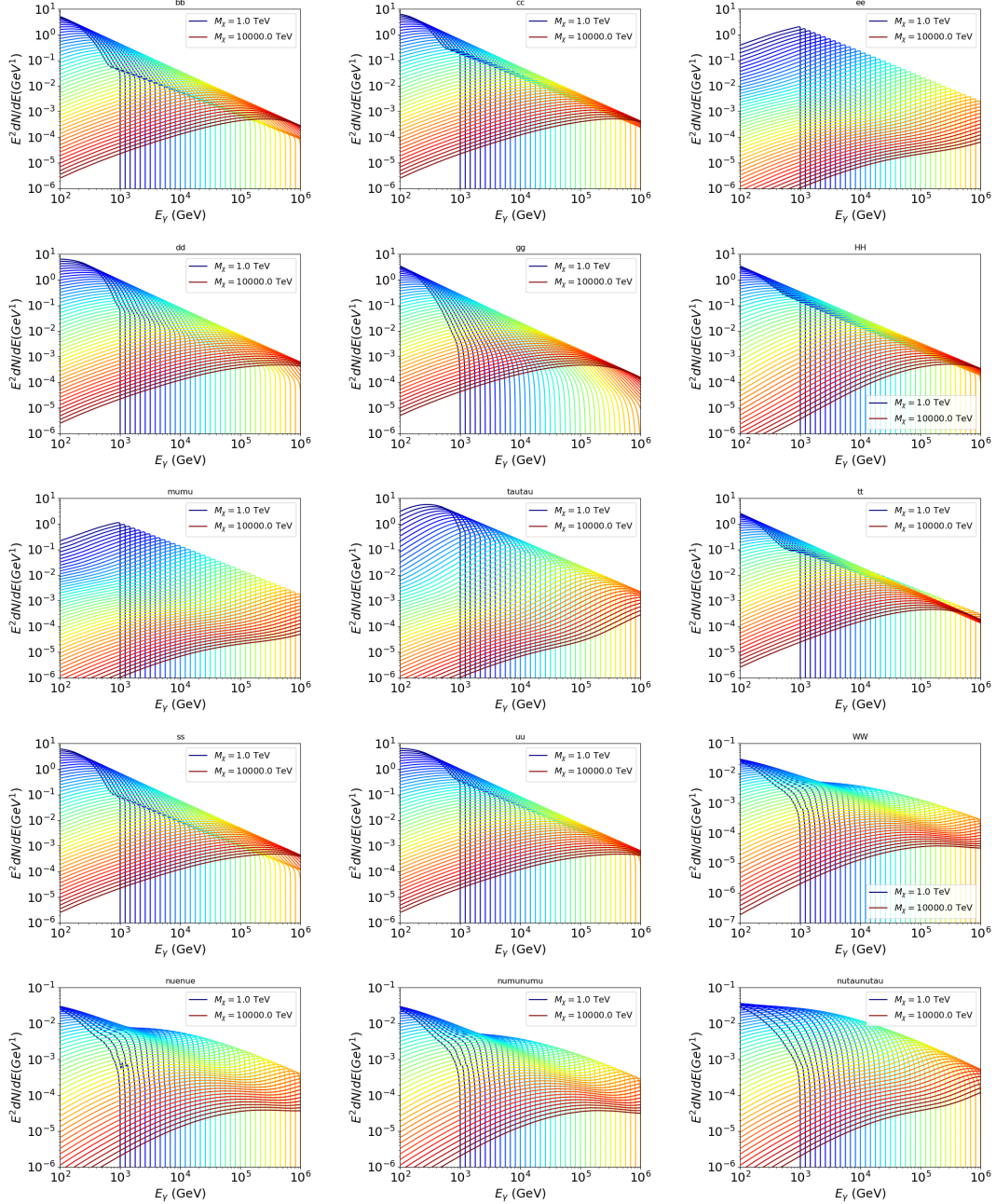


Figure B.1 Sister figure to Figure 7.2 for remaining SM primary annihilation channels studied for this thesis. These did not require any post generation smoothing and so are directly pulled from [64] with a binning scheme most helpful for a HAWC analysis.

1337 **B.1 mpu_analysis.py**

```
13381 import warnings
13392 with warnings.catch_warnings():
13403     warnings.simplefilter("ignore")
13414 # Python base libraries
13425 import os
13436 import sys
13447 import time
13458 # Import general libraries with namespace
13469 import matplotlib
13470 # Necessary for computing on cluster
13481 matplotlib.use("agg")
13492 import numpy as np
13503 import multiprocessing as mp
13514 # Import HAWC software
13525 sys.path.insert(1, os.path.join(os.environ['HOME'], 'hawc_software', 'threeML-
1353     analysis-scripts', 'fitModel'))
13546 from analysis_modules import *
13557 from threeML import *
13568 from hawc_hal import HAL, HealpixConeROI
13579 from threeML.minimizer.minimization import FitFailed
13580 # Import Dark Matter HAWC Libraries
13591 import analysis_utils as au
13602 import spectra as spec
13613 import sources as srcs
13624
13635 #* READ ONLY PATHS This block will change eventually
13646 MASS_LIST = './plotting/studies/nd/masses.txt'
13657 CHAN_LIST = './plotting/studies/nd/chans.txt'
13668
13679 #* WRITE PATHS, default location is to scratch
13680 OUT_PATH = os.path.join(os.environ["SCRATCH"], os.environ["USER"], 'New_duck')
```

```

13691 print('Our out path is going to be {}'.format(OUT_PATH))
13702
13713 # Define parallel Function. Can also be run serially
13724 def some_mass_fit(sigVs, datalist, shape, dSph, jfactor, mass_chan,
13735                 progress=None, log_file='', queue=None, i_job=0):
13746
13757     if progress is None:
13768         progress = [0]
13779     else: # Create log files for each thread
13780         log_file = log_file.replace('.log', '_ThreadNo_')
13791         log_file = log_file + str(i_job) + ".log"
13802         sys.stdout = open(log_file, "w")
13813
13824     fits = []
13835
13846     try:
13857         for m_c in mass_chan:
13868             print(f'Mass chan tuple: {m_c}')
13879             mass = int(m_c[0])
13880             ch = m_c[1]
13891             # Build path to output files
13902             outPath = os.path.join(OUT_PATH, ch, dSph)
13913             au.ut.ensure_dir(outPath)
13924
13935             if progress[i_job] < 0:
13946                 # If the master gets a Keyboard interrupt, commit suicide.
13957                 break
13968
13979                 ### Start Model Building for DM mass and SM channel #####
13980                 spectrum = spec.DM_models.HDMSpectra()
13991                 spectrum.set_channel(ch)
14002
14013                 myDwarf = ExtendedSource(dSph, spatial_shape=shape,

```

```

14024                     spectral_shape=spectrum)
14035
14046             spectrum.J = jfactor * u.GeV**2 / u.cm**5
14057             spectrum.sigmav = 1e-24 * u.cm**3 / u.s
14068             spectrum.set_dm_mass(mass * u.GeV)
14079
14080             spectrum.sigmav.bounds = (1e-30, 1e-12)
14091             model = Model(myDwarf)
14102             ##### End model Building #####
14113
14124             jl = JointLikelihood(model, datalist, verbose=False)
14135
14146             try:
14157                 result, lhdf = jl.fit(compute_covariance=False)
14168                 ts = -2.* (jl.minus_log_like_profile(1e-30) - jl.
1417 _current_minimum)
14189                 # Also profile the LLH vs sv
14190                 ll = jl.get_contours(spectrum.sigmav, sigVs[0],
14201                                 sigVs[-1], len(sigVs),
14212                                 progress=False, log=['False'])
14223
14234                 sigv_ll = au.ut.calc_95_from_profile(ll[0], ll[2])
14245                 # Write results to file
14256                 outFileLL = outPath+f"/LL_{dSph}_{ch}_mass{int(mass)}_GD.txt"
14267                 np.savetxt(outFileLL, (sigVs, ll[2]),
14278                               delimiter='\t', header='sigV\tLL\n')
14289
14290                 with open(outPath+f"/results_{dSph}_{ch}_mass{int(mass)}_GD.
1430 txt", "w") as results_file:
14311                     results_file.write("mDM [GeV]\tsigV_95\tsigV_B.F.\n")
14322
14333                     results_file.write("%i\t%.5E\t%.5E\t%.5E"%(mass, sigv_ll,
14344                                         ts, result.value[0]))

```

```

14355         # End write to file
14356
14357     except FitFailed: # Don't kill all threads if a fit fails
14358         print("Fit failed. Go back and calculate this spectral model
14359             later")
14360
14361         fits.append((ch, mass, -1, -1))
14362
14363         with open(log_file+'.fail', 'w') as f_file:
14364             f_file.write(f'{ch}, {mass}\n')
14365
14366
14367         progress[i_job] += 1
14368
14369         matplotlib.pyplot.close() # Prevent leaky memory
14370
14371
14372         fits.append((ch, mass, result.value[0], ts))
14373
14374         progress[i_job] += 1
14375
14376         matplotlib.pyplot.close()
14377
14378     except KeyboardInterrupt:
14379
14380         progress[i_job] = -1
14381
14382
14383         fits = np.array(fits)
14384
14385     if queue is None:
14386
14387         return fits
14388
14389     else:
14390
14391         queue.put((i_job, fits))
14392
14393
14394 def main(args):
14395
14396     masses = np.loadtxt(MASS_LIST, dtype=int)
14397
14398     chans = np.loadtxt(CHAN_LIST, delimiter=',', dtype=str)
14399
14400     mass_chan = au.ut.permute_lists(chans, masses)
14401
14402
14403     print(f"DM masses for this study are: {masses}")
14404
14405     print(f"SM Channels for this study are XX -> {chans}")
14406
14407     print(mass_chan)
14408
14409
14410     # extract information from input argument

```

```

14687 dSph = args.dSph
14698 data_mngr = au.ut.Data_Selector('P5_NN_2D')
14709 dm_profile = srcts.Spatial_DM(args.catalog, dSph, args.sigma, args.decay)
14710
14721     ### Extract Source Information ####
14732 if dm_profile.get_dec() < -22.0 or dm_profile.get_dec() > 62.0:
14743     raise ValueError("HAWC can't see this source D: Exitting now...")
14754
14765 print(f'{dSph} information')
14776 print(f'jfac: {dm_profile.get_factor()}\tRA: {dm_profile.get_ra()}\tDec: {dm_profile.get_dec()}\n')
14797
14808 shape = SpatialTemplate_2D(fits_file=dm_profile.get_src_fits())
14819     ### Finish Extract Source Information ####
14820
14831     ### LOAD HAWC DATA ####
14842 roi = HealpixConeROI(data_radius=2.0, model_radius=8.0,
14853                         ra=dm_profile.get_ra(), dec=dm_profile.get_dec())
14864 bins = choose_bins.analysis_bins(args, dec=dm_profile.get_dec())
14875
14886 hawc = HAL(dSph, data_mngr.get_datmap(), data_mngr.get_detres(), roi)
14897 hawc.set_active_measurements(bin_list=bins)
14908 datalist = DataList(hawc)
14919     ### FINISH LOAD HAWC DATA ####
14920
14931 # set up SigV sampling. This sample is somewhat standardized
14942 sigVs = np.logspace(-28,-18, 1001, endpoint=True) # NOTE This will change
1495 whith HDM
14963
14974 if args.n_threads == 1:
14985     # No need to start || programming just iterate over the masses
14996 kw_arg = dict(sigVs=sigVs, datalist=datalist, shape=shape, dSph=dSph,
15007                 jfactor=dm_profile.get_factor(), mass_chan=mass_chan,

```

```

15018                 log_file=args.log)
15029             some_mass_fit(**kw_arg)
15030         else:
15041             # I Really want to suppress TQMD output
15052             from tqdm import tqdm
15063             from functools import partialmethod
15074             tqdm.__init__ = partialmethod(tqdm.__init__, disable=True)
15085
15096             x = np.array_split(mass_chan, args.n_threads)
15107             n_jobs = len(x)
15118
15129             print("Thread jobs summary by mass and SM channel")
15130             for xi in x:
15141                 print(f'{xi}')
15152
15163             queue = mp.Queue()
15174             progress = mp.Array('i', np.zeros(n_jobs, dtype=int))
15185
15196             # Define task pool that will be split amongsts threads
15207             kw_args = [dict(sigVs=sigVs, datalist=datalist, shape=shape,
15218                             dSph=dSph, jfactor=dm_profile.get_factor(),
15229                             mass_chan=mass_chan, progress=progress,
15230                             queue=queue, i_job=i, log_file=args.log)
15241                 for i, mass_chan in enumerate(x)]
15252
15263             # Define each process
15274             procs = [mp.Process(target=some_mass_fit, kwargs=kw_args[i]) \
15285                 for i in range(n_jobs)]
15296
15307             ### Start MASTER Thread only code block ###
15318             # Begin running all child threads
15329             for proc in procs: proc.start()
15330

```

```

15341     try:
15352         # In this case, the master does nothing except monitor progress of
1536         the threads
15373         # In an ideal world, the master thread also does some computation.
15384         n_complete = np.sum(progress)
15395         while_count = 0
15406
15417         while n_complete < len(mass_chan):
15428
15439             if np.any(np.asarray(progress) < 0):
15440                 # This was no threads are stranded when killing the script
15451                 raise KeyboardInterrupt()
15462             if while_count%1000 == 0:
15473                 print(f"{np.sum(progress)} of {len(mass_chan)} finished")
15484
15495             n_complete = np.sum(progress)
15506             time.sleep(.25)
15517             while_count += 1
15528
15539         except KeyboardInterrupt:
15540             # signal to jobs that it's time to stop
15551                 for i in range(n_jobs):
15562                     progress[i] = -2
15573                     print('\nKeyboardInterrupt: terminating early.')
15584             ### End MASTER Thread only code block ###
15595
15606             fitss = [queue.get() for proc in procs]
15617             print(fitss)
15628             print(f'Thread statuses: {progress[:]}')
15639
15640             # putting results in a file
15651
15662             print("QUACK! All Done!")

```

```

15673
15684
15695 if __name__ == '__main__':
15706     import argparse
15717
15728     p = argparse.ArgumentParser(description="Run a DM annihilation analysis on
1573         a dwarf spheroidal for a specific SM channel for DM masses [1 TeV to 10
1574         PeV]")
15759
15760     # Dwarf spatial modeling arguements
15771     p.add_argument("-ds", "--dSph", type=str,
15782             help="dwarf spheroidal galaxy to be studied", required=
1579     True)
15803     p.add_argument("-cat", "--catalog", type=str, choices=['GS15', 'LS20'],
15814             default='LS20', help="source catalog used")
15825     p.add_argument("-sig", "--sigma", type=int, choices=[-1, 0, 1], default=0,
15836             help="Spatial model uncertainty. 0 corresponds to the
1584 median. +/-1 correspond to the +/-1sigma uncertainty respectively.")
15857
15868     # Arguements for the energy estimators
15879     p.add_argument("-e", "--estimator", type=str,
15880             choices=['P5_NHIT', 'P5_NN_2D'],
15891             default="P5_NN_2D", required=False,
15902             help="The energy estimator choice. Options are: P5_NHIT,
1591 P5_NN_2D. GP not supported (yet).")
15923     p.add_argument("--use-bins", default=None, nargs="*",
15934             help="Bins to use for the analysis", dest="use_bins")
15945     p.add_argument('--select_bins_by_energy', default=None, nargs="*",
15956             help="Does nothing. May fill in later once better
1596 understood")
15977     p.add_argument('--select_bins_by_fhit', default=None, nargs="*",
15988             help="Also does nothing see above")
15999     p.add_argument( '-ex', "--exclude", default=None, nargs="*",

```

```

16000         help="Exclude Bins", dest="exclude")

16011

16022 # Computing and logging arguements.

16033 p.add_argument('-nt', '--n_threads', type=int, default=1,
16044                         help='Maximum number of threads spawned by script. Default
16055 is 4')

16065 p.add_argument('-log', '--log', type=str, required=True,
16076                         help='Name for log files. Especially needed for threads')

16087

16098 p.add_argument('--decay', action="store_true",
16109                         help='Set spectral DM hypothesis to decay')

16110

16121 args = p.parse_args()

16132 print(args.decay)

16143 if args.exclude is None: # default exclude bins 0 and 1
16154     args.exclude = ['B0C0Ea', 'B0C0Eb', 'B0C0Ec', 'B0C0Ed', 'B0C0Ee']

16165

16176 if args.decay: OUT_PATH += '_dec'
16187 else: OUT_PATH += '_ann'

16198

16209 OUT_PATH = OUT_PATH + '_' + args.catalog
16210 if args.sigma != 0: OUT_PATH += f'_{args.sigma}sig'

16221

16232 main(args)

```

BIBLIOGRAPHY

- [1] Anne M. Green. “Dark matter in astrophysics/cosmology”. In: *SciPost Phys. Lect. Notes* (2022), p. 37. doi: [10.21468/SciPostPhysLectNotes.37](https://doi.org/10.21468/SciPostPhysLectNotes.37). URL: <https://scipost.org/10.21468/SciPostPhysLectNotes.37>.
- [2] Bing-Lin Young. “A survey of dark matter and related topics in cosmology”. In: *Frontiers of Physics* 12 (Oct. 2016). doi: <https://doi.org/10.1007/s11467-016-0583-4>. URL: <https://doi.org/10.1007/s11467-016-0583-4>.
- [3] Gianfranco Bertone, Dan Hooper, and Joseph Silk. “Particle dark matter: evidence, candidates and constraints”. In: *Physics Reports* 405.5 (2005), pp. 279–390. issn: 0370-1573. doi: <https://doi.org/10.1016/j.physrep.2004.08.031>. URL: <https://www.sciencedirect.com/science/article/pii/S0370157304003515>.
- [4] Gianfranco Bertone and Dan Hooper. “History of dark matter”. In: *Rev. Mod. Phys.* 90 (4 Aug. 2018), p. 045002. doi: [10.1103/RevModPhys.90.045002](https://doi.org/10.1103/RevModPhys.90.045002). URL: <https://link.aps.org/doi/10.1103/RevModPhys.90.045002>.
- [5] Fritz Zwicky. “The Redshift of Extragalactic Nebulae”. In: *Helvetica Physica Acta* 6. (1933), pp. 110–127. doi: [10.5169/seals-110267](https://doi.org/10.5169/seals-110267).
- [6] Vera C. Rubin and Jr. Ford W. Kent. “Rotation of the Andromeda Nebula from a Spectroscopic Survey of Emission Regions”. In: *ApJ* 159 (Feb. 1970), p. 379. doi: [10.1086/150317](https://doi.org/10.1086/150317).
- [7] K. G. Begeman, A. H. Broeils, and R. H. Sanders. “Extended rotation curves of spiral galaxies: dark haloes and modified dynamics”. In: *Monthly Notices of the Royal Astronomical Society* 249.3 (Apr. 1991), pp. 523–537. issn: 0035-8711. doi: [10.1093/mnras/249.3.523](https://doi.org/10.1093/mnras/249.3.523). eprint: <https://academic.oup.com/mnras/article-pdf/249/3/523/18160929/mnras249-0523.pdf>. URL: <https://doi.org/10.1093/mnras/249.3.523>.
- [8] *Different types of gravitational lenses*. website. Feb. 2004. URL: <https://esahubble.org/images/heic0404b/>.
- [9] Douglas Clowe et al. “A Direct Empirical Proof of the Existence of Dark Matter”. In: *apjl* 648.2 (Sept. 2006), pp. L109–L113. doi: [10.1086/508162](https://doi.org/10.1086/508162). arXiv: [astro-ph/0608407 \[astro-ph\]](https://arxiv.org/abs/astro-ph/0608407).
- [10] Planck Collaboration and N. et. al. Aghanim. “Planck 2018 results I. Overview and the cosmological legacy of Planck”. In: *A&A* 641 (2020). doi: [10.1051/0004-6361/201833880](https://doi.org/10.1051/0004-6361/201833880). URL: <https://doi.org/10.1051/0004-6361/201833880>.
- [11] Wayne Hu. *Matter Density Animation*. web. 2024. URL: <http://background.uchicago.edu/~whu/animbut/anim2.html>.

- 1658 [12] Wenlong Yuan et al. “A First Look at Cepheids in a Type Ia Supernova Host with JWST”. in:
1659 *The Astrophysical Journal Letters* 940.1 (Nov. 2022). doi: [10.3847/2041-8213/ac9b27](https://doi.org/10.3847/2041-8213/ac9b27).
1660 URL: <https://dx.doi.org/10.3847/2041-8213/ac9b27>.
- 1661 [13] Wendy L. Freedman. “Measurements of the Hubble Constant: Tensions in Perspective”. In:
1662 *The Astrophysical Journal* 919.1 (Sept. 2021), p. 16. doi: [10.3847/1538-4357/ac0e95](https://doi.org/10.3847/1538-4357/ac0e95).
1663 URL: <https://dx.doi.org/10.3847/1538-4357/ac0e95>.
- 1664 [14] Jodi Cooley. “Dark Matter direct detection of classical WIMPs”. In: *SciPost Phys. Lect.
1665 Notes* (2022), p. 55. doi: [10.21468/SciPostPhysLectNotes.55](https://doi.org/10.21468/SciPostPhysLectNotes.55). URL: <https://scipost.org/10.21468/SciPostPhysLectNotes.55>.
- 1667 [15] “Search for new phenomena in events with an energetic jet and missing transverse momentum
1668 in pp collisions at $\sqrt{s} = 13$ TeV with the ATLAS detector”. In: *Phys. Rev. D* 103
1669 (11 July 2021), p. 112006. doi: [10.1103/PhysRevD.103.112006](https://doi.org/10.1103/PhysRevD.103.112006). URL: <https://link.aps.org/doi/10.1103/PhysRevD.103.112006>.
- 1671 [16] *Jetting into the dark side: a precision search for dark matter*. website. July 2020. URL:
1672 <https://atlas.cern/updates/briefing/precision-search-dark-matter>.
- 1673 [17] Celine Armand et. al. “Combined dark matter searches towards dwarf spheroidal galaxies
1674 with Fermi-LAT, HAWC, H.E.S.S., MAGIC, and VERITAS”. in: *Proceedings of Science*.
1675 Vol. 395. Mar. 2022. doi: <https://doi.org/10.22323/1.395.0528>.
- 1676 [18] Tracy R. Slatyer. “Les Houches Lectures on Indirect Detection of Dark Matter”. In: *SciPost
1677 Phys. Lect. Notes* (2022), p. 53. doi: [10.21468/SciPostPhysLectNotes.53](https://doi.org/10.21468/SciPostPhysLectNotes.53). URL:
1678 <https://scipost.org/10.21468/SciPostPhysLectNotes.53>.
- 1679 [19] Christian W Bauer, Nicholas L. Rodd, and Bryan R. Webber. “Dark matter spectra from
1680 the electroweak to the Planck scale”. In: *Journal of High Energy Physics* 2021.1029-8479
1681 (June 2021). doi: [https://doi.org/10.1007/JHEP06\(2021\)121](https://doi.org/10.1007/JHEP06(2021)121).
- 1682 [20] Riccardo Catena and Piero Ullio. “A novel determination of the local dark matter density”.
1683 In: *Journal of Cosmology and Astroparticle Physics* 2010.08 (Aug. 2010), p. 004. doi:
1684 [10.1088/1475-7516/2010/08/004](https://doi.org/10.1088/1475-7516/2010/08/004). URL: <https://dx.doi.org/10.1088/1475-7516/2010/08/004>.
- 1686 [21] B. P. Abbott et al. “Observation of Gravitational Waves from a Binary Black Hole Merger”.
1687 In: *Phys. Rev. Lett.* 116 (6 Feb. 2016), p. 061102. doi: [10.1103/PhysRevLett.116.061102](https://doi.org/10.1103/PhysRevLett.116.061102). URL: <https://link.aps.org/doi/10.1103/PhysRevLett.116.061102>.
- 1689 [22] R. Abbasi et. al. “Observation of high-energy neutrinos from the Galactic plane”. In: *Science*
1690 380.6652 (June 2023), pp. 1338–1343.

- 1691 [23] NASA Goddard Space Flight Center. *Fermi's 12-year view of the gamma-ray sky*. website.
1692 2022. URL: <https://svs.gsfc.nasa.gov/14090>.
- 1693 [24] Marco Cirelli et al. "PPPC 4 DM ID: a poor particle physicist cookbook for dark matter
1694 indirect detection". In: *Journal of Cosmology and Astroparticle Physics* 2011.03 (Mar.
1695 2011), p. 051. doi: [10.1088/1475-7516/2011/03/051](https://doi.org/10.1088/1475-7516/2011/03/051). URL: <https://dx.doi.org/10.1088/1475-7516/2011/03/051>.
- 1697 [25] Javier Rico. "Gamma-Ray Dark Matter Searches in Milky Way Satellites—A Comparative
1698 Review of Data Analysis Methods and Current Results". In: *Galaxies* 8.1 (Mar. 2020), p. 25.
1699 doi: [10.3390/galaxies8010025](https://doi.org/10.3390/galaxies8010025). arXiv: [2003.13482 \[astro-ph.HE\]](https://arxiv.org/abs/2003.13482).
- 1700 [26] W. B. Atwood et al. "The Large Area Telescope on the Fermi Gamma-Ray Space Telescope
1701 Mission". In: *apj* 697.2 (June 2009), pp. 1071–1102. doi: [10.1088/0004-637X/697/2/1071](https://doi.org/10.1088/0004-637X/697/2/1071). arXiv: [0902.1089 \[astro-ph.IM\]](https://arxiv.org/abs/0902.1089).
- 1703 [27] M. Ackermann et al. "Searching for Dark Matter Annihilation from Milky Way Dwarf
1704 Spheroidal Galaxies with Six Years of Fermi Large Area Telescope Data". In: *prl* 115.23,
1705 231301 (Dec. 2015), p. 231301. doi: [10.1103/PhysRevLett.115.231301](https://doi.org/10.1103/PhysRevLett.115.231301). arXiv:
1706 [1503.02641 \[astro-ph.HE\]](https://arxiv.org/abs/1503.02641).
- 1707 [28] Mattia Di Mauro, Martin Stref, and Francesca Calore. "Investigating the effect of Milky
1708 Way dwarf spheroidal galaxies extension on dark matter searches with Fermi-LAT data".
1709 In: *Phys. Rev. D* 106 (12 Dec. 2022), p. 123032. doi: [10.1103/PhysRevD.106.123032](https://doi.org/10.1103/PhysRevD.106.123032).
1710 URL: <https://link.aps.org/doi/10.1103/PhysRevD.106.123032>.
- 1711 [29] F. et al. Aharonian. "Observations of the Crab Nebula with H.E.S.S.". In: *Astron. Astrophys.*
1712 457 (2006), pp. 899–915. doi: [10.1051/0004-6361:20065351](https://doi.org/10.1051/0004-6361:20065351). arXiv: [astro-ph/0607333](https://arxiv.org/abs/astro-ph/0607333).
- 1714 [30] J. Albert et al. "VHE γ -Ray Observation of the Crab Nebula and its Pulsar with the MAGIC
1715 Telescope". In: *The Astrophysical Journal* 674.2 (Feb. 2008), p. 1037. doi: [10.1086/525270](https://doi.org/10.1086/525270). URL: <https://dx.doi.org/10.1086/525270>.
- 1717 [31] N. Park. "Performance of the VERITAS experiment". In: *Proceedings, 34th International
1718 Cosmic Ray Conference (ICRC2015): The Hague, The Netherlands, July, 30th July - 6th
1719 August*. Vol. 34. 2015, p. 771. arXiv: [1508.07070 \[astro-ph.IM\]](https://arxiv.org/abs/1508.07070).
- 1720 [32] A. Abramowski et al. "H.E.S.S. constraints on Dark Matter annihilations towards the Sculptor
1721 and Carina Dwarf Galaxies". In: *Astropart. Phys.* 34 (2011), pp. 608–616. doi: [10.1016/j.astropartphys.2010.12.006](https://doi.org/10.1016/j.astropartphys.2010.12.006). arXiv: [1012.5602 \[astro-ph.HE\]](https://arxiv.org/abs/1012.5602).
- 1723 [33] A. Abramowski et al. "Search for dark matter annihilation signatures in H.E.S.S. observations
1724 of Dwarf Spheroidal Galaxies". In: *Phys. Rev. D* 90 (2014), p. 112012. doi: [10.1103/PhysRevD.90.112012](https://doi.org/10.1103/PhysRevD.90.112012). arXiv: [1410.2589 \[astro-ph.HE\]](https://arxiv.org/abs/1410.2589).

- 1726 [34] H. Abdalla et al. “Searches for gamma-ray lines and ‘pure WIMP’ spectra from Dark
1727 Matter annihilations in dwarf galaxies with H.E.S.S”. in: *JCAP* 11 (2018), p. 037. doi:
1728 [10.1088/1475-7516/2018/11/037](https://doi.org/10.1088/1475-7516/2018/11/037). arXiv: [1810.00995 \[astro-ph.HE\]](https://arxiv.org/abs/1810.00995).
- 1729 [35] J. Aleksić et al. “Optimized dark matter searches in deep observations of Segue 1 with
1730 MAGIC”. in: *JCAP* 1402 (2014), p. 008. doi: [10.1088/1475-7516/2014/02/008](https://doi.org/10.1088/1475-7516/2014/02/008).
1731 arXiv: [1312.1535 \[hep-ph\]](https://arxiv.org/abs/1312.1535).
- 1732 [36] V.A. Acciari et al. “Combined searches for dark matter in dwarf spheroidal galaxies observed
1733 with the MAGIC telescopes, including new data from Coma Berenices and Draco”. In: *Physics of the Dark Universe* (2021), p. 100912. issn: 2212-6864. doi: <https://doi.org/10.1016/j.dark.2021.100912>. URL: <https://www.sciencedirect.com/science/article/pii/S2212686421001370>.
- 1737 [37] M. L. Ahnen et al. “Indirect dark matter searches in the dwarf satellite galaxy Ursa Major II
1738 with the MAGIC Telescopes”. In: *JCAP* 1803.03 (2018), p. 009. doi: [10.1088/1475-7516/2018/03/009](https://doi.org/10.1088/1475-7516/2018/03/009). arXiv: [1712.03095 \[astro-ph.HE\]](https://arxiv.org/abs/1712.03095).
- 1740 [38] S. et al. Archambault. “Dark matter constraints from a joint analysis of dwarf Spheroidal
1741 galaxy observations with VERITAS”. in: *prd* 95.8 (Apr. 2017). doi: [10.1103/PhysRevD.95.082001](https://doi.org/10.1103/PhysRevD.95.082001). arXiv: [1703.04937 \[astro-ph.HE\]](https://arxiv.org/abs/1703.04937).
- 1743 [39] Louise Oakes et al. “Combined Dark Matter searches towards dwarf spheroidal galaxies with
1744 Fermi-LAT, HAWC, HESS, MAGIC and VERITAS”. in: *Proceedings of Science*. 2019.
- 1745 [40] Celine Armand et al. on behalf of the Fermi-LAT, HAWC, HESS, MAGIC, VERITAS.
1746 “Combined Dark Matter searches towards dwarf spheroidal galaxies with Fermi-LAT,
1747 HAWC, HESS, MAGIC and VERITAS”. in: *Proceedings of Science*. 2021.
- 1748 [41] Daniel Kerszberg et al. on behalf of the Fermi-LAT, HAWC, HESS, MAGIC, and VER-
1749 TIAS collaborations. “Search for dark matter annihilation with a combined analysis of
1750 dwarf spheroidal galaxies from Fermi-LAT, HAWC, H.E.S.S., MAGIC and VERITAS”. in:
1751 *Proceedings of Science*. 2023.
- 1752 [42] A. U. Abeysekara et al. “Observation of the Crab Nebula with the HAWC Gamma-Ray
1753 Observatory”. In: *The Astrophysical Journal* 843.1 (June 2017), p. 39. doi: [10.3847/1538-4357/aa7555](https://doi.org/10.3847/1538-4357/aa7555). URL: <https://doi.org/10.3847/1538-4357/aa7555>.
- 1755 [43] Giacomo Vianello et al. *The Multi-Mission Maximum Likelihood framework (3ML)*. 2015.
1756 arXiv: [1507.08343 \[astro-ph.HE\]](https://arxiv.org/abs/1507.08343).
- 1757 [44] Marco Cirelli et al. “PPPC 4 DM ID: a poor particle physicist cookbook for dark matter
1758 indirect detection”. In: *Journal of Cosmology and Astroparticle Physics* 2011.03 (Mar.
1759 2011). issn: 1475-7516. doi: [10.1088/1475-7516/2011/03/051](https://doi.org/10.1088/1475-7516/2011/03/051). URL: <http://dx.doi.org/10.1088/1475-7516/2011/03/051>.

- 1761 [45] Alex Geringer-Sameth, Savvas M. Koushiappas, and Matthew Walker. “DWARF GALAXY
1762 ANNIHILATION AND DECAY EMISSION PROFILES FOR DARK MATTER EXPERI-
1763 MENTS”. in: *The Astrophysical Journal* 801.2 (Mar. 2015), p. 74. ISSN: 1538-4357. doi:
1764 [10.1088/0004-637X/801/2/74](https://doi.org/10.1088/0004-637X/801/2/74). URL: <http://dx.doi.org/10.1088/0004-637X/801/2/74>.
- 1766 [46] A. Albert et al. “Dark Matter Limits from Dwarf Spheroidal Galaxies with the HAWC
1767 Gamma-Ray Observatory”. In: *The Astrophysical Journal* 853.2 (Feb. 2018), p. 154. ISSN:
1768 1538-4357. doi: [10.3847/1538-4357/aaa6d8](https://doi.org/10.3847/1538-4357/aaa6d8). URL: <http://dx.doi.org/10.3847/1538-4357/aaa6d8>.
- 1770 [47] V. Bonnivard et al. “Spherical Jeans analysis for dark matter indirect detection in dwarf
1771 spheroidal galaxies - Impact of physical parameters and triaxiality”. In: *Mon. Not. Roy.
1772 Astron. Soc.* 446 (2015), pp. 3002–3021. doi: [10.1093/mnras/stu2296](https://doi.org/10.1093/mnras/stu2296). arXiv:
1773 [1407.7822 \[astro-ph.HE\]](https://arxiv.org/abs/1407.7822).
- 1774 [48] M. Ackermann et al. “Searching for Dark Matter Annihilation from Milky Way Dwarf
1775 Spheroidal Galaxies with Six Years of Fermi Large Area Telescope Data”. In: *prl* 115.23,
1776 231301 (Dec. 2015), p. 231301. doi: [10.1103/PhysRevLett.115.231301](https://doi.org/10.1103/PhysRevLett.115.231301). arXiv:
1777 [1503.02641 \[astro-ph.HE\]](https://arxiv.org/abs/1503.02641).
- 1778 [49] M. L. Ahnen et al. “Limits to Dark Matter Annihilation Cross-Section from a Combined
1779 Analysis of MAGIC and Fermi-LAT Observations of Dwarf Satellite Galaxies”. In: *JCAP*
1780 1602.02 (2016), p. 039. doi: [10.1088/1475-7516/2016/02/039](https://doi.org/10.1088/1475-7516/2016/02/039). arXiv: [1601.06590](https://arxiv.org/abs/1601.06590)
1781 [astro-ph.HE].
- 1782 [50] Javier Rico et al. *gLike: numerical maximization of heterogeneous joint
1783 likelihood functions of a common free parameter plus nuisance parameters*.
1784 <https://doi.org/10.5281/zenodo.4601451>. Version v0.09.03. Mar. 2021. doi: [10.5281/zenodo.4601451](https://doi.org/10.5281/zenodo.4601451). URL: <https://doi.org/10.5281/zenodo.4601451>.
- 1786 [51] Tjark Miener and Daniel Nieto. *LklCom: Combining likelihoods from different experiments*.
1787 <https://doi.org/10.5281/zenodo.4597500>. Version v0.5.3. Mar. 2021. doi: [10.5281/zenodo.4597500](https://doi.org/10.5281/zenodo.4597500). URL: <https://doi.org/10.5281/zenodo.4597500>.
- 1789 [52] T. Miener et al. “Open-source Analysis Tools for Multi-instrument Dark Matter Searches”.
1790 In: *arXiv e-prints*, arXiv:2112.01818 (Dec. 2021), arXiv:2112.01818. arXiv: [2112.01818](https://arxiv.org/abs/2112.01818)
1791 [astro-ph.IM].
- 1792 [53] Alex Geringer-Sameth and Matthew Koushiappas Savvas M. and Walker. “Dwarf galaxy
1793 annihilation and decay emission profiles for dark matter experiments”. In: *Astrophys.
1794 J.* 801.2 (2015), p. 74. doi: [10.1088/0004-637X/801/2/74](https://doi.org/10.1088/0004-637X/801/2/74). arXiv: [1408.0002](https://arxiv.org/abs/1408.0002)
1795 [astro-ph.CO].

- 1796 [54] Gianfranco Bertone, Dan Hooper, and Joseph Silk. “Particle dark matter: evidence, can-
1797 didates and constraints”. In: *Physics Reports* 405.5-6 (Jan. 2005), pp. 279–390. ISSN:
1798 0370-1573. doi: [10.1016/j.physrep.2004.08.031](https://doi.org/10.1016/j.physrep.2004.08.031). URL: <http://dx.doi.org/10.1016/j.physrep.2004.08.031>.
- 1800 [55] V. Bonnivard et al. “Dark matter annihilation and decay in dwarf spheroidal galaxies: The
1801 classical and ultrafaint dSphs”. In: *Mon. Not. Roy. Astron. Soc.* 453.1 (2015), pp. 849–867.
1802 doi: [10.1093/mnras/stv1601](https://doi.org/10.1093/mnras/stv1601). arXiv: [1504.02048 \[astro-ph.HE\]](https://arxiv.org/abs/1504.02048).
- 1803 [56] A. et al. Albert. “Searching for Dark Matter Annihilation in Recently Discovered Milky Way
1804 Satellites with Fermi-LAT”. in: *Astrophys. J.* 834.2 (2017), p. 110. doi: [10.3847/1538-4357/834/2/110](https://doi.org/10.3847/1538-4357/834/2/110). arXiv: [1611.03184 \[astro-ph.HE\]](https://arxiv.org/abs/1611.03184).
- 1806 [57] Mattia Di Mauro and Martin Wolfgang Winkler. “Multimessenger constraints on the dark
1807 matter interpretation of the Fermi-LAT Galactic Center excess”. In: *prd* 103.12, 123005
1808 (June 2021), p. 123005. doi: [10.1103/PhysRevD.103.123005](https://doi.org/10.1103/PhysRevD.103.123005). arXiv: [2101.11027 \[astro-ph.HE\]](https://arxiv.org/abs/2101.11027).
- 1810 [58] HongSheng Zhao. “Analytical models for galactic nuclei”. In: *Mon. Not. Roy. Astron. Soc.*
1811 278 (1996), pp. 488–496. doi: [10.1093/mnras/278.2.488](https://doi.org/10.1093/mnras/278.2.488). arXiv: [astro-ph/9509122 \[astro-ph\]](https://arxiv.org/abs/astro-ph/9509122).
- 1813 [59] H. C. Plummer. “On the Problem of Distribution in Globular Star Clusters: (Plate 8.)”
1814 In: *Monthly Notices of the Royal Astronomical Society* 71.5 (Mar. 1911), pp. 460–470.
1815 ISSN: 0035-8711. doi: [10.1093/mnras/71.5.460](https://doi.org/10.1093/mnras/71.5.460). eprint: <https://academic.oup.com/mnras/article-pdf/71/5/460/2937497/mnras71-0460.pdf>. URL:
1816 <https://doi.org/10.1093/mnras/71.5.460>.
- 1818 [60] Daniel R. Hunter. “Derivation of the anisotropy profile, constraints on the local velocity
1819 dispersion, and implications for direct detection”. In: *JCAP* 02 (2014), p. 023. doi:
1820 [10.1088/1475-7516/2014/02/023](https://doi.org/10.1088/1475-7516/2014/02/023). arXiv: [1311.0256 \[astro-ph.CO\]](https://arxiv.org/abs/1311.0256).
- 1821 [61] Barun Kumar Dhar and Liliya L. R. Williams. “Surface mass density of the Einasto family
1822 of dark matter haloes: are they Sersic-like?” In: *Mon. Not. Roy. Astron. Soc.* (2010). doi:
1823 [10.1111/j.1365-2966.2010.16446.x](https://doi.org/10.1111/j.1365-2966.2010.16446.x).
- 1824 [62] M. Baes and E. Van Hese. “Dynamical models with a general anisotropy profile”. In:
1825 *Astron. Astrophys.* 471 (2007), p. 419. doi: [10.1051/0004-6361:20077672](https://doi.org/10.1051/0004-6361:20077672). arXiv:
1826 [0705.4109 \[astro-ph\]](https://arxiv.org/abs/0705.4109).
- 1827 [63] Matthew G. Walker, Edward W. Olszewski, and Mario Mateo. “Bayesian analysis of re-
1828 solved stellar spectra: application to MMT/Hectochelle observations of the Draco dwarf
1829 spheroidal”. In: *mnras* 448.3 (Apr. 2015), pp. 2717–2732. doi: [10.1093/mnras/stv099](https://doi.org/10.1093/mnras/stv099).
1830 arXiv: [1503.02589 \[astro-ph.GA\]](https://arxiv.org/abs/1503.02589).

- 1831 [64] Nicholas L. Rodd et al. “Dark matter spectra from the electroweak to the Planck scale”. In:
1832 *J. High Energy Physics* 121.10.1007 (June 2021).
- 1833 [65] Pace, Andrew B and Strigari, Louis E. “Scaling relations for dark matter annihilation and
1834 decay profiles in dwarf spheroidal galaxies”. In: *Monthly Notices of the Royal Astronomical
1835 Society* 482.3 (Oct. 2018), pp. 3480–3496. ISSN: 0035-8711. doi: [10.1093/mnras/sty2839](https://doi.org/10.1093/mnras/sty2839).
- 1837 [66] Albert, A. et al. “Search for gamma-ray spectral lines from dark matter annihilation in
1838 dwarf galaxies with the High-Altitude Water Cherenkov observatory”. In: *Phys. Rev. D* 101 (10 May 2020), p. 103001. doi: [10.1103/PhysRevD.101.103001](https://doi.org/10.1103/PhysRevD.101.103001). URL:
1839 <https://link.aps.org/doi/10.1103/PhysRevD.101.103001>.
- 1841 [67] Victor Eijkhout and Edmund Show and Robert van de Geijn. *The Science of Computing.
1842 The Art of High Performance Computing*. Vol. 3. Open Copy published under CC-BY 4.0
1843 license, 2023, pp. 63–66.